

# **The Interstellar Medium Scaling Relations in Cosmological Simulations**

A thesis submitted in partial fulfilment of the requirements  
for the Masters in Cosmology degree in the Department of  
Physics and Astronomy, University of the Western Cape.



**UNIVERSITY** *of the*  
**WESTERN CAPE**

**Ms Mpendulo Sibiya**

Supervisor : Prof Lerothodi Leeuw

Co-Supervisor : Prof Maarten Baes, Prof Erwin de Blok, and Prof Mario Santos

Date : October 2022

## Acknowledgement

I am grateful for the support provided by all of my supervisors in achieving different objectives (financial, academic, and physical well-being). I wish to thank my primary supervisor Prof Lerothodi Leeuw, and my co-supervisors, Prof Maarten Baes, Prof Erwin de Blok, and Prof Mario Santos. Thank you to Dr Gauri Sharma for working closely with me to organise my work. Thank you to Prof. Mario Santos, the South African Radio Astronomy Observatory (SARAO) and Center of Radio Cosmology (CRC) bursary chair, for the funding. I want to thank the University of Ghent research team; they were all responsive and helpful in the face of the Covid-19 pandemic, notably Anand Utsav Kapoor, who taught me how to work with SKIRT. Moreover, I am very grateful for the support from the University of Western Cape (UWC) research team and the Inter-University Institute for Data Intensive Astronomy (IDIA) for providing access to their facilities to conduct the research. I thank you all for your support. Thank you to my parents, friends, and family. May God bless you.



## DECLARATION

I, Mpendulo Emmarencia Sibiyi, declare that I solely did this work. It was never submitted for any examination or academic purposes at any university. All helpful references consulted have been appropriately acknowledged with complete citations.



# Contents

<b>1</b>	<b>Introduction</b>	<b>1</b>
1.1	Galaxy formation and evolution sub-grid models in cosmological simulations . . . . .	2
1.2	Scaling Relations . . . . .	5
1.3	DustPedia observational data. . . . .	8
1.4	SIMBA hydrodynamic cosmological simulations . . . . .	9
1.5	EAGLE hydrodynamic cosmological simulations. . . . .	14
1.6	The problem with cosmological simulations . . . . .	15
1.7	SKIRT . . . . .	15
1.8	The research aim, objective, significance, and questions . . . . .	16
1.9	Project limitations . . . . .	17
1.10	Thesis Overview . . . . .	18
<b>2</b>	<b>Method</b>	<b>19</b>
2.1	Methodology for dealing with SIMBA data . . . . .	21
2.1.1	Criteria for selecting galaxies in the SIMBA snapshot . . . . .	21
2.1.2	Extraction of galaxies in the SIMBA snapshot . . . . .	24
2.1.3	Post-processing SIMBA data with SKIRT . . . . .	26
2.1.4	Treatment of the SIMBA data with SKIRT . . . . .	29
2.1.5	Spectral energy distribution . . . . .	30
2.1.6	SKIRT system tests . . . . .	34
2.1.7	Deriving observations from SIMBA data processed with SKIRT . . . . .	37
2.2	Methodology for dealing with EAGLE data . . . . .	40
2.2.1	Selection criteria for the EAGLE data . . . . .	40
2.2.2	Post-processing procedure of EAGLE data compared to that of SIMBA data . . . . .	42
2.2.3	Deriving observations from EAGLE data processed with SKIRT . . . . .	43
2.3	Methodology for dealing with DustPedia data . . . . .	45
2.3.1	Selection criteria for DustPedia data . . . . .	45

2.3.2	Deriving DustPedia observation's physical properties using the observational fluxes . . . . .	47
2.4	Statistics test on selected galaxies datasets . . . . .	49
2.5	Method limitations and conclusions . . . . .	49
<b>3</b>	<b>Results and Discussion</b>	<b>51</b>
3.1	Inferred physical properties . . . . .	51
3.2	Luminosities as a proxy of stellar mass, dust mass, and star formation rate	55
3.2.1	The WISE $3.4\mu m$ luminosity as the galaxy stellar mass proxy . . . . .	57
3.2.2	The WISE $22\mu m$ luminosity as the galaxy SFR proxy . . . . .	58
3.2.3	The SPIRE $250\mu m$ luminosity as the galaxy dust mass proxy . . . . .	59
3.2.4	Result summary . . . . .	60
3.3	The MIR/FIR luminosities scaling relations . . . . .	63
3.3.1	Scaling relation between luminosities in the $3.4\mu m$ and $22\mu m$ band	63
3.3.2	Scaling relation between luminosities in the $3.4\mu m$ and $250\mu m$ band . . . . .	63
3.3.3	Scaling relation between luminosities in the $22\mu m$ and $250\mu m$ band	65
3.3.4	Interesting findings in the luminosities ratio relations . . . . .	65
3.3.5	Result summary . . . . .	67
3.4	Dust to stellar mass ratios scaling relation . . . . .	69
3.4.1	Result summary . . . . .	72
<b>4</b>	<b>Conclusion</b>	<b>73</b>

## List of Figures

1	The hierarchical galaxy formation . . . . .	2
2	The Faber-Jackson relation . . . . .	6
3	The colour-magnitude diagram . . . . .	6
4	The Tully-Fisher scaling relation . . . . .	6
5	The galaxy stellar mass function . . . . .	10
6	The EAGLE galaxies dust scaling relations . . . . .	15
7	The project’s methodology . . . . .	20
8	SIMBA galaxies’ physical properties distribution . . . . .	22
9	SIMBA galaxies’ physical properties box and whisker diagrams . . . . .	23
10	SKIRT output SED for SIMBA dustier galaxies . . . . .	30
11	SKIRT output SED for less dustier SIMBA galaxies . . . . .	32
12	The spatial grid convergence test . . . . .	36
13	The photon test . . . . .	37
14	Physical properties derived for SIMBA galaxies . . . . .	39
15	EAGLE galaxies’ physical properties distribution . . . . .	40
16	The EAGLE galaxies box and whisker physical properties distribution diagram. . . . .	41
17	Physical properties derived for EAGLE galaxies . . . . .	44
18	DustPedia galaxies’ physical properties distribution . . . . .	45
19	DustPedia galaxies’ box and whisker statistics diagram . . . . .	46
20	The relationship between this work’s DustPedia-derived physical properties and properties derived from Clark et al. (2018). . . . .	48
21	The normalised distribution of all studied galaxies’ physical properties . . . . .	53
22	The relationship between the galaxies’ luminosities and their stellar mass, dust mass, and SFR . . . . .	56
23	The $3.4\mu m$ galaxies’ luminosities and their stellar mass relation. . . . .	57
24	The $22\mu m$ galaxies’ luminosities and their SFR relation. . . . .	59
25	The $250\mu m$ galaxies’ luminosities and their dust mass relation . . . . .	60
26	The relationship between the galaxies’ luminosities and their stellar mass, dust mass, and SFR, at $1\sigma$ intrinsic scatter . . . . .	62

27	The galaxies' MIR and FIR luminosities scaling relations . . . . .	64
28	The MIR and FIR luminosities' ratio scaling relations . . . . .	66
29	The MIR and FIR luminosities scaling relations at $1\sigma$ intrinsic scatter . . . . .	68
30	The dust scaling relations . . . . .	70
31	The NUV-r colour magnitudes scaling relations . . . . .	71
32	The NUV-r colour magnitudes scaling relation. Galaxies coloured according to SFR . . . . .	72



## List of Tables

1	Acronyms List 1 . . . . .	viii
2	Acronyms List 2 . . . . .	ix
3	SKIRT input files galaxy information . . . . .	27
4	The UV to submm wavelength studied band lists . . . . .	31
5	The galaxy information for each studied dataset . . . . .	50
6	The statistical summary of the studied galaxies' physical properties . . . . .	54



EAGLE	Evolution and Assembly of GaLaxies and their Environment
2MASS	Two Micron All Sky Survey
AGN	Active Galactic Nuclei
ANOVA	Analysis of Variance
BH	Black Hole
C	Compactness Parameter
CIGALE	Code Investigating GALaxy Emission
CMD	Cluster Theory
D	Distance
EDA	Empirical Dust Attenuation
fPDR	Fraction of Photo-Dissociation Region
GALEX	Galaxy Evolution Explorer
GB	Gigabyte
GMC	Giant Molecular Cloud
HDF5	Hierarchical Data Format version 5
HI	Emission line of neutral atomic hydrogen
IDIA	Institute for Data-Intensive Astronomy
IMF	Initial Mass Function
IR	Infrared
IRAS	Infrared Astronomical Satellite
ISM	Interstellar Medium
kpc	Kilo-parsecs
Mpc	Mega-parsecs
NUV	Near Visible Ultraviolet

**Table 1:** Acronyms List 1

PACS	Photodetector Array Camera and Spectrometer
PDR	Photo-Dissociation Region
SDSS	Spectroscopic Sloan Digital Sky Survey
SED	Spectral Energy Distribution
SFR	Star-Formation Rate
SKIRT	Stellar Kinematics Including Radiative Transfer
SMBH	Supermassive Black Hole
SPH	Smoothed Particle Hydrodynamics
SPIRE	Spectral and Photometric Imaging REceiver
sSFR	Specific Star-Formation Rate
WISE	Wide-field Infrared Survey Explorer
XML	Extensible Markup Language
Z	Metallicity
$M_{\odot}$	Solar mass
$L_{\odot}$	Solar luminosoty
$\mu m$	Microns

**Table 2:** Acronyms List 2

# ABSTRACT

This work presents the scaling relations for the redshift zero galaxies in the SIMBA<sup>1</sup> cosmological hydrodynamic simulations. The aim is to test the degree to which the SIMBA simulations reproduce the physical properties observed in real galaxies, as this simulation has advanced dust models that will better our understanding of hydrodynamic simulation's sub-grid models, galaxy formation, and galaxy evolution. To achieve this, we studied and compared the scaling relations of observed galaxies from the DustPedia<sup>2</sup> observational database and the scaling relations of the SIMBA simulated galaxies. We selected galaxies ranging from a minimum stellar mass of  $10^9 M_{\odot}$  and a minimum specific star-formation of  $10^{10.5}/\text{yr}$  to the upper limit of the galaxies in the snapshot. These selection criteria are used to make sure that our sample contains galaxies with an active interstellar medium<sup>3</sup> (ISM). We employed a radiative transfer code called SKIRT to derive the simulated galaxies' fluxes ranging from UV to sub-mm wavelengths. Then we used previous literature equations to estimate the galaxies' inferred physical properties. We also included the EAGLE (Evolution and Assembly of GaLaxies and their Environment) cosmological hydrodynamic simulations dataset that was studied by Camps et al. (2016) to compare the performance between the two simulations. Our results show that SIMBA galaxies mimic the star-formation quenching observed in real massive galaxies very well; the results further show that this was the case for SIMBA but not for EAGLE cosmological simulations. We found more agreement between observations and SIMBA simulated galaxies in the  $f_{250}/f_{350}$  versus  $f_{350}/f_{500}$  submm colour–colour relation and dust scaling relations. On the other hand, we discovered a discrepancy in the dust-to-stellar versus NUV-r colour relation in SIMBA simulated galaxies. We also found a discrepancy in the submm colour–colour relation for EAGLE galaxies' dust scaling relations. Overall, both simulations, when coupled with SKIRT, can reproduce observations and each simulation has room for improvement.

---

<sup>1</sup><http://simba.roe.ac.uk/>

<sup>2</sup>[www.dustpedia.com](http://www.dustpedia.com)

<sup>3</sup>The environment between the star systems

# 1 Introduction

Cosmological hydrodynamic simulations use the numerical implementation of theoretical physics to reconstruct the physical events of the current universe. They enable the analysis of particles at different redshifts and are built on cosmological boxes of various sizes in mega-parsecs (Mpc). For more than a decade now, these simulations have been valuable tools in galaxy formation and evolution studies (Vogelsberger et al., 2020a). However, cosmological simulations have limitations because galaxy evolution and formation processes, such as star formation and feedback, are not fully understood. They cannot fully reproduce what is seen in observations. In this project, we test the degree to which the SIMBA hydrodynamic simulation succeeds in reproducing observations by studying and comparing the scaling relations of observed galaxies in the DustPedia database with the same scaling relations for the simulated SIMBA galaxies. We also incorporated Camps et al. (2016) EAGLE hydrodynamic simulation dataset, as the two studies are similar, which enabled us to study and compare the two simulations with observations.

This introductory chapter comprises several sections. The first, Section 1.1, provides a background to galaxy formation and evolution theory. Section 1.2 introduces the scaling relations studied in this project, and Section 1.3 describes the observational data. Section 1.4 briefly describes SIMBA simulations, Section 1.5 describes the EAGLE simulations, and in Section 1.6, we discuss the issue of cosmological simulation, which this research will contribute towards. Section 1.7 provides a background on the SKIRT code used to create this work's mock observational fluxes. After that, Section 1.8 describes the current research's aims, objectives, questions, and significance. Finally, Section 1.9 discusses the research limitations within this thesis, and Section 1.10 provides the thesis overview.

## 1.1 Galaxy formation and evolution sub-grid models in cosmological simulations

This section discusses the basic physics background and sub-grid models of galaxy formation in cosmological simulations illustrated in Figure 1.

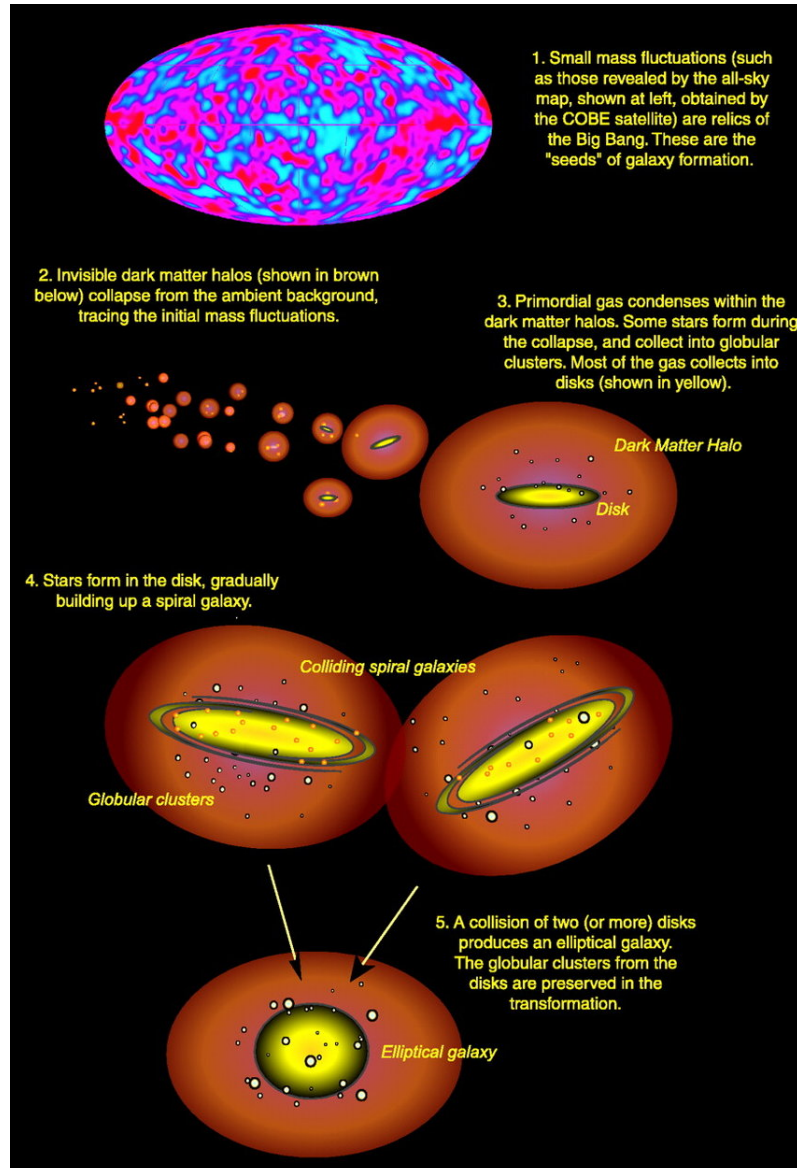


**Figure 1:** The hierarchical galaxy formation shows how galaxies formed from the early homogeneous and isotropic universe (Abraham & van den Bergh, 2001).

## Gravity and cosmic structure formation

We believe that the Universe is a composition of baryons that are dominated by dark matter, and dark energy. Galaxy evolution theory assumes that the Universe's initial conditions were homogeneous and isotropic. However, the dominant hypothesis suggests quantum fluctuations are responsible for instability in the early Universe because no structure would have formed should the Universe remain homogeneous and isotropic without any disturbances. The fluctuations and the gravitational instability changed the Universe's homogeneous and isotropic state. The state change caused some regions to have more gravitational pulling than others, resulting in the Universe becoming non-linear and forming over and under dense regions. Due to the universe expansion, cosmological simulations' density growth rate is  $\sigma \propto t^\alpha$  where  $\alpha > 0$ , parameters may vary with different cosmological simulations and conditions. (Cole et al., 1994; Anghopo, 2021).

## Gas cooling

Due to gravitational instability across the Universe, some regions become dense to the point where the cooling effect becomes essential. Over-dense area emits strong shocks that cause gas entropy. Hotter gas, such as  $T > 10^7 K$ , will be collisionally ionised and cool via free-free emission (Brussaard & Van de Hulst, 1962). Hot gas ( $10^4 K < T < 10^7 K$ ) ionised atoms will decay to the ground state, making it possible for the recombination of electrons and ions. Gases with temperatures below  $10^4 K$  will cool due to heavy element excitation, de-excitation, and molecular cooling. The gas cooling in the over-dense region will lead to the formation of molecules. This is because when the area cools enough, it promotes the inflow of large gas quantities, loses pressure support, and collapses until its angular momentum supports it. In due course, molecules will trigger the formation of pro-galaxies that are surrounded by dark matter halos. (Birnbom & Dekel, 2003). In the cosmological simulations, cold mode accretion occurs when the gas flows in along with the cold, dense filaments (Kereš et al., 2005).

## Star formation

Star formation is one of the ongoing studies in galaxy formation and evolution since it is not yet fully understood (Kroupa, 2002; Chabrier, 2003; Kapoor et al., 2021). Nevertheless, it has been observed that when gas collapses in the central region of a dark matter

halo, it begins to self-gravitate. Gas densities increase with gas cooling, which leads to the formation of complex molecules such as Giant Molecular Clouds (GMC). The GMC contains dense core clouds that collapse until they reach high densities that trigger nuclear fusion. Simulations do not resolve the scale at which the GMC and individual cores form. Instead, cosmological simulations use empirical sub-grid recipes for star formation modelling.

### **Black hole formation and growth**

Another poorly understood subject modelled using the sub-grid recipes in cosmological simulations is black hole (BH) formation and their growth. However, BHs formed in the early Universe, and predictions suggest that the growth of BHs may be due to the accretion of gas with little angular momentum or accumulation of gas via viscosity (Volonteri, 2010; Netzer, 2013).

### **Feedbacks**

There is a contradiction between what is seen in observations and what is predicted by theory. Observations show that only 10% of the global baryon has turned into stars (Angthopo, 2021). On the other hand, theory over-predicts the observed gas cooling, indicating that other sources continue to heat the interstellar gas responsible for star formation, causing star formation quenching. We referred to these sources as 'feedbacks', implemented via the sub-grid models in cosmological simulations.

### **Star formation and supernova feedback**

Cosmological events such as supernova<sup>4</sup> explosion release high energy into their surrounding ISM, and the released energy heats the surrounding ISM gas. The released energy also causes galactic winds that eject cool gases out of their galaxies, causing star formation quenching since the galaxy no longer has enough cool gas for star formation (Dekel & Silk, 1986). Most cosmological simulations implement this effect on their galactic scale using the sub-grid recipes as they cannot resolve this process in detail (Somerville & Davé, 2015).

---

<sup>4</sup>An explosive cosmological event occurring when a massive star dies.

## Active galactic nuclei feedback

All galaxies have a central supermassive black hole (SMBH) that co-evolves with its host galaxy as it accretes large amounts of gases from its surroundings (Somerville et al., 2008). This results in the presence of active galactic nuclei (AGN) activities. As with supernovae, AGNs release high energy that heats up and ejects the gas in galaxies. The energy release is perpendicular to the SMBH spin direction (Nelson et al., 2018; Dashyan et al., 2019). The physics of AGNs and SMBHs is not yet fully understood; thus, simulations use the sub-grid recipes to implement the event.

## 1.2 Scaling Relations

Scaling relations are old tools used to understand the galaxies' formation, evolutionary history, and internal physics; examples include the Tully Fisher relation used to determine the galaxy distances (Tully & Fisher, 1977), the elliptical galaxies' fundamental plane relation (Jørgensen et al., 1996), the main sequence relation showing the relationship between the SFR and galaxy stellar mass (Brinchmann et al., 2004; Tomczak et al., 2016), and many others that have been found in the past few years (Casasola et al., 2020). This section starts with a briefing on the common or known scaling relations within the study. Then after the section ends by introducing scaling relations studied in this project.

### Faber-Jackson relation

$$L \propto \sigma^4 \quad (1)$$

Faber-Jackson scaling relation is a relation commonly used to study early-type stars. The relation shows the relationship between the luminosity, apparent magnitude, and stellar velocity dispersion of galaxies. Figure 2 shows the Faber Jackson relation for early-type<sup>5</sup> galaxies, the figure is taken from Sanders (2010), it shows the distance between galaxies. The luminosity is plotted against  $\log(\sigma^4/Ga_0)$ . Both curves show that  $M = c_2 \Sigma_e^4 / Ga_0$ , where the upper M line shows when  $c_2 = 20.25$  and the lower curve (N) shows when  $c_2 = 1$  (Highly Newtonian objects).

---

<sup>5</sup>galaxies that are dominated by an old stellar population and are mainly spheroidals or ellipticals

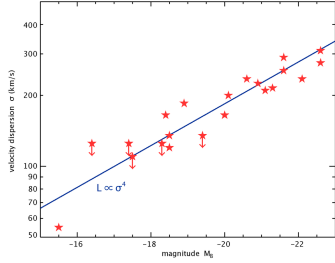


**Figure 2:** In the image above is the Faber-Jackson relation (blue line), which is the relationship between the size of an elliptical galaxy (red stars) and its dispersion velocity (y-axis). (Wikipedia contributors, 2021a)

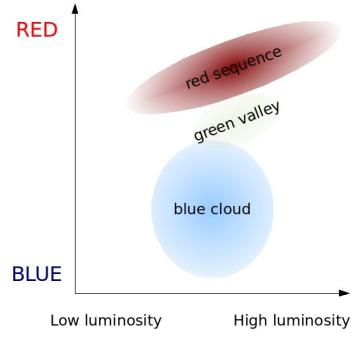


**Figure 3:** This image shows the general model of a color diagram. On the x-axis is luminosity, and on the y-axis is color (in magnitudes). There are three known galaxy populations shown on the color-magnitude diagram. A blue cloud galaxy is in the lower color-magnitude range, a red sequence is in the higher color-magnitude range, and a green valley lies between the two populations. (Wikipedia contributors, 2021b)

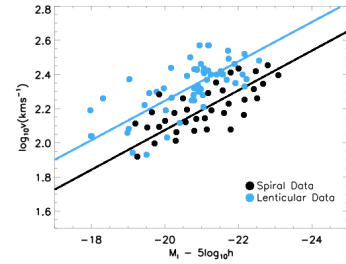


**Figure 4:** The Tully-Fisher relationships of lenticular galaxies (blue dots) and spiral galaxies (black dots) are shown in this image. The straight lines (blue and black) indicate the rotational velocities (y-axis) and the magnitudes (x-axis) of the data sets. (Commons, 2020)

### Color-magnitude relations

$$\text{Magnitude} = M$$

$$M_x = -2.5 * \log(F_x * (D/10) * *2/3631)$$

$$M_x - M_y = -2.5 \log(F_x) - (-2.5 \log(F_y)) \quad (2)$$

where  $M_x$  is absolute magnitude of  $x^{th}$  galaxy,  $F_x$  is flux, and  $D$  is distance from observer.

By utilizing colour as an indicator, the colour-magnitude relation investigates the relationship between galaxy luminosity and stellar population metallicity. Figure 3 is a rough sketch of a colour-magnitude diagram showing different galaxy populations. In the red sequence galaxies, there are higher colour magnitudes; in the green valley galaxies, there are between red and blue clouds. In the blue cloud, galaxies are characterized by lower colour magnitudes, as shown in the figure. It is known that the red clusters are early-type galaxies because elliptical galaxies dominate them. The green valley is a mixture of both red and blue cloud galaxies. Late-type<sup>6</sup> galaxies dominate the blue cloud and are mainly spiral arms galaxies. One of the best tools to use to determine a galaxy cluster's age or flux is the HR diagram<sup>7</sup>. Research has also advanced to the point that The colour-magnitude diagram can also be used, instead of measuring the galaxy's stellar light, the galaxy luminosity ratios between two spectral bands can be used to determine the galaxy temperature. These ratios are referred to as colours and are expressed as the difference between two spectral bands' magnitudes (equation 2). Another one is the Color-color magnitude, the best option in a case where the cluster distance is not known since the colour-colour plot is independent of the distance. The colour-colour plot can be used to separate galaxies of different types. The position of a galaxy in a colour-colour plot is related to the coolness or warmness of the galaxy and its age.

### **Tully-Fisher relation**

The Tully-Fisher scaling relation shows the relationship between galaxy rotational velocity and luminosity (see figure 4) and can be used as a distance indicator. Brent Tully and Richard Fisher discovered this relationship in 1977. They discovered that neutral hydrogen electron spin-flip 21 cm emission could be used to measure the galaxy's rotational velocity. Also, the 21 cm emission line can be used to identify the size of a galaxy emitting light (broad emission line for large galaxies, narrow emission line for small galaxies). As shown in equation 3, equation 3 is the Tully Fisher Relation, the line width of the spectrum is a proxy of galaxy rotation  $2V_{max}$ , and the galaxy rotation is correlated with luminosity. An estimate of the galaxy's distance can be determined from the luminosity and magnitude of the galaxy (Koda et al., 2000).

---

<sup>6</sup>star-forming galaxies and mostly spiral

<sup>7</sup>A diagram showing the relationship between the luminosity and temperature of stars

$$L = V_{max}^4 \quad (3)$$

For this work, we study the simulated galaxies' scaling relations to understand the ISM of the galaxies and compare it with real galaxies. Specifically, we focus on luminosities and dust's physical properties scaling relations because we are interested in studying the ISM for the selected sample of galaxies. We further focus on the MIR and FIR fluxes for the luminosities' scaling relations because we already know and also show our findings' physical property proxies connected to each studied luminosities. This relation is appropriate for identifying the galaxies' flux discrepancies. For the dust scaling relations, we study the dust-to-stellar mass ratio ( $M_{dust}/M_*$ ) relations versus stellar mass ( $M_*$ ); this relation enables the understanding of the galaxies' dust enrichment in terms of stellar mass growth (Hou et al., 2019). We also study ( $M_{dust}/M_*$ ) relations versus NUV-r colour because the NUV-r colour is a good sSFR proxy (Schiminovich et al., 2007). Finally, we study the submm colour-colour relations ( $f_{250}/f_{350}$  v.s  $f_{350}/f_{500}$ ) involving the SPIRE fluxes only because these fluxes are good dust mass indicators (Cortese et al., 2012) and are sensitive to the cold dust contents (Camps et al., 2016).

### 1.3 DustPedia observational data.

The main objective is to test the degree to which the SIMBA simulations subgrid model agrees with observations. To do so, we employ the DustPedia observational database (Davies et al., 2017) to compare the simulated galaxies' scaling relations with real galaxies' scaling relations. DustPedia is a project developed to broaden the study of cosmic dust and its origins (Davies et al., 2017). It aims to develop computer models and tools that enable better data interpretations based on state-of-the-art observations. The DustPedia dataset combines the Herschel (Pilbratt et al., 2010) and Planck (Collaboration et al., 2020) missions dataset alongside other data sources, for example, IRAS (Neugebauer et al., 1984), SDSS (York et al., 2000), 2MASS (Skrutskie et al., 2006), GALEX (Morrissey et al., 2007), and WISE (Wright et al., 2010). Due to this dataset combination, the DustPedia database contains multiwavelength observations across the spectral energy distribution (41), consisting of 875 Herschel's PACS or SPIRE observed local galaxies that reside in different environments, selected according to their stellar mass. These galaxies have a flux detection of at least  $5\sigma$  WISE  $3.4\mu m$ . Their recessional velocity range is less

than 3000 km/s, and they have a diameter of less than one arcmin. Dustpedia galaxies have an average aperture of 17.6 kpc, corresponding to lower stellar mass, an average distance of 21.5 Mpc, and 20 positive flux bands (Trčka et al., 2020). For more Dustpedia information, we refer the reader to Davies et al. (2017).

## 1.4 SIMBA hydrodynamic cosmological simulations

We study the SIMBA hydrodynamic cosmological simulations scaling relations to test whether the simulations' sub-grid recipe models of galaxy evolution and formation agree with observations and other hydrodynamic cosmological simulations. SIMBA is a new generation of the old MUFASA cosmological simulations (Davé et al., 2016). MUFASA is a cosmological hydrodynamic simulation set that runs using the meshless GODUNOV finite mass hydrodynamics method in the new GIZMO<sup>8</sup> code. It has  $H_2$  based star-formation, a two-phase kinetic outflow, a chemical evolution that includes nine elements, and a mass-based evolving halo quenching (Davé et al., 2016). The MUFASA updated version, 'SIMBA', has dust recipes included in the simulation; instead of the halo quenching process, it has BH growth and feedback modules (Davé et al., 2019). Its BH growth is via the torque-limited accretion model from cold gas and Bondi accretion from hot gas. It has black hole feedback via kinetic bipolar outflows and X-ray energy. As a result, it provides a closer look at radiative transfer in galaxies, in other words, more realistic ISM conditions than MUFASA (Davé et al., 2016, 2019; Glowacki et al., 2020). For example, Figure 5 shows the galaxy stellar mass function scaling relation of the SIMBA galaxies and compares the galaxies' relation with EAGLE simulations and observational galaxies from different observations, see the legend. The green band represents all Simba galaxies, Red and blue dashed lines show the mass functions of central galaxies below and above  $sSFR = 10^{1.8+0.3z} Gyr^{-1}$ , respectively, then the dotted cyan line represents EAGLE galaxies. This relation is one of the relations that have proven that Simba can reproduce observed galaxy stellar mass function better than other simulations, as the simulation has more realistic ISM conditions. And in this work, we test the simulation using different techniques and tools that enable us to study more different scaling relations at different wavelengths. Following is the brief of some of the important for the study physics included in the SIMBA simulation, but full detail about the simulation's physics we refer to

<sup>8</sup>A flexible and multi-physics simulation code.

Davé et al. (2019).

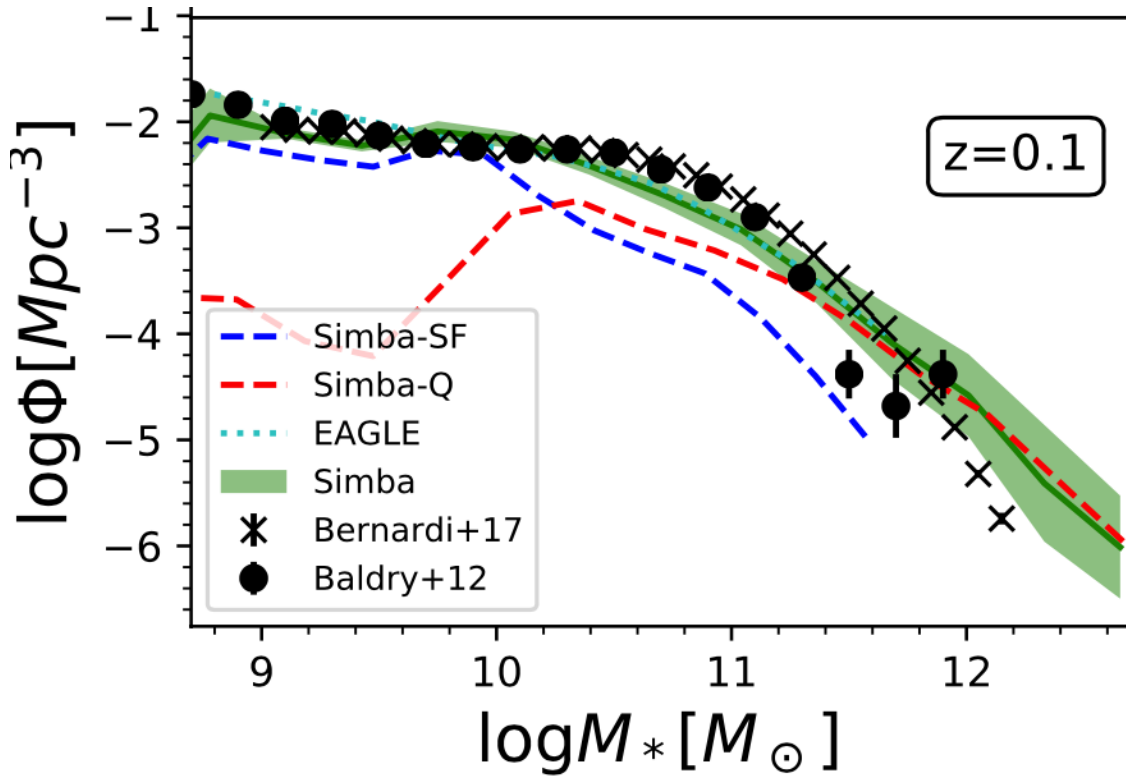
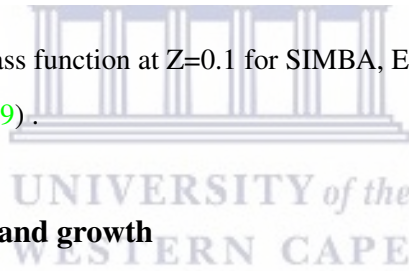


**Figure 5:** The galaxy stellar mass function at  $Z=0.1$  for SIMBA, EAGLE, and observations. This is figure 2 of in Davé et al. (2019).



### SIMBA black hole seeding and growth

SIMBA plants black holes in galaxies using the FOF algorithm. When a galaxy reaches a stellar mass greater than  $M_* > \rho_{BH} \times M_{seed}$ , the star particles near the galaxy center turn into black hole particles, where  $M_{seed} = 10^4 M_\odot / h$  and  $\rho_{BH} = 3 \times 10^5$ . These parameters are chosen so that the simulation make black holes in galaxies with a stellar mass of  $M_* = 9.5 M_\odot$ . The growth of black holes during the simulation is one of the significant updates from the MUFASA to the SIMBA simulation version, and it follows the two following accretion models.

#### 1. Cold gas torque-limited accretion

Only for cold gas  $T < 10^5 \text{K}$  within the kernel of the black-hole, the gas inflow rate  $\dot{M}_{torque}$  is modelled from the host galaxy properties lying within a distance  $R_o$  from the black-hole following Hopkins & Quataert (2011) as :

$$\dot{M}_{torque} \simeq \epsilon_T f_d^{\frac{5}{2}} x \left( \frac{M_{BH}}{10^8 M_\odot} \right)^{\frac{1}{6}} \left( \frac{M_{enc}(R_o)}{10^9 M_\odot} \right) x \left( \frac{R_o}{100 pc} \right)^{-\frac{3}{2}} \left( 1 + \frac{f_o}{f_{gas}} \right)^{-1} M_\odot yr \quad (4)$$

where  $f_d$  is the disk mass fraction (stellar + gas),  $M_{enc}(R_o)$  is the total mass (stellar + gas),  $f_{gas}$  is the gas mass fraction (disk),  $f_o \simeq 0.31 f_d^2 (M_d(R_o)/10^9 M_\odot)^{-\frac{1}{3}}$  ( $M_d$  is the disk mass).

On the other hand,  $\epsilon_T \equiv \epsilon_m x \alpha T$ . where  $\epsilon_T$  is the normalization factor,  $\alpha T$  is the efficiency to transport material from the inner galactic disk into the black hole accretion disk and is value to 5, and  $\epsilon_m$  is the efficiency to transport material from the inner galactic disk into the black hole accretion disk and is value to 0.1

## 2. Bondi accretion from hot gas

Bondi accretion model models the accretion for the non-ISM gas with a temperature  $T > 10^5 k$ .

$$\dot{M}_{Bondi} \simeq \epsilon_m \frac{4\pi G^2 M_{BH}^2 \rho}{(v^2 + c_s^2)^{\frac{3}{2}}} \quad (5)$$

where  $\rho$  is the mean density with the accretion kernel of the blackhole,  $c_s$  is the average hot gas speed of the kernel,  $v$  is the average hot gas velocity relative to the blackhole, and  $\epsilon_m = 0.1$  (as in torque-limited accretion).

## SIMBA galaxies' stellar mass

A galaxy is a collection of stars, hence it has a stellar mass. SIMBA galaxies follow a galaxy stellar mass function that is regulated by the rate at which halos convert their baryons into stars.

## SIMBA galaxies' SFR

SIMBA galaxies SFR is computed as follows,:

$$SFR = \frac{\epsilon_* \rho_{H_2}}{t_{dyn}} \quad (6)$$

where  $\epsilon_* = 0.02$  [Davé et al. \(2019\)](#),  $t_{dyn}$  is the dynamical time, and  $\rho_{H_2}$  is  $H_2$  density.

## SIMBA galaxies' dust masses production, growth, and destruction

As mentioned above SIMBA has special dust recipes. The simulation's dust production and destruction are modeled on the fly mode. The model tracks the life cycle of cosmic dust following dust grains under the assumption that they have the same physical properties and a radius of  $0.1\mu\text{m}$ . This simulation ignores active dust coding (in process for future work [Davé et al. \(2019\)](#)). It follows [Dwek \(1998\)](#) with some changes to condensation efficiency. Dust production and growth are calculated based on metal condensation. Metals from Type II supernovae (SNe) ejects and AGB stars are calculated separately (different equations) and will be summarised in the following subtitles.

For the following equations note that  $m_{i,d}^j$  is the dust mass-produced by the  $j^{\text{th}}$  stellar process of the  $i^{\text{th}}$  element (O,C,Si,Mg,Ca,S,Fe). The dust mass produced by AGB stars with a carbon-to-oxygen ratio greater than 1 ( $C/O > 1$ ) is calculated as :

$$m_{i,d}^{AGB} = \begin{cases} \sigma_c^{AGB} (m_{c,ej}^{AGB} - 0.75m_{0,ej}^{AGB}), & i = c. \\ 0, & \text{otherwise.} \end{cases} \quad (7)$$

where  $\sigma_i^{AGB}$  is the condensation efficiency, fixed to  $\sigma_{i,dust}^{AGB} = 0.2$

The dust mass produced by AGB stars with a carbon-to-oxygen ratio less than 1 ( $C/O < 1$ ) is calculated as :

$$m_{i,d}^{AGB} = \begin{cases} 0, & i = c \\ 16 \sum_{i=Mg,Si,S,Ca,Fe} m_{i,ej}^{AGB}, & i = 0. \\ \sigma_i^{AGB} m_{i,ej}^{AGB} & \text{otherwise} \end{cases} \quad (8)$$

where  $\mu_i$  is the element  $i$ 's mass in atomic unit

The dust mass produced by Type III SNe is calculated as :

$$m_{i,d}^{SNII} = \begin{cases} 16 \sum_{i=Mg,Si,S,Ca,Fe} \sigma_i^{SNII} m_{i,ej}^{SNII}, & i = 0. \\ \sigma_i^{SNII} m_{i,ej}^{SNII} & \text{otherwise} \end{cases} \quad (9)$$

where  $\sigma_i^{SNII}$  is the Type II SNe condensation efficiency, fixed to  $\sigma_{i,dust}^{SNII} = 0.15$ .

SIMBA fixes the condensation efficiency to keep the relation of the dust-to-mass and gas-phase metallicities based on theoretical models ([Rémy-Ruyer et al., 2014](#)).

## SIMBA dust growth

Dust grains can grow by accretion of gas-phase metals. It is calculated from the metal condensation, and their grain radius growth rate follows [Dwek \(1998\)](#) :

$$\left(\frac{dM_{dust}}{dt}\right)_{grow} = \left(1 - \frac{M_{dust}}{M_{metal}}\right) \frac{M_{dust}}{\tau_{accr}} \quad (10)$$

The  $M_{metal} = M_{dust,total} + local\ gas - phase\ metals$ , and the  $\tau_{accr} = \tau_{ref}, \left(\frac{\rho_{ref}}{\rho_g}\right) \left(\frac{T_{ref}}{T_g}\right) \left(\frac{Z_{\odot}}{Z_g}\right)$ , accretion time. Where  $\rho_g$  is the local gas density,  $\rho_{ref} = 100\ H\ atoms\ cm^{-3}$ , is the reference gas density,  $T_g$  is the gas temperature,  $T_{ref} = 20k$  is the reference gas temperature,  $Z_g$  is the gas metallicity, and  $\tau_{ref} = 1 - Myrs$

The grain radii growth is calculated as in [Tsai & Mathews \(1995\)](#) :

$$\left(\frac{da}{dt}\right)_{sp} = \frac{-a}{\tau_{sp}} \quad (11)$$

where :

$$\tau_{sp} = a \left|\frac{da}{dt}\right|^{-1} 0.17 Gyr \left(\frac{a}{0.1\mu m}\right) \left(\frac{10^{-27} g cm^{-3}}{\rho_g}\right) \left[\left(\frac{T_o}{T_g}\right)^w + 1\right] \quad (12)$$

$w = 2.5, T_o = 2 \times 10^6\ k$ .  $w$  controls the  $T_{low}$  scaling of the sputtering rate, and  $T_o$  is the temperature that is above the temperature at which the sputtering rate flattens, so the dust mass becomes :

$$\left(\frac{dM_{dust}}{dt}\right) = \frac{-M_{dust}}{\tau_{sp}/3} \quad (13)$$

## SIMBA dust destruction

Dust destruction results from the star-formation sputtering consumption and SNe shocks.

It is calculated as :

$$\left(\frac{dM_{dust}}{dt}\right)_{de} = \frac{-M_{dust}}{\tau_{de}} \quad (14)$$

The characteristic time scale is  $\tau_{de} = \frac{m_g}{\epsilon \gamma m_s}$  and the efficiency  $\epsilon = 0.3$ . Where  $m_g$  is the local gas mass,  $\gamma$  is the local SNII rate,  $m_s = 6800 E_{SNII,51} \left(\frac{v_s}{100 km/s}\right)$ ,  $E_{SNII,51}$  is the energy released by the SNII, and  $m_s$  shocked local gas mass, at about 100 km/s.

## 1.5 EAGLE hydrodynamic cosmological simulations.

We employed other hydrodynamic simulations galaxies to compare the SIMBA simulated galaxies with other simulated galaxies from other cosmological simulations that have done similar work. In particular, EAGLE database catalogue published in [Camps et al. \(2016\)](#) 2016 paper. The employed database contains the galaxies' mock fluxes, as they are already processed in [Camps et al. \(2016\)](#) project. As a result, we do not process or create mock fluxes as we did with SIMBA. We reproduce the SIMBA galaxies' scaling relations in this EAGLE data to see which simulation's sub-grid model reproduces observational or real galaxies' scaling relations better.

EAGLE is a campaign of large-scale hydrodynamical simulations of the Lambda-Cold Dark Matter universe, run by the Virgo Consortium ([Schaye et al., 2015](#)). This N-body/SPH, GADGET<sup>9</sup> code simulation is known for its galaxy formation and co-evolution of gaseous environments. It was designed to reproduce the local universe stellar mass function, the  $H_2$  galaxy mass function, the mass-size mass function, and many other observable relations ([Baes et al., 2019](#)). This simulation's physical processes and tracking systems are similar to other cosmological hydrodynamic simulations. However, unlike SIMBA, EAGLE cannot model the cold gas phase in the ISM. Therefore, to prevent artificial fragmentation of the star-forming gas, EAGLE's ISM does not have a molecular cloud but rather smoothly distributes pressured gas and a metallicity-dependent density threshold ([Baes et al., 2019](#)). Through scaling relation, [Camps et al. \(2016\)](#) has proven that the EAGLE simulation can reproduce many observed galaxy properties relations, including the observed galaxy dust mass scaling relation shown in Figure 6. However, [Camps et al. \(2016\)](#) also found some discrepancies in the EAGLE simulation's f250/f350 versus f350/f500 submm colour-colour relation, which they believe the discrepancy implied that part of the simulated dust is insufficiently heated. In this work, we repeat these relations to test SIMBA's performance and also to understand SIMBA galaxies' dust properties better. Note that, in this project, we employed the 'RefL0100N1504' EAGLE snapshot that was already processed and SKIRT-simulated in [Camps et al. \(2016\)](#).

---

<sup>9</sup>A free cosmological N-body/SPH simulations software

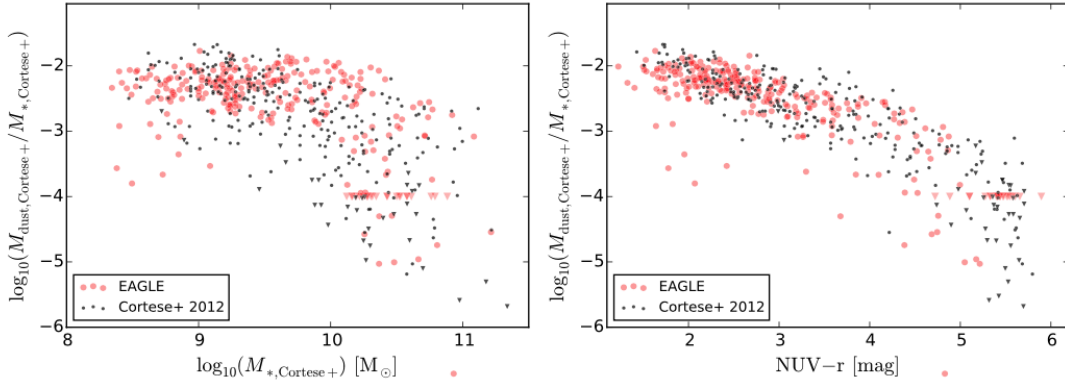


**Figure 6:** The EAGLE galaxies dust scaling relations from [Camps et al. \(2016\)](#) (figure 12).

## 1.6 The problem with cosmological simulations

Cosmological simulation models are limited because galaxy evolution and formation physics are not yet fully understood. For example, essential processes such as star formation, BH growth and evolution, AGN, and supernovae feedbacks are modelled using sub-grid recipes. It has been proved that many cosmological simulations can mimic some but not all of the observational galaxies' properties due to a poor understanding of these essential physical processes ([Vogelsberger et al., 2014](#); [Schaye et al., 2015](#); [Davé et al., 2019](#)). All cosmological simulations have unique features that make them different, and the main goal of all the simulations is to improve the understanding of galaxy formation and evolution. Therefore, comparing the cosmological simulation's performance with observations and other simulations helps improve the existing sub-grid prescriptions and betters the understanding of galaxy formation and evolution.

## 1.7 SKIRT

Without dust attenuation, most hydrodynamic simulations do not reproduce precise observations. This limitation has shown that simulations need dust modelling to reproduce observations; for example, the most recent work done by [Hahn et al. \(2022\)](#) on SIMBA, EAGLE, and TNG. [Hahn et al. \(2022\)](#) presented a dust attenuation framework that models dust attenuation in simulated galaxies using the galaxies' physical properties. we need a dust modelling technique to compare simulated galaxies with observations successfully. In addition to dust modelling, the hydrodynamic simulation galaxies are in 3-dimensional galaxy mass distributions (gas, star, and dark matter). The observational data used for

comparison is in 2-dimensional sky observational fluxes. To succeed in this project's goal, we created 2-dimensional realistic mock observations of the simulations' 3-dimensional mass distribution. To do so, we used the SKIRT radiative transfer code for the galaxies' dust modelling and generated the simulation's mock 2-dimensional observational fluxes.

SKIRT<sup>10</sup> is an acronym for Stellar Kinematics Including Radiative Transfer. It was primarily designed to study the kinematics of dusty galaxies by evaluating all the fundamental dust and radiation processes observed in the galaxies. This Monte Carlo code can produce several images and spectral energy distributions (SEDs) at various observables by peeling off the photon packages (Camps & Baes, 2015). It is a C++ code that considers the complete absorption and anisotropic scattering dust treatment. It calculates the dust temperature distribution and thermal dust re-emission self-consistently and uses efficient libraries to support small grains of stochastic heating. The code is deployable in Unix systems, and the user can access it in their terminal once it is installed. The simulation configuration is saved in an eXtensible Markup Language (XML) that can be easily edited using a text editor. This code is not only applicable in dusty galaxies but also AGN (Stalevski et al., 2012), stellar systems (Deschamps et al., 2015), and molecular clouds (Hendrix et al., 2015). In Camps et al. (2016), SKIRT was used to produce SEDs and integral field spectroscopy data cubes. In Trčka et al. (2020), it was used to create SED and inferred physical properties from UV-submm wavelength. Similar to Trčka et al. (2020), this work uses SKIRT to derive SIMBA mock fluxes from UV-submm wavelengths from SIMBA hydrodynamic simulation inputs.

## 1.8 The research aim, objective, significance, and questions

### Aim

This project aims to test the degree to which the SIMBA hydrodynamic cosmological simulations succeeded in mimicking DustPedia observational galaxies and compare the simulations' performance with the EAGLE hydrodynamic cosmological simulations.

---

<sup>10</sup>[https://skirt.ugent.be/root/\\_landing.html](https://skirt.ugent.be/root/_landing.html)

## Objectives

1. To use the SKIRT radiative transfer code to derive the simulation's mock observational fluxes for direct comparison between the simulated and real galaxies;
2. Derive physical properties using the SKIRT mock fluxes; and
3. Study the ISM scaling relations in SIMBA cosmological simulations.

## Research questions

1. Do SIMBA simulated galaxies' scaling relations reproduce observational galaxies scaling relations?
2. How does the performance of SIMBA's simulation compare to others, particularly EAGLE's simulation?

## Research significance

SIMBA is a new cosmological hydrodynamic simulation that has a unique recipe for dust physics included in the simulation itself. It employs advanced BH and accretion feedback models, uses a modified post-processing procedure, and does not require populating the galaxies with dust grains. Therefore, this work tested the latest simulation modelled with advanced dust models and will contribute to advancing our understanding of hydrodynamic simulation's sub-grid models, galaxy formation, and its evolution. The more a simulation is close to observation implies correct modelling physics, which will bring solutions or validations to the studies' theoretical physics.

## 1.9 Project limitations

This work tests the fidelity of the SIMBA galaxy evolution model by comparing it with DustPedia observations and EAGLE simulations. The project focuses only on simple scaling relations dependent on SKIRT synthetic broadband fluxes. We do not derive the inferred physical properties using the SED fitting as in [Boquien et al. \(2019\)](#); [Trčka et al. \(2020\)](#) but rather derive them using simple equations that depend entirely on the synthetic broadband fluxes.

The project's initial aim includes studying and comparing the synthetic HI data in SIMBA simulations and observations since they are already available in SIMBA. However, we had to narrow it down because SKIRT's HI data was not yet generated when this analysis was conducted.

Scaling relations help test the accuracy of a cosmological simulation; however, they cannot be used independently to make final decisions. Two different populations of galaxies, one from simulations and the other from observations, can lie in a similar sequence in luminosity scaling relation; for example, in a case where the simulated galaxy population has too many luminous galaxies. More statistical populations can boost the scaling relation tests for firmer conclusions; for example, the luminosity functions, stellar mass functions, and SFR functions (Baes et al., 2019, 2020), which have not been considered in this work but have been noted for future work.

## 1.10 Thesis Overview

This thesis consists of five chapters. This chapter, Chapter 1, briefly introduced the study alongside a literature review. Chapter 2 will discuss the methodology used in this study, whilst Chapter 3 will discuss the results obtained from the chosen method. The final chapter of this work is Chapter 4, presenting the conclusions and findings of this study.

## 2 Method

This chapter outlines all the steps taken in this project. It consists of five sections. The first three sections (2.1, 2.2 and 2.3) describe the methods used to deal with data from the SIMBA and EAGLE cosmological simulations and DustPedia observational data. Thereafter, Section 2.4 provides the statistical tests and finally Section 2.5 set out the method limitations encountered.

The project studied extensive data from SIMBA simulations (Davé et al., 2019), EAGLE simulations (Schaye et al., 2015), and the DustPedia observational database (Davies et al., 2017). Unlike the SIMBA data, the EAGLE and DustPedia data used in this project were taken from previous literature (Camps et al., 2016; Trčka et al., 2020) and were already post-processed and simulated through SKIRT. On the other hand, the SIMBA data was taken from a high-resolution snapshot that requires high computational power and memory, which a regular computer could not handle. The snapshot contains about 2400 galaxies, which needed 2.5T of memory and 32 cores to complete the SKIRT simulation run and data analysis for all the selected galaxies. Since a personal computer does not have that much capacity, we applied to do all the data collection and analysis in the Inter-university Institute for Data-Intensive Astronomy (IDIA) research cloud infrastructure facilities<sup>11</sup>. Within the IDIA facilities, we wrote simple python scripts that use common python modules and packages to extract the galaxies from their snapshot. In the scripts, the galaxies are identified by their galactic centre coordinates provided by the SIMBA general galaxy catalogue publicly available on the SIMBA website. For this project, we focused on the redshift zero ( $Z = 0$ ) SIMBA snapshot labelled 'snap\_m25n512\_151'. We applied stellar mass and sSFR selection criteria that ensured the selection of galaxies with an active ISM. The selected galaxies were within a stellar-mass range of  $10^9 M_{\odot} \leq M_{*} \leq 10^{11.5} M_{\odot}$ , and a sSFR range of  $10^{10.5} yr^{-1} \leq sSFR \leq 10^7 yr^{-1}$ .

---

<sup>11</sup><https://www.ilifu.ac.za/>, accessed 15 September 2022

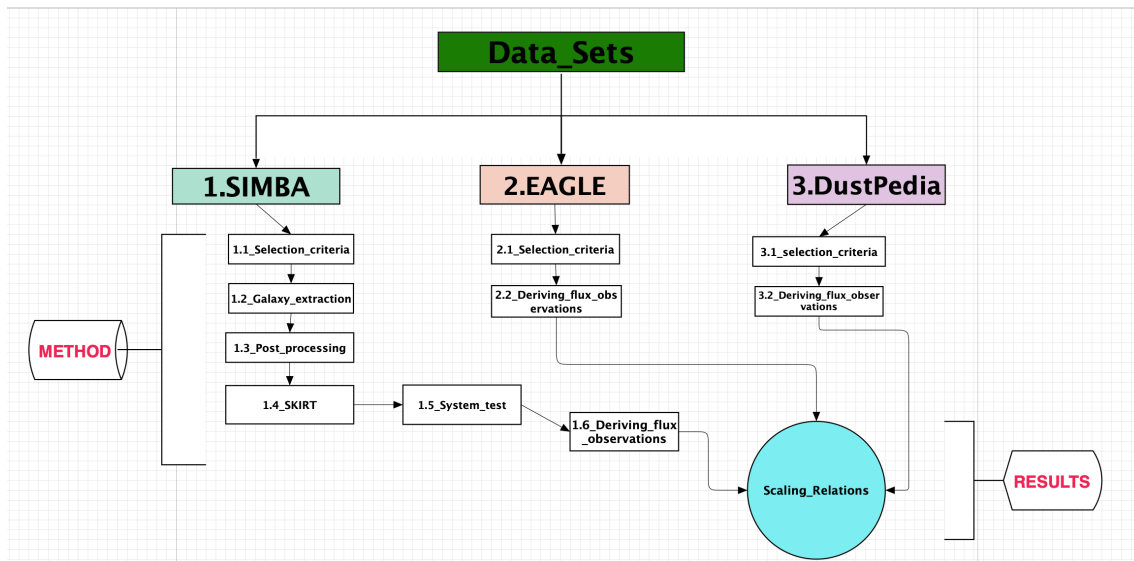


**Figure 7:** The project’s methodology schematic overview. Only the SIMBA galaxies were post-processed and simulated with SKIRT in this project. The EAGLE galaxies were already post-processed and had mock fluxes from Camps et al. (2016). The DustPedia observational galaxies were ready for analysis and taken from Trčka et al. (2020)’s project. The main goal of all the steps taken was to do the scaling relations for the simulated galaxies and compare them with the observational galaxies scaling relations. See full text in Chapter 2 for further details of this methodology.

UNIVERSITY of the  
WESTERN CAPE

Figure 7 above presents this study’s methodology flow chart. Its flow summarises the procedures carried out toward the undertaking of this project. We began by collecting the SIMBA, EAGLE, and DustPedia galaxies’ datasets from different sources. SIMBA data were made available by the SIMBA team (Davé et al., 2019). EAGLE data were taken from Camps et al. (2016) and DustPedia data were taken from Trčka et al. (2020). As seen in Figure 7, SIMBA is the primary dataset of this project; hence processing it was lengthy compared to the other two datasets adopted from previous literature for comparison, as discussed above.

Processing SIMBA data included extracting galaxies from their snapshot, post-processing them using Camps et al. (2016)’s procedure, simulating the galaxies with SKIRT, running some system tests, and deriving the galaxies’ physical properties using the SKIRT output fluxes. In addition, the recipes or methods used to estimate the galaxies’ physical proper-

ties in this work and the techniques used in EAGLE and DustPedia datasets are different. So we also derived the physical properties for EAGLE and DustPedia galaxies using similar procedures used for SIMBA data. After all the derivations, we performed the ISM scaling relation, and all findings are detailed in Section 3.

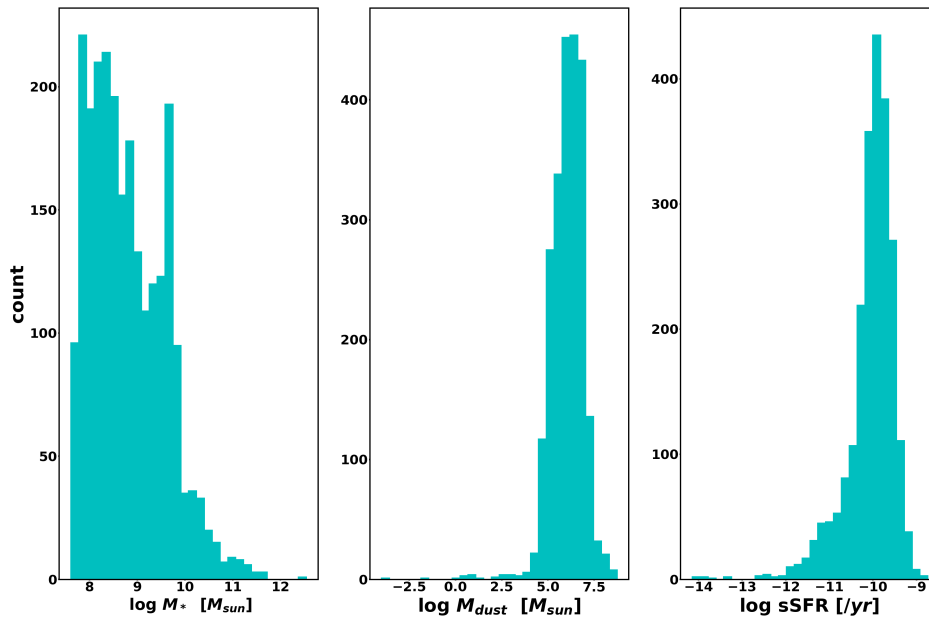
## 2.1 Methodology for dealing with SIMBA data

There are four publicly available SIMBA simulation snapshots, starting from  $z=20$  to  $z=0$ . The Planck cosmological parameters for each snapshot is  $\Omega_m = 0.3$ ,  $\Omega_\Lambda = 0.7$ ,  $\Omega_b = 0.048$ ,  $H_\odot = 68 \text{ km.s}^{-1} \text{ Mpc}^{-1}$ ,  $\sigma_8 = 0.82$ , and  $n_s = 0.97$ . The galaxies studied in this work were extracted from the SIMBA full physics snapshot box ( $z=0$ ), which contains a high-resolution run. The snapshot is a  $25 \text{ Mpc}/h$  box with a minimum gravitational softening length of  $0.25 \text{ Kpc}/h$ , an initial gas element mass resolution of  $2.85 \times 10^5 M_\odot$ , a dark matter particle mass resolution of  $1.5 \times 10^6 M_\odot$ , and spatial stellar masses resolution of  $9.1 \times 10^6 M_\odot$ . Details are summarised in Table 1 of [Davé et al. \(2019\)](#). In total, the snapshot contains 2411 galaxies in the stellar mass range  $10^{7.5} M_\odot \leq M_* \leq 10^{12.5} M_\odot$ , dust mass range  $10^{-4} M_\odot \leq M_{dust} \leq 10^{8.5} M_\odot$ , and specific star-formation rate (sSFR) range  $10^{-14} \text{ yr}^{-1} \leq sSFR \leq 10^{-9} \text{ yr}^{-1}$ , as shown in Figure 8.

### 2.1.1 Criteria for selecting galaxies in the SIMBA snapshot

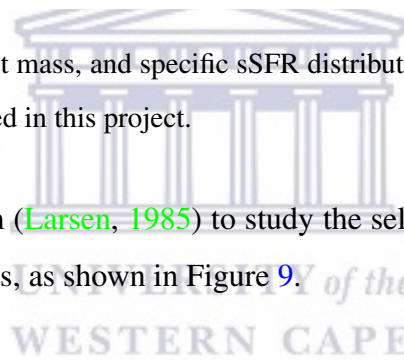
The main interest of the project was to study the ISM of galaxies. However, not all galaxies have an active ISM. An example is the massive elliptical galaxies in which gas reservoirs have generally run out. To ensure we study galaxies with an active ISM, we used selection criteria that excluded galaxies with low star formation. In particular, we selected galaxies that satisfied the following two conditions, an  $sSFR \geq 10^{-10.5} \text{ yr}^{-1}$  and a galaxy stellar mass  $M_* \geq 10^9 M_\odot$ . The selection criteria were motivated by our interest in studying the scaling relations of highly resolved galaxies with an active interstellar medium. The galaxy stellar mass threshold was because of the used SIMBA snapshot and the black hole seeding and dynamics employed by the simulation. The simulation places black holes in galaxies with  $M_* \geq 10^{9.5} M_\odot$ , and according to the snapshot resolution, galaxies within this range are highly resolved and coupled with the sSFR threshold resulted in the selection of active ISM galaxies only.

After applying the selection criteria, we had 264 SIMBA galaxies to study. We used



**Figure 8:** The stellar mass, dust mass, and specific sSFR distribution for all the SIMBA galaxies contained in the snapshot studied in this project.

the box and whisker diagram (Larsen, 1985) to study the selected galaxies' stellar mass, dust mass, and sSFR statistics, as shown in Figure 9.



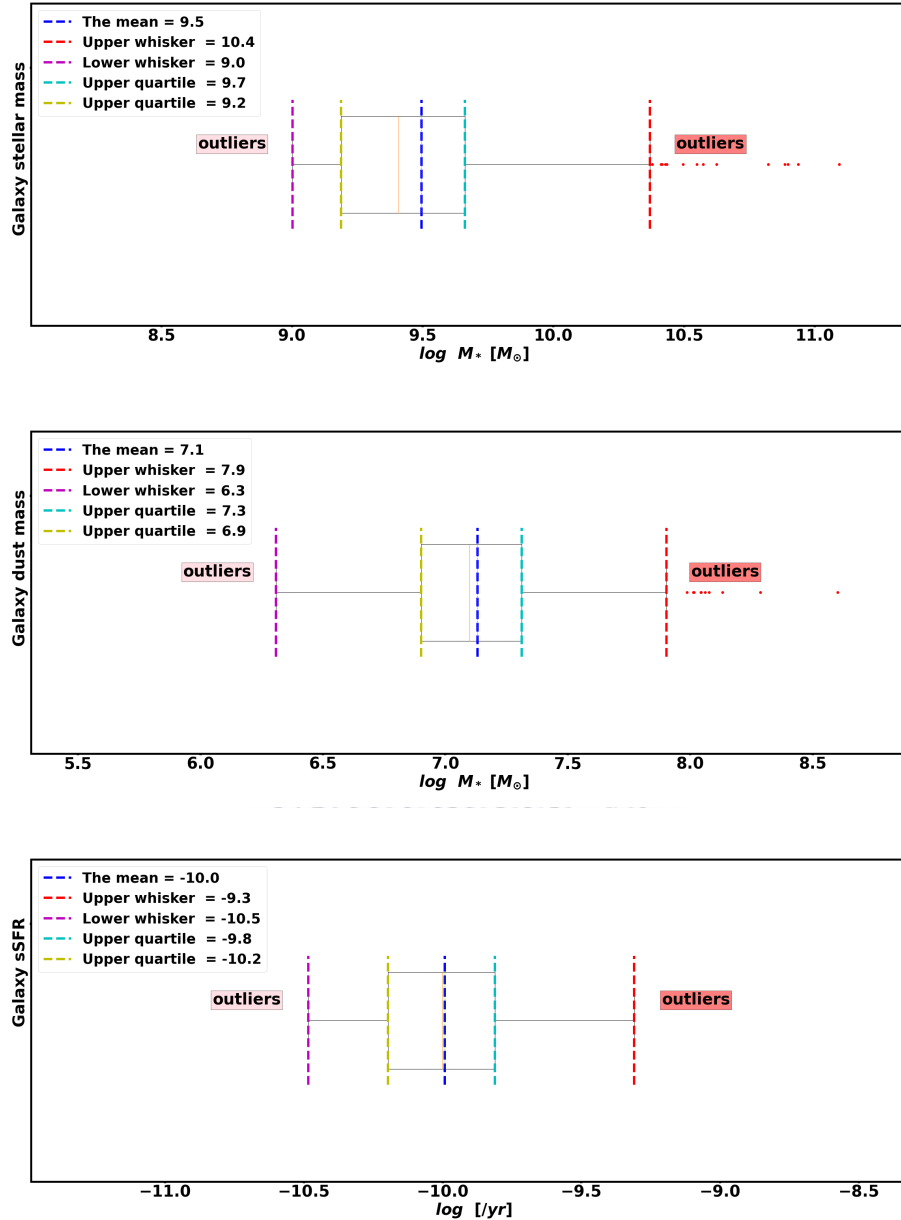


**Figure 9:** The stellar mass, dust mass, and specific star-formation box and whisker diagrams (from top to bottom) for all the selected SIMBA galaxies. The vertical dashed lines are colour-coded as follows: data mean (blue), lower whisker (purple), upper whisker (red), lower quartile (yellow), and upper quartile (cyan).

The box and whisker stellar mass diagram in the top panel of Figure 9 shows that the selected SIMBA galaxies' stellar masses range from a minimum stellar mass of  $10^{9.0}M_{\odot}$  to a maximum of  $10^{11.1}M_{\odot}$ , with an average and median of  $10^{9.5}M_{\odot}$  and  $10^{9.4}M_{\odot}$  respectively. The galaxies are as follows: 132 galaxies (50%) lie between  $10^{9.2}M_{\odot} \leq M_* \leq 10^{9.7}M_{\odot}$ , 66 galaxies (25%) are lower stellar mass galaxies ranging between  $10^{9.0}M_{\odot} < M_* \leq 10^{9.2}M_{\odot}$ , and 51 galaxies (20%) are higher stellar mass galaxies ranging between  $10^{9.7}M_{\odot} < M_* \leq 10^{10.4}M_{\odot}$ . Lastly, the dataset also has a few (15) massive galaxies in the stellar mass range  $M_* > 10^{10.4}M_{\odot}$ , shown as outliers in the box and whisker plot. The box skews towards the left because the selection criteria selected many lower mass galaxies  $< 10^{9.5}M_{\odot}$  with high SFR.

The middle panel in Figure 9 shows the selected SIMBA galaxies' dust mass distribution, starting from a minimum of  $10^{6.3}M_{\odot}$  to a maximum of  $10^{8.6}M_{\odot}$  with an average and median of  $10^{7.1}M_{\odot}$  and  $10^{7.1}M_{\odot}$  respectively. Out of the 264 selected SIMBA galaxies, 131 (50%) range between  $10^{6.9}M_{\odot} < M_{dust} \leq 10^{7.3}M_{\odot}$ , 66 (25%) range between  $10^{6.3}M_{\odot} < M_{dust} \leq 10^{6.9}M_{\odot}$ , 20% (55) range between  $10^{7.3}M_{\odot} < M_{dust} \leq 10^{7.9}M_{\odot}$ , with some 12 (10%) outliers above  $10^{7.9}M_{\odot}$ .

The bottom panel in Figure 9 shows the sSFR distribution, which starts from a minimum of  $10^{-10.5}yr^{-1}$  to a maximum of  $10^{-9.3}yr^{-1}$  with an average and median of  $10^{-10.0}yr^{-1}$  and  $10^{-10.0}yr^{-1}$  respectively. As can be seen from the figure, 134 (50%) galaxies range between  $10^{-10.2} < sSFR[yr^{-1}] \leq 10^{-9.8}$ , 65 (25%) are lower sSFR galaxies ranging between  $10^{-10.5} < sSFR[yr^{-1}] \leq 10^{-10.2}$ , and 65 (25%) are higher sSFR galaxies in the range of  $10^{-9.8} < sSFR[yr^{-1}] \leq 10^{-9.3}$ . The SIMBA galaxies' sSFR distribution is symmetric.

### 2.1.2 Extraction of galaxies in the SIMBA snapshot

This section describes how we extracted the SIMBA galaxies from their parent snapshot using a python script and python functions. The script had two functions, the 'loadsnap' and the 'extract' functions, and both scripts used common python packages like NumPy, shutil, os, sys, h5py, math, and some astronomy packages like caesar. The functions are divided into two to avoid reloading the same snapshot repeatedly. The **loadsnap** function

read into the snapshot and extracted all the gas and stellar data from the snapshot. The **extract** function extracted the selected galaxy using the galaxy's central coordinates.

### **The loadsnap function**

Loadsnap functions took in the snapshot path as input and read the snapshot information, such as the Hubble parameter, redshift, box size, expansion factor, and the number of files in the snapshot. After reading the general information about the snapshot, it created stars and gas dictionaries that were later filled with the corresponding particle information. The code reads all the gas and stellar particle information for each galaxy inside the snapshot and concatenates the particle information into the created dictionaries. SKIRT has specific acceptable units for its input sources, and SIMBA simulation units are not SKIRT-friendly; they had to be changed from co-moving to physical units. To do so, we used CAESAR<sup>12</sup> and common python libraries, such as NumPy and matplotlib. All unit conversions were done within the 'loadsnap' function, and the function's output files comprised the gas, dust, and stellar particle information for all the galaxies in the snapshot.

### **The extract function**

The **extract** function extracted specific galaxy information as needed for this study. It took the **loadsnap** output files, the galaxy centre coordinates of the desired galaxies<sup>13</sup>, and prefixed names as inputs to the function. The code identified the galactic centre as the origin for initial extraction, then extracted all particles within 150 kpc aperture radius such that all particles centred outside this diameter were ignored or removed. The code searched for the galaxy's centre of mass from the extracted galaxy particles using the galaxy's stellar particle information. Once the galaxy's centre of mass was identified, the particles were rearranged to be centred around the newly identified centre of mass. For the 3D geometric modelling of the galaxies, the code finds the unit rotational axis and vectors using the stellar information within the given aperture. After that, it aligned the vector

---

<sup>12</sup>CAESAR is a module designed to analyse cosmological simulation output files, and it is also a helpful unit conversion tool. This module can read the original simulation binary snapshot and create a new Hierarchical Data Format version 5 (HDF5) catalogue file containing the host galaxy and halo particle information (Davé et al., 2019; Glowacki et al., 2020)

<sup>13</sup>The galactic centre coordinates are accessible in the SIMBA 25 cMpc catalogue Davé et al. (2019)

quantities with the stellar angular momentum axis. Once the alignment was complete, the code ran another aperture extraction, identifying the new galaxy's centre of mass as the galactic centre and extracting all particles within a 30 kpc radius from the galaxy's centre of mass. All the extracted galaxies had a fixed diameter of 60 kpc, and particles outside this diameter were ignored. The code separated the extracted particles into three groups. The star-forming region particles were selected based on their stellar age<sup>14</sup>. The final output text files contained particle information of the dust, stars, star-forming regions, and the snapshot general information data file.

### 2.1.3 Post-processing SIMBA data with SKIRT

The aim of post-processing the SIMBA galaxies before simulating them in SKIRT is to ensure that the hydrodynamic simulations input files have all the regions and are in a format acceptable for the SKIRT code and will produce the desired results. This section explains how the extracted simulation output sources were prepared for the SKIRT radiative transfer code. This procedure occurred during galaxy extraction and was included in the extract python script, discussed in Section 2.1.1. The galaxy particles from the snapshot were not divided into stellar, dust, and star-forming region particles; they were either gas or star particles. The post-processing procedure helped create the files of each galaxy's stellar, dust, and star-forming region particles. These files were necessary for the SKIRT radiative transfer simulation. Table 3 below shows the SKIRT input files' required parameters and units. In the table, parameters with asterisks (\*) denote derived parameters, meaning these values were unavailable in the snapshot. Values without asterisks (\*) were directly extracted from the snapshot. After extraction, the galaxy outputs contained two primary emission sources, namely the stellar and star-forming particles and the galaxy medium file (ISM dust), as required in the SKIRT code. In this work's procedure, the stellar region particle information was taken directly from the snapshot star particles, the galaxy medium or dust was taken from the snapshot gas particles, and the star-forming region particles were derived following Groves et al. (2008) and Kapoor et al. (2021)'s procedures. The details on how each particle was assigned a region or SED template are described in the following paragraphs.

---

<sup>14</sup>All stellar particles less than  $10^7$  years are star-forming region particles

<b>SKIRT INPUT FILES</b>	
<b>Stellar</b>	
Stellar data	Units
3D Coordinates	kpc
smoothing length	kpc
Initial particle mass*	$M_{sun}$
Metallicity	1
Age	Gyr
<b>Dust</b>	
Dust data	Units
3D Coordinates	kpc
smoothing length	kpc
Dust particle mass	$M_{sun}$
<b>SFR</b>	
Star-forming region data	Units
3D Coordinates	kpc
smoothing length	kpc
SFR*	$M_{sun}/yr$
Metallicity	1
Compactness*	1
ISM Pressure*	Pa
Covering Factor*	1

**Table 3:** This table shows the galaxy information and corresponding units in each simulation output file (SKIRT inputs). The asterisks (\*) indicate the derived or calculated parameters.

### Star-forming region particles

This section describes how the star-forming region particles were assigned their MAPPING III SED template (Groves et al., 2008). These particles were extracted directly from the snapshot and were the galaxies' star particles younger than 10 Myrs. The MAPPING III SED template wavelength ranged from 1 angstrom to 1 m. It had a spectrum

of 1800 wavelength bins covering five metallicities, five pressures, six compactness parameters, and two covering factors. Below is a summary of how each star-forming region parameter was derived:

- For **SFR**, the assumption was that all-star particles with age lesser than 10 Myr were star-forming, the HII regions for stellar-mass conservation, as suggested in [Camps et al. \(2016\)](#). The SFR was calculated as the particles' mass divided by  $10\text{Myr}$  ( $M_*/10\text{Myr}$ ), assuming a constant SFR for  $10\text{Myr}$ .
- **Metallicity (z)** was extracted directly from the SIMBA snapshot star particles.
- The **compactness parameter (C)** is known as the dust temperature distribution proxy ([Groves et al., 2008](#)). In SKIRT9, this parameter varied between  $4.0 \leq \log(c) \leq 6.5$ . To calculate this parameter, we approximated a log-normal distribution with a standard deviation of 0.4 and  $\langle \log C \rangle = 5$ . The compactness parameter value for each star-forming particle was randomly sampled from the derived log C distribution ([Rodriguez-Gomez et al., 2019](#); [Vogelsberger et al., 2020b](#)).
- The **ISM pressure** was calculated using Equation 13 of [Groves et al. \(2008\)](#) for each star-forming particle. This parameter only affects the number of emission line strengths but not the shape of the SED template.
- The **covering factor of the photo-dissociation region (PDR)** provided the radiative feedback of stars from their parent or molecular clouds. The covering fraction of the PDR (fPDR) provided the fraction or amount of the molecular cloud covering the surrounding galaxy star cluster. This fraction range between 0 and 1, where 0 means uncovered (or no molecular clouds) and 1 implies full covering. For this work we employed the SKIRT default value of 0.2 for covering ([Groves et al., 2008](#); [Jonsson et al., 2010](#); [Rodriguez-Gomez et al., 2019](#)), and ([Vogelsberger et al., 2020b](#)).

### Stellar particles

Galaxy stellar particles above 10 Myr were assigned to the [Bruzual & Charlot \(2003\)](#) SED Family template. The temple consists of two assumed initial mass models, namely the Chabrier and Salpeter ([Treu et al., 2010](#)). The Bruzual-Charlot initial mass model

could be used when parameterised by metallicity, age, and initial mass; with two high and low wavelengths of 1221 and 6900 points, respectively. In this work, we used [Bruzual & Charlot \(2003\)](#) high wavelength resolution (6900 points) Chabrier initial mass function (IMF) template for these particles.

## Dust particles

The dust particles were extracted directly from the snapshot and assigned the THEMIS dust model ([Jones et al., 2017](#)). The THEMIS model has two families of amorphous hydrocarbons and amorphous silicates. It has a self-consistent treatment for the dust material properties, as they interact with the local radiation field intensity and the dynamics of the gas density. The model's interstellar dust is heterogeneous due to mantle accretion, grain surface photoprocessing, and coagulation.

### 2.1.4 Treatment of the SIMBA data with SKIRT

Once we post-processed or prepared SIMBA galaxies, we import the hydrodynamic simulation's output sources as inputs in SKIRT. To import the galaxies in SKIRT, we created a "ski" file in the SKIRT user-friendly question-and-answer coded environment. This file defines all the desired simulation parameters, and this section presents the simulation parameters used for SIMBA galaxies in SKIRT. Table 4 after that presents the wavelength bands studies in this work.

The simulation took in three galaxy sources, two primary sources and one medium source because we used the Panchromatic simulation mode, which works in a range of wavelengths from UV-submm and includes secondary emissions by the medium in addition to primary sources. The primary sources are the stellar and SFR data. The stellar populations (stellar data) were assigned the Bruzual-Charlot SED Family template, and the star-forming populations (SFR data) were assigned the Mappings SED Family template. The Medium source was the galaxy dust data. We chose the dust model type to be the THEMIS dust mixture model composed of amorphous silicates and amorphous hydrocarbons.

We released  $5 \times 10^8$  photons packets for each simulation run in each wavelength. We ap-

plied extragalactic system units, pc unit length; Mpc unit of distance;  $\mu m$  unit of wavelength; and  $M_{\odot}$  unit of mass. The flux density and surface brightness were in frequency, spatially integrated flux in Jansky ( $Jy$ ), and surface brightness in  $M Jy sr^{-1}$ .

### 2.1.5 Spectral energy distribution

The SKIRT SED instrument outputs both the intrinsic stellar radiation (no dust) and SF region dust re-processed emission at higher wavelength. This section shows the reader the SED examples we produced with SKIRT when processing SIMBA galaxies. The SEDs are different for the various galaxies, some galaxies are dustier than others, and the effect of dust is shown clearly at lower wavelengths. The SEDs also show differences due to the employed post-processing procedure when forming the star-forming SKIRT input source. In each of the presented examples of SEDs, Figure 10 and Figure 11, the blue line shows the intrinsic stellar SED (Transparent flux), and the red line shows the observed SED (Total detected flux).

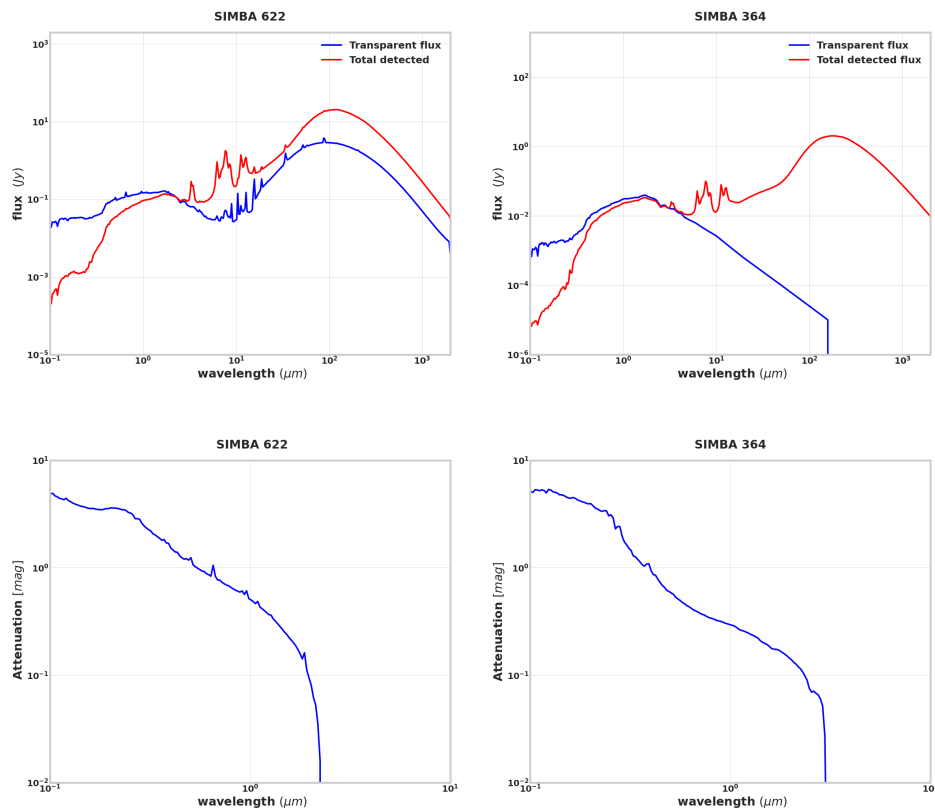


**Figure 10:** Example of the SKIRT output SED of SIMBA dustier galaxies in the top row, and their respective attenuation curve in the bottom row.

SIMBA BAND LIST		
Index	Band Name	Wavelength (microns)
0	GALEX_GALEX_FUV	0.1535
1	GALEX_GALEX_NUV	0.2301
2	SLOAN_SDSS_U	0.3556
3	SLOAN_SDSS_G	0.4702
4	SLOAN_SDSS_R	0.6176
5	SLOAN_SDSS_I	0.7490
6	SLOAN_SDSS_z	0.8947
7	2MASS_2MASS_J	1.2392
8	2MASS_2MASS_H	1.6494
9	2MASS_2MASS_KS	2.1638
10	WISE_WISE_W1	3.3897
11	WISE_WISE_W2	4.6406
12	WISE_WISE_W3	12.5676
13	WISE_WISE_W4	22.314
14	HERSCHEL_PACS_70	70.7698
15	HERSCHEL_PACS_100	100.802
16	HERSCHEL_PACS_160	161.892
17	HERSCHEL_PACS_250	252.549
18	HERSCHEL_PACS_350	354.272
19	HERSCHEL_PACS_500	515.3633

**Table 4:** The UV to submm wavelength band lists detecting the SKIRT fluxes and their corresponding wavelengths.

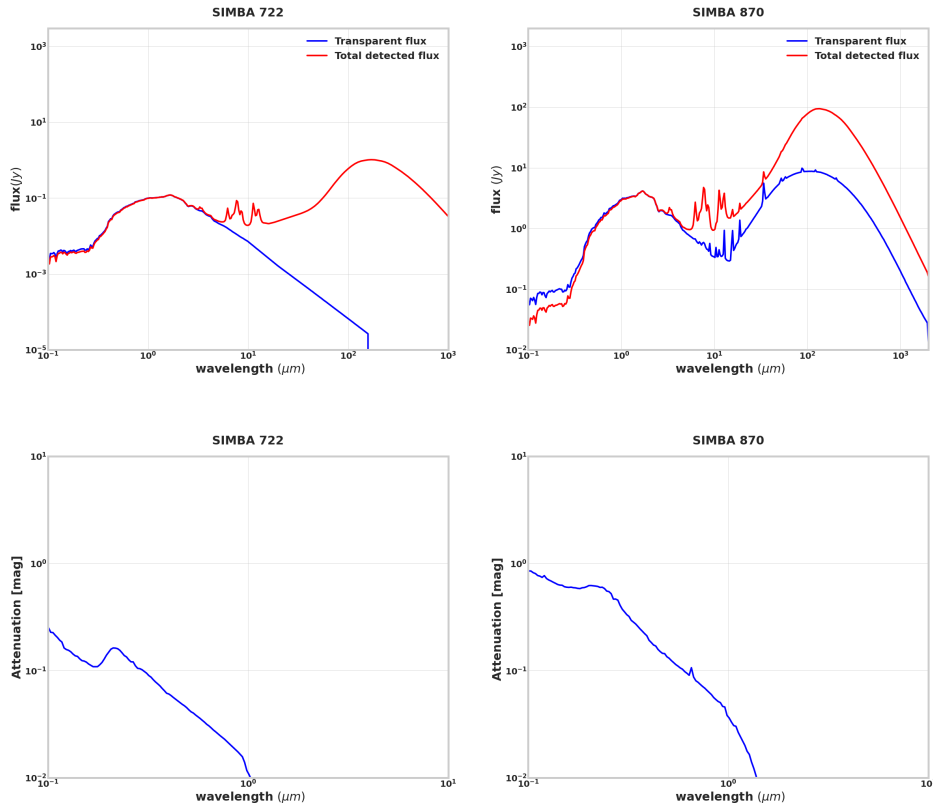


**Figure 11:** Example of the SKIRT output SED of SIMBA less dustier galaxies in the top row, and their respective attenuation curve in the bottom row.

Referring back to Figure 6 of Camps et al. (2016), where it shows the different galaxy properties and the common emission wavelengths from UV to submm, we are reminded that the galaxy stellar emission is expected a lower wavelength, starburst emission should be around  $10\mu m$ , and dust emission is always at higher wavelength. The SED templates that we have created also tell us more about the galaxies' properties at different wavelengths.

When selecting the galaxies for this work, the selection criteria were to ensure that we study actively star-forming galaxies. But interestingly, one may question why are we having galaxies that are showing no SFR, for example, galaxy 364<sup>15</sup> in figure 10. The SED only has stellar emission and no star formation activities, yet only star-forming galaxies were selected. Yes, the intrinsic SED of galaxy 364 has no starburst emission, but that does not mean galaxy 364 is not star-forming. But this is due to the way the SFR SKIRT input file was created in the post-processing (section 2.1.3). In the post-processing

<sup>15</sup>galaxy 364 is just a galaxy ID/name

procedure, the SIMBA 364 galaxy intrinsic SED has stellar emission only because the galaxy stellar particles are all older than 10Myr. As a result, the SFR SKIRT input file had no SFR particles. But In the case of galaxies like SIMBA galaxy 622 in Figure 10, the galaxy has stellar particles that are younger than 10 Myr which are identified as the star-forming region for the SKIRT stellar input sources post-processing procedure. Hence SIMBA 622 galaxy has stellar emission at lower wavelengths, starburst emission around  $10\mu m$ , and dust emission at higher wavelengths. Moreover, when both galaxies get radiative transferred in the dusty system (SKIRT), we get detection for all bands in all wavelengths from UV to submm (the red SEDs).

### **Dust effect can be seen on the SEDs templates**

Dust grains play a vital role in observations and mainly affect starlight emission at lower wavelengths. Now I show the effect that dust has on the detected fluxes. Figure 10 and figure 11 are the sample SEDs from this work taken to serve as an example in this section. The x-axis is the wavelengths in microns, the y-axis is the detected flux in jansky, and the red and blue SEDs are the detected and intrinsic SEDs, respectively. Figure 10 shows the SEDs of SIMBA dusty galaxies. In this plot, the difference between the intrinsic and detected flux at lower wavelengths is too high in dusty galaxies (shown in the attenuation curve below). The plot shows that more flux is detected at lower wavelengths in the absence of dust (blue SED). However, in the presence of dust (red SED), the starlight is distracted mainly by the scattering and absorption of the dust grains as the stellar light radiated through the medium and is expected in observations. In the same sample, some galaxies are behaving like galaxies SIMBA 722 and SIMBA 870 in figure 11. The flux detected in the dusty SED is not too different from the intrinsic SED, meaning this system does not have much dust attenuation, and most of its starlight is detected and not scattered or absorbed by any dust grains. Which can only be true in simulations since dust is always and more present in observations. In summary, here we show the effect that dust has on observations and that some galaxies are forming more stars than others.

### 2.1.6 SKIRT system tests

After importing the first SIMBA sources in SKIRT and ensuring that SKIRT accepted and ran the hydrodynamic simulation output files successfully, we had to perform system tests. These tests were performed before running the remaining galaxies in the code. The test ensured that we used resources reasonable by minimising the computational power and time <sup>16</sup> used for each simulation, whilst also ensuring that the results we obtained were reliable.

#### Spatial grid convergence test

The simulation employed the octree dust grid structure. This structure runs in a loop format of nodes that start as cuboidal nodes and cover the entire dust medium. The spatial grid convergence test determines which spatial grid node and maximum dust fraction mass level yield the best results at the lowest computational power and time. This test simulates the same galaxy through four iterations, changing the maximum dust fraction in each simulation run.

We knew the first run needed more computational power, smaller grid cells, and time, which we provided. Thus, we referred to this run as the most satisfactory or superfine result. Its spatial grid node levels ranged from 6 to 12, with a maximum dust fraction of  $1e-7$ . This simulation took, on average, 40 hours and 53.4 Gigabytes (GB) of memory to complete. Although a maximum dust fraction of  $1e-7$  gives satisfactory results, it requires a lot of computing power and time; we could not afford this luxury, as we had hundreds more galaxies to run, and we shared the working environment's memory with other users.

The second run had a maximum dust fraction of  $1e-5$ , took 9 hours, 9 minutes, 44 seconds, and 1.57 GB of memory. The third run had a maximum dust fraction of  $5e-5$ , which took 7 hours, 20 minutes, 15 seconds, and 11.4 GB of memory. In the last run, the maximum dust fraction was  $1e-6$ , which took 6 hours, 39 minutes, 48 seconds, and 6.5 GB of memory to complete. This test was conducted on ten random galaxies, and the time presented changed with different galaxies. The presented times were recorded from one

---

<sup>16</sup>The IDIA supercomputer cloud memory is shared with other users, resulting in space and memory limitations

galaxy's results and were included to demonstrate how the test was done for each galaxy. An example of what the test looked like for the first three galaxies is shown in Figure 12. Figure 12 shows the percentage error plots of the fluxes obtained in each simulation run compared to the flux obtained from a super fine grid or best results simulation run. The lines show the percentage error of the simulation compared to the superfine simulation, differentiated by their maximum dust fraction in the legend. In the figures, the red line is for the maximum dust fraction of  $1e-5$ , the blue maximum dust fraction of  $5e-5$ , and the pink maximum dust fraction of  $1e-6$ . The three graphs show that the most converging simulation had a maximum dust fraction of  $1e-6$ , as its percentage error was less than 0.4% from UV to submm wavelength.

Therefore we concluded that a dust fraction of  $1e-6$  and a minimum spatial grid level of 6 to 12 would yield good results at a reasonable amount of run time, memory, and computational power. The average time of the run was 7 hours, with 7GB of memory.

### **Photon test**

The photon test has similar principles as the spatial grid convergence test. The difference is that the photon test checks for the number of photons that SKIRT can shoot and provide good results in reasonable computational power and time requirements. Generally, the higher the number of photons, the higher the simulation resolution, the larger the memory, and the longer the simulation runs. Unfortunately, this must be avoided in our working environment.

In this test, we simulated the same galaxy four times, keeping a constant maximum dust fraction of  $1e-6$  and a minimum spatial grid level of 6 to 12, as we concluded in the spatial grid test and changing the number of photons. The first run was the most expensive (superfine), its number of photons was  $1e7$ , and it took 43 hours, 36 minutes, 30 seconds, and 11.5 GB of memory to complete. In the second run, the number of photons was  $1e7$  and took 5 hours, 6 minutes, 5 seconds, and 11.5 GB of memory. In the third run, the number of photons was  $5e7$ , which took 7 hours, 22 minutes, 21 seconds, and 11.5 GB of memory. The final run had  $5e8$  photons, which took 24 hours and 11.5 GB of memory. Figure 13 shows the flux comparison done in the convergence test. A combination of the

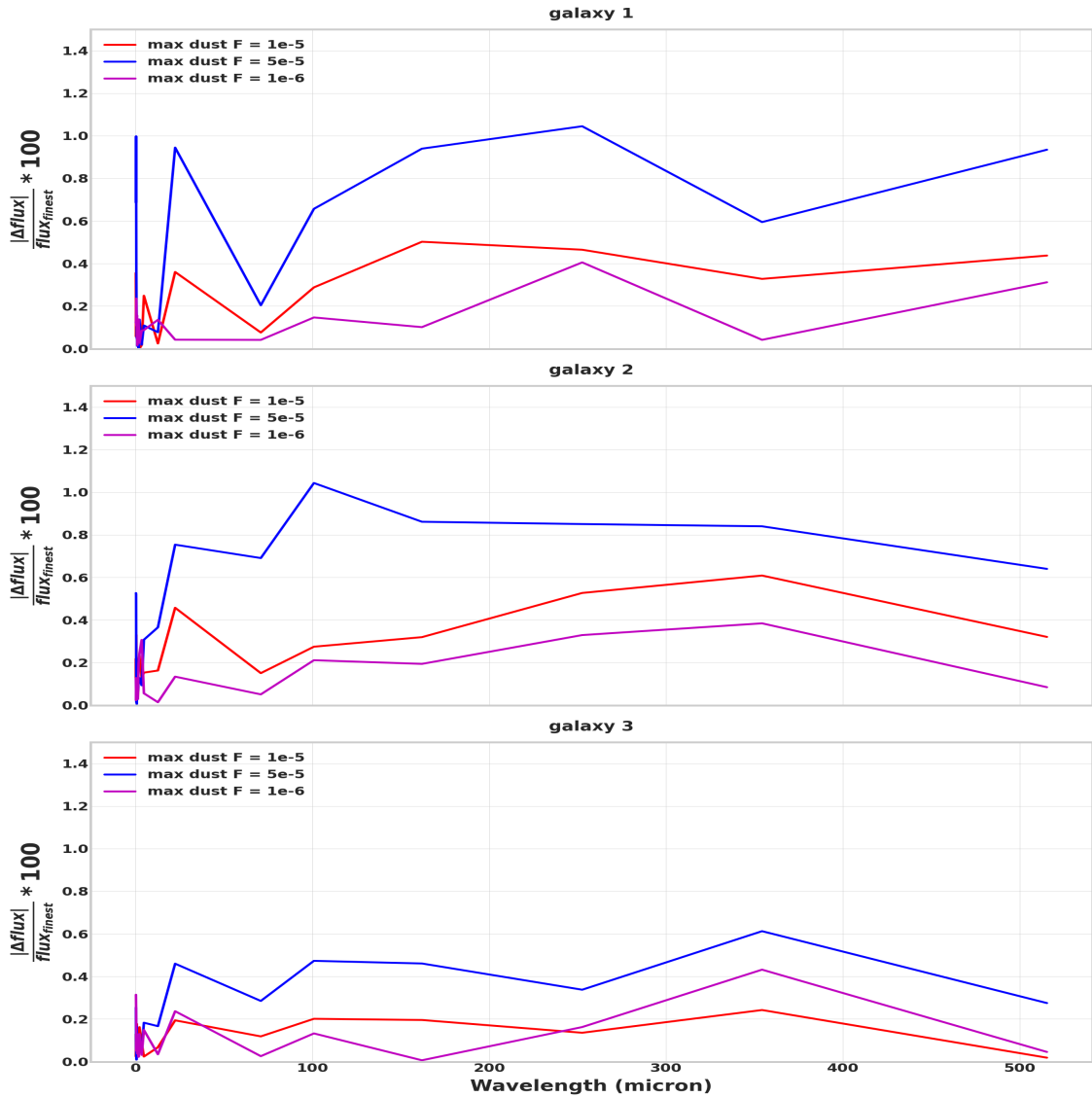


**Figure 12:** This figure shows the spatial grid convergence test; each plots depicts the different flux wavelength percentages. The percentage error in the y-axis compares the flux obtained in the superfine or best results simulation run to the flux obtained in the current maximum dust fraction simulation fluxes. The plots show the effects of changing the maximum dust fraction in each simulation for the same galaxy. The red line shows maximum dust fractions of 1e-5, the pink line shows maximum dust fractions of 1e-6, and the blue line shows maximum dust fractions of 5e-5 for the same galaxy in each plot.

number of photons 5e8, a maximum dust fraction of 1e-6, and a minimum spatial grid level of 6 to 12 were selected as suitable parameters for each simulation run. Based on the test results, 5e8 is a good value for the simulation's number of photons. On average, all our simulations ran in 24 threads in a single process, 19 to 24 hours, and 5 to 8 GB of memory.

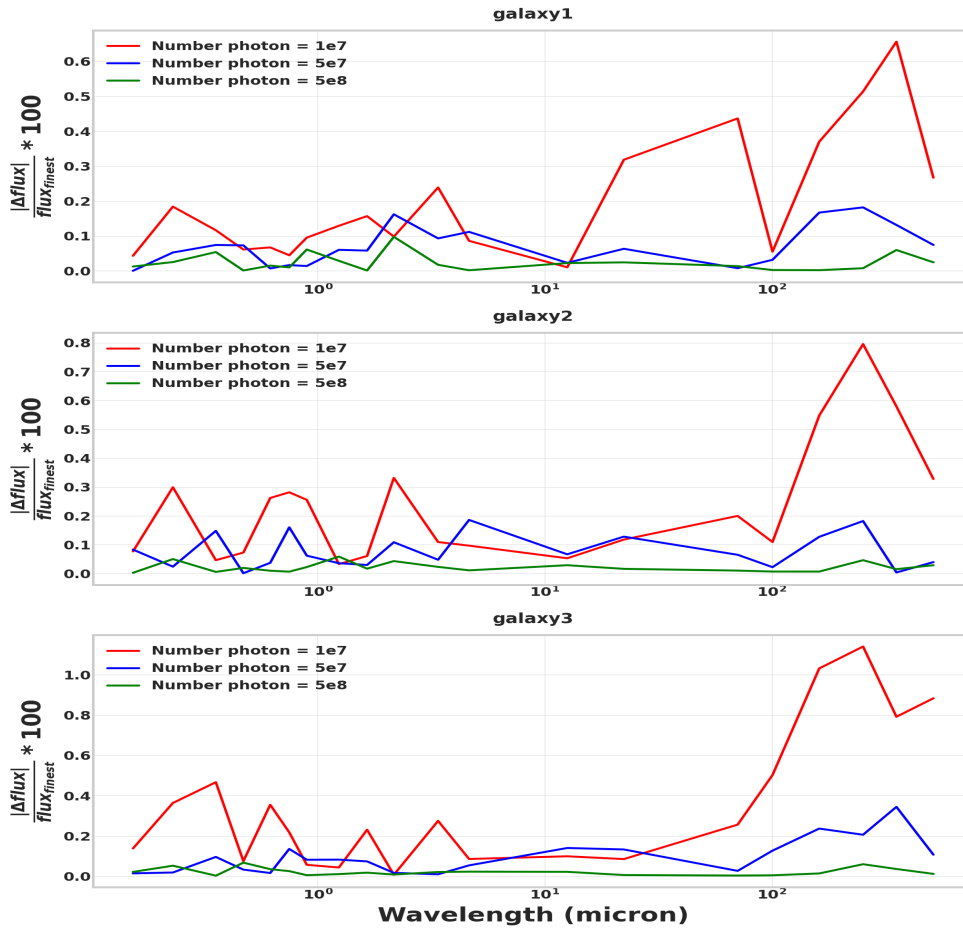


**Figure 13:** The photon test has the same procedure as the spatial grid test in Figure 12; the difference is that in this plot, we changed the number of photons shot in each simulation run. Photons = 1e7 (red line), photons = 5e7 (blue line), and photons = 5e8 (green line).

### 2.1.7 Deriving observations from SIMBA data processed with SKIRT

After the system test, all selected galaxies were simulated in the SKIRT radiative transfer code. The SKIRT SEDs output files had synthetic fluxes at different bands for each galaxy. We referred to these galaxy fluxes as mock observations, and they enabled direct comparison between simulations and observations. We used simple previous literature equations to derive the galaxies' inferred physical properties using the mock observations.

Below we present the equations used to derive the inferred physical properties in this

work. For the galaxy stellar masses, we mimicked [Camps et al. \(2016\)](#)'s procedure of determining the galaxy stellar masses using the i-band luminosity ( $L_i$ ) and g - i colour through equation 15, where  $a = -0.963$  and  $b = 1.032$ . For the galaxies' dust masses, we mimicked [Cortese et al. \(2012\)](#)'s recipes of estimating the dust masses using the SPIRE fluxes' only relation shown in Equation 16, wherein  $\log(M_{dust}/(f_{350} * D))$  is calculated using the flux density ratio Table B1 in [Cortese et al. \(2012\)](#), D is the distance from the galaxy in Mpc, and  $f_{350}$  is the flux at 350 microns in jansky. Lastly, we derived the galaxies' SFRs mimicking [Galametz et al. \(2013\)](#)'s total IR luminosity relations shown in equation 17 and equation 18, where  $L_{TIR}$  is the total IR luminosity calculated as in equation 18. When all derivations were completed, we tested and found agreement between our flux-derived physical properties and physical properties from the snapshot shown in Figure 14. In Figure 14, the x-axis is this work's derived values, and the corresponding snapshot values are in the y-axis.

$$\log_{10} \frac{M_*}{M_{\odot}} = \log_{10} \frac{L_i}{L_{i,\odot}} + a + b + (g - i) \quad (15)$$

$$\log\left(\frac{M_{dust}}{M_{\odot}}\right) = \log\left(\frac{M_{dust}}{f_{350}D^2}\right) + 2\log\left(\frac{D}{\text{Mpc}}\right) + \log\left(\frac{f_{350}}{\text{jy}}\right) - 11.32 \quad (16)$$

$$\text{SFR}(M_{\odot}/\text{yr}^{-1}) = 2.8x10^{-44}L_{TIR}(\text{erg/s}) \quad (17)$$

$$L_{TIR} = 2.023L_{24} + 0.523L_{70} + 0.390L_{100} + 0.577L_{160} + 0.721L_{250} \quad (18)$$

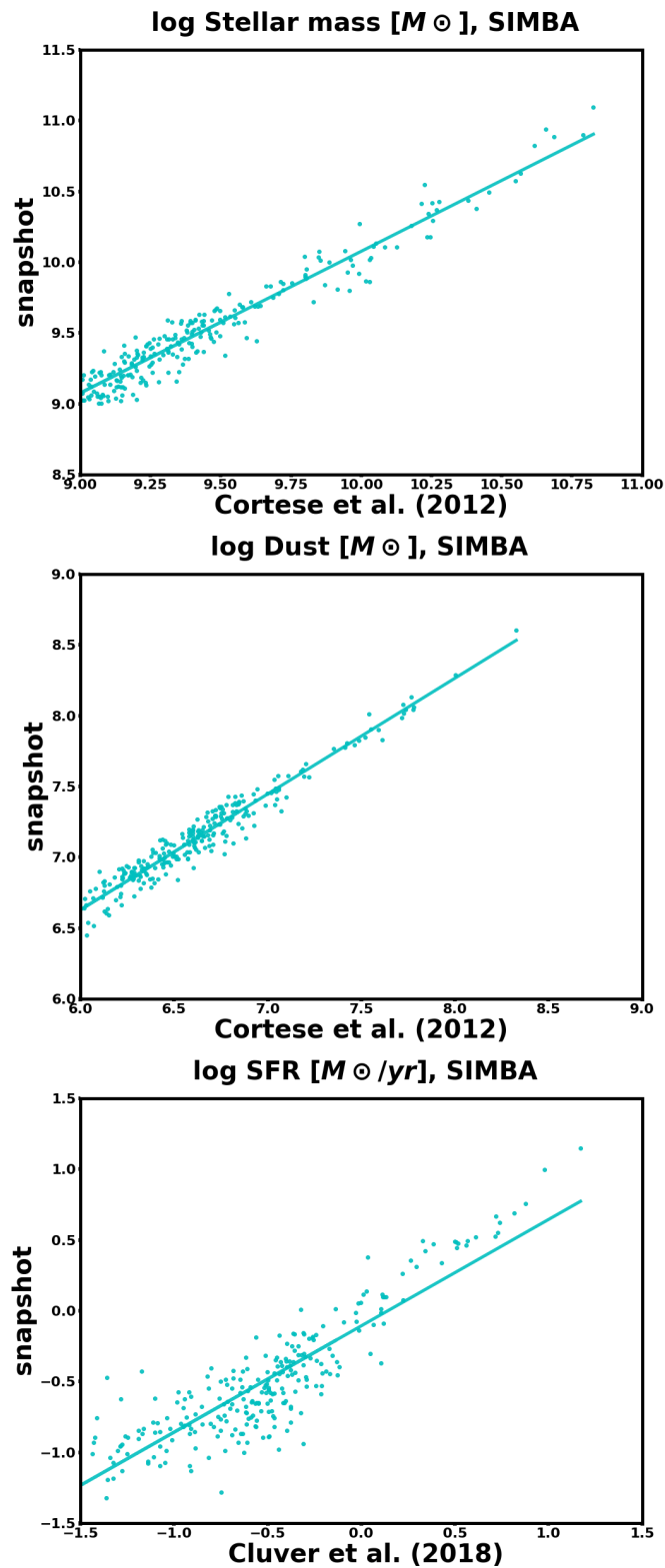


**Figure 14:** The relationship between this work’s SIMBA-derived physical properties and physical properties from the raw SIMBA snapshot. The x-axis label refers to the paper in which the flux equation used to derive the physical property was taken, and the y-axis refers to snapshot properties.

## 2.2 Methodology for dealing with EAGLE data

The EAGLE data presented in this work was already post-processed and SKIRT simulated in [Camps et al. \(2016\)](#). In the following sections, we discuss the EAGLE-selected galaxies as we applied the same selection criteria in all three datasets. And we also discuss the differences and similarities made when [Camps et al. \(2016\)](#) was processing the EAGLE galaxies, compared to how this project processed the SIMBA galaxies, as this helped us understand some of the differences seen in the results of the scaling relation when comparing the simulations against each other. Figure 15 show the physical properties and distribution for all the galaxies in the used EAGLE ( $z=0$ ) dataset before applying the selection criteria.

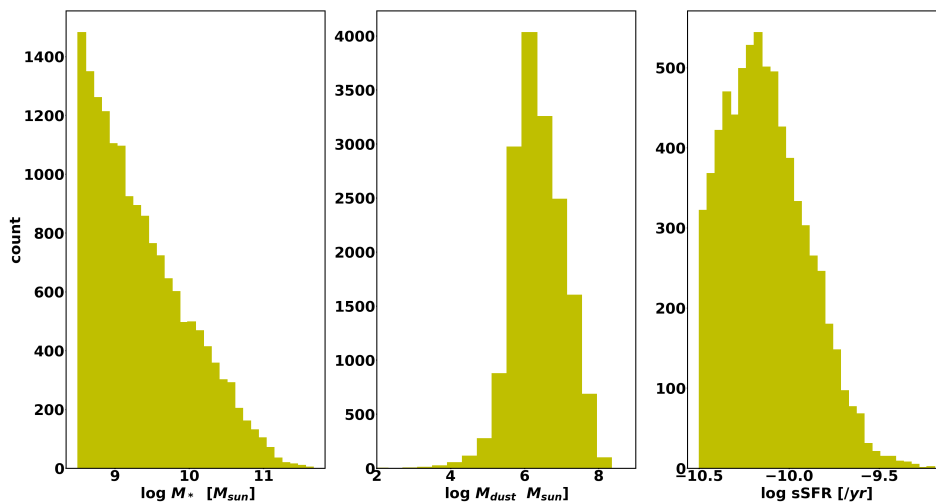


**Figure 15:** This figure presents the physical properties and distribution for EAGLE galaxies.

### 2.2.1 Selection criteria for the EAGLE data

The EAGLE sample had 16 493 galaxies, and we applied the same selection criteria used in SIMBA galaxies to ensure that we studied or compared similar samples. After applying the selection criteria, we retained 7227 EAGLE galaxies. The EAGLE sample was still a huge sample of galaxies compared to SIMBA, with 264 galaxies. As a result, we randomly picked 1000 galaxies from the selected 7227 EAGLE galaxies. We used the box and whisker diagram to see the stellar mass, dust mass, and sSFR distribution of the selected 1000 EAGLE galaxies, shown in Figure 16 from top to bottom.

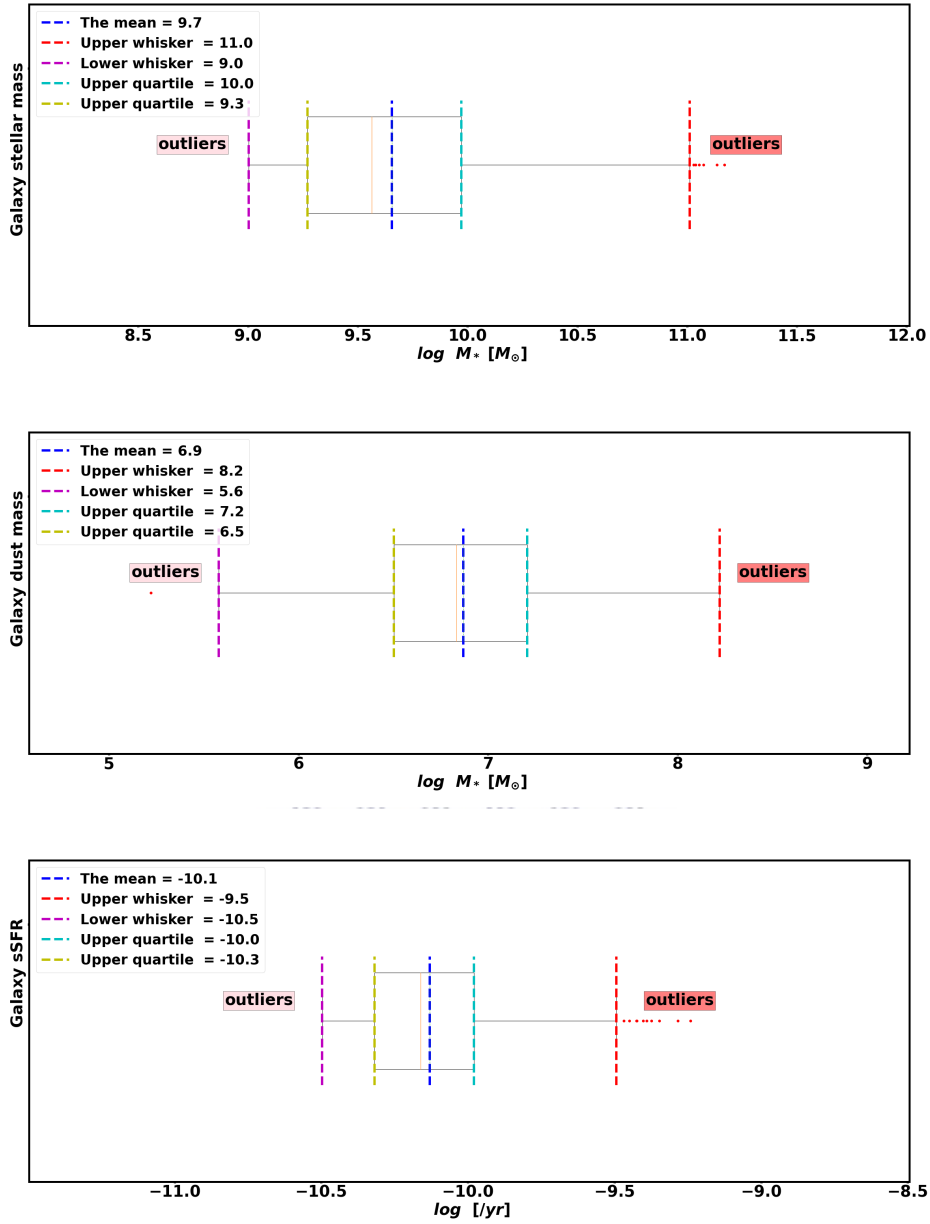


**Figure 16:** The EAGLE galaxies box and whisker physical properties distribution diagram.

The top panel of Figure 16 is the EAGLE galaxies stellar masses box distribution. It starts from a minimum stellar mass of  $10^{9.0}M_{\odot}$  to a maximum of  $10^{11.2}M_{\odot}$ , with an average and median of  $10^{9.7}M_{\odot}$  and  $10^{9.7}M_{\odot}$ , respectively. A majority 499 (50%) of the galaxies lie between  $10^{9.3}M_{\odot} \leq M_* \leq 10^{10.0}M_{\odot}$ , 248 (25%) galaxies range between  $10^{9.0}M_{\odot} < M_* \leq 10^{9.3}M_{\odot}$ , 245 (24%) are higher stellar mass galaxies ranging between  $10^{10.0}M_{\odot} < M_* \leq 10^{11.0}M_{\odot}$ , and 1% (6) outlier massive galaxies ( $M_* > 10^{11.0}M_{\odot}$ )

The middle panel of Figure 16 is the EAGLE galaxies' dust mass box distribution. It starts from a minimum of  $10^{5.2}M_{\odot}$  to a maximum of  $10^{8.2}M_{\odot}$ , with an average and median of  $10^{6.9}M_{\odot}$  and  $10^{6.8}M_{\odot}$ , respectively. Majority 500 (50%) of the galaxies range between  $10^{6.9}M_{\odot} < M_{dust} \leq 10^{7.2}M_{\odot}$ , 250 (25%) range between  $10^{5.6}M_{\odot} < M_{dust} \leq 10^{6.5}M_{\odot}$ , and 250 (25%) range between  $10^{7.2}M_{\odot} < M_{dust} \leq 10^{8.2}M_{\odot}$ .

At the bottom panel of Figure 16 is the EAGLE galaxies' sSFR box distribution. It starts from a minimum of  $10^{-10.5}yr^{-1}$  to a maximum of  $10^{-9.2}yr^{-1}$  with an average and median of  $10^{-10.1}yr^{-1}$  and  $10^{-10.1}yr^{-1}$ , respectively. Mostly 500 (50%) of the galaxies range between  $10^{-10.3} < sSFR[yr^{-1}] \leq 10^{-10.9}$ , 249 (25% ) galaxies are lower sSFR galaxies ranging between  $10^{-10.5} < sSFR[yr^{-1}] \leq 10^{-10.3}$ , and 239 ( 24% ) are higher sSFR galaxies in the range of  $10^{-10.0} < sSFR[yr^{-1}] \leq 10^{-10.0}$ . The EAGLE galaxies' sSFR distribution has an outlier rate of 1% (11) with an sSFR above  $10^{-10.0}yr^{-1}$ .

### 2.2.2 Post-processing procedure of EAGLE data compared to that of SIMBA data

As highlighted earlier, the EAGLE post-processing procedure was not done in this work, it was done by Camps et al. (2016), and we used it for comparison. This section highlights mainly the difference between the EAGLE post-processing procedure and the SIMBA post-processing procedure.

Similar to SIMBA, EAGLE galaxies are identified as gravitationally bound structures in a halo of dark baryonic matter. Their galaxy extraction process has similarities and differences. The extracted galaxies have a fixed radius of 30 kpc for both EAGLE and SIMBA. One of the outstanding attributes of the SIMBA recipe is its ability to derive dust during the simulation (see section 1.4). The EAGLE simulation does not include the derivation of dust particles by itself; however, the EAGLE post-processing procedure does. EAGLE galaxies' dust mass is derived using the gas particles, where a dust-to-mass ratio of  $f_{dust} = 0.3$  is assumed, and the dust distribution from each cold gas particle<sup>17</sup> is calculated using equation 19:

<sup>17</sup>A non-zero SFR and maximum temperature less than 8000 K

$$m_{dust} = \begin{cases} f_{dust} Z M, & \text{if } T < T_{max} \text{ or } SFR > 0 \\ 0, & \text{other} \end{cases} \quad (19)$$

where  $Z$  is the metallicity,  $M$  is the current mass, and  $T$  is the particle's current temperature (Camps et al., 2016)

In SIMBA, the star-forming region particles are all younger than  $10Myrs$  stellar particles (Section 2.1.3). In EAGLE, the star-forming region particles are sampled as stellar particles less than  $10Myrs$ , and all star-forming gas particles.

### 2.2.3 Deriving observations from EAGLE data processed with SKIRT

The process of computing physical properties for EAGLE galaxies is detailed in Camps et al. (2016), and Trčka et al. (2020). This section compares our inferred physical properties recipes with those used in Camps et al. (2016). The EAGLE data catalogue already had the inferred physical observation; however, it was derived or calculated using different recipes. To test the difference between the recipes used in this work and those used in EAGLE, we derived the EAGLE physical properties using the simple equations used in this project on SIMBA data (see Section 2.1.7). Figure 17 presents the outcome, showing agreement between the two methods used.

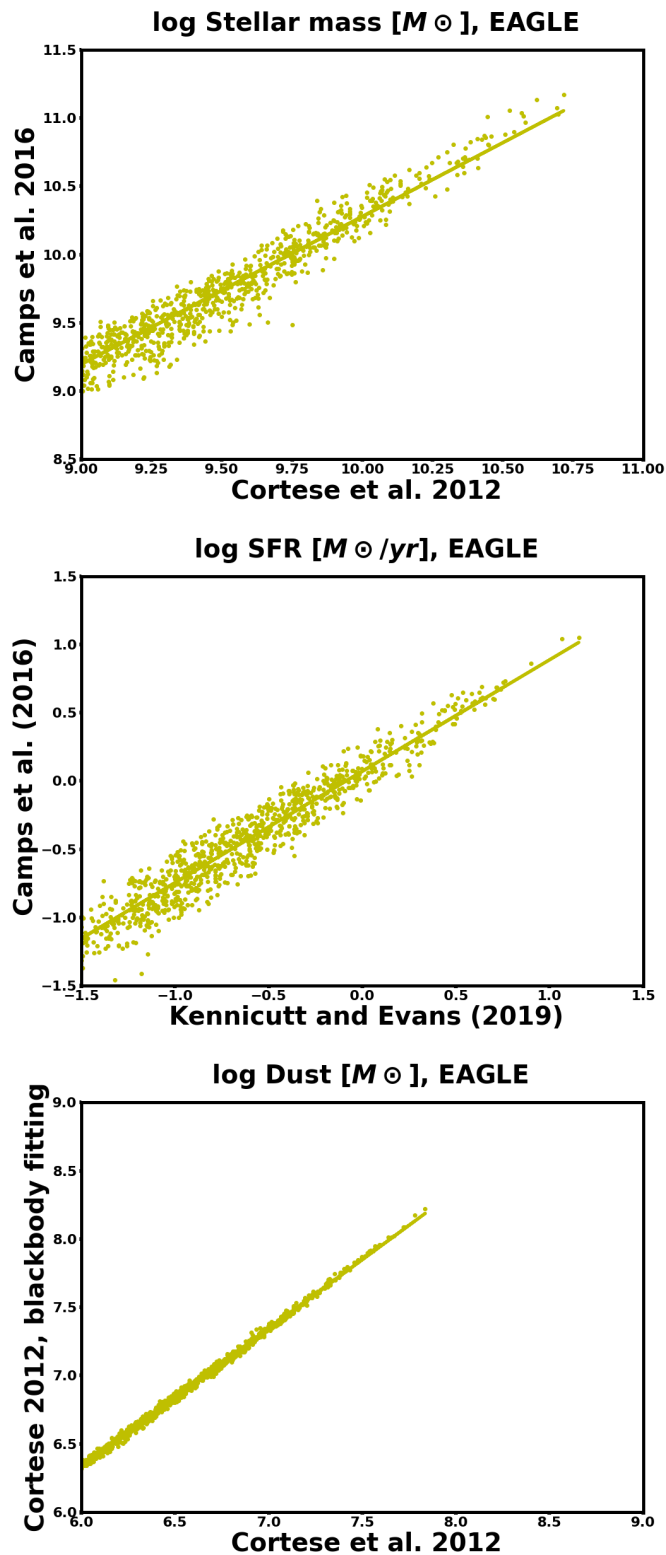


**Figure 17:** The relationship between EAGLE galaxies' physical properties derived in this work using simple flux recipes on the y-axis and EAGLE galaxies' physical properties from the employed [Camps et al. \(2016\)](#) catalogue in the x-axis.

## 2.3 Methodology for dealing with DustPedia data

DustPedia is observational data that we used to compare the simulated galaxies with real observed galaxies in this project. The presented dataset was taken from Trčka et al. (2020), and Figure 19 shows the dataset galaxies' physical properties distribution before we applied the selection criteria.

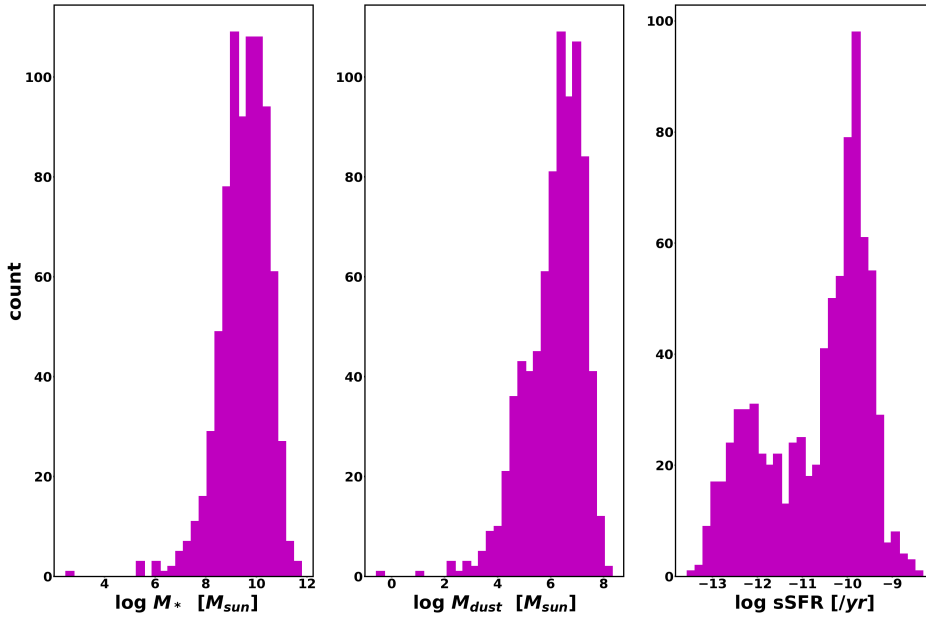


**Figure 18:** Similar to Figure 8 and Figure 15 this is the physical properties galaxy distribution for all the galaxies in the studied DustPedia database.

### 2.3.1 Selection criteria for DustPedia data

The same selection criteria used throughout this research (see Section 2.1.1) are used here. The full DustPedia sample contains 814 galaxies that cover the range of stellar mass  $10^2 M_{\odot} \leq M_* \leq 10^{11.8} M_{\odot}$ , dust mass range of  $10^{-1} M_{\odot} \leq M_{dust} \leq 10^{8.4} M_{\odot}$ , and specific star-formation rates range of  $10^{-14} yr^{-1} \leq sSFR \leq 10^{-9.5} yr^{-1}$ , as seen in Figure 18. After applying the selection criteria, we were left with 302 DustPedia galaxies for this analysis.

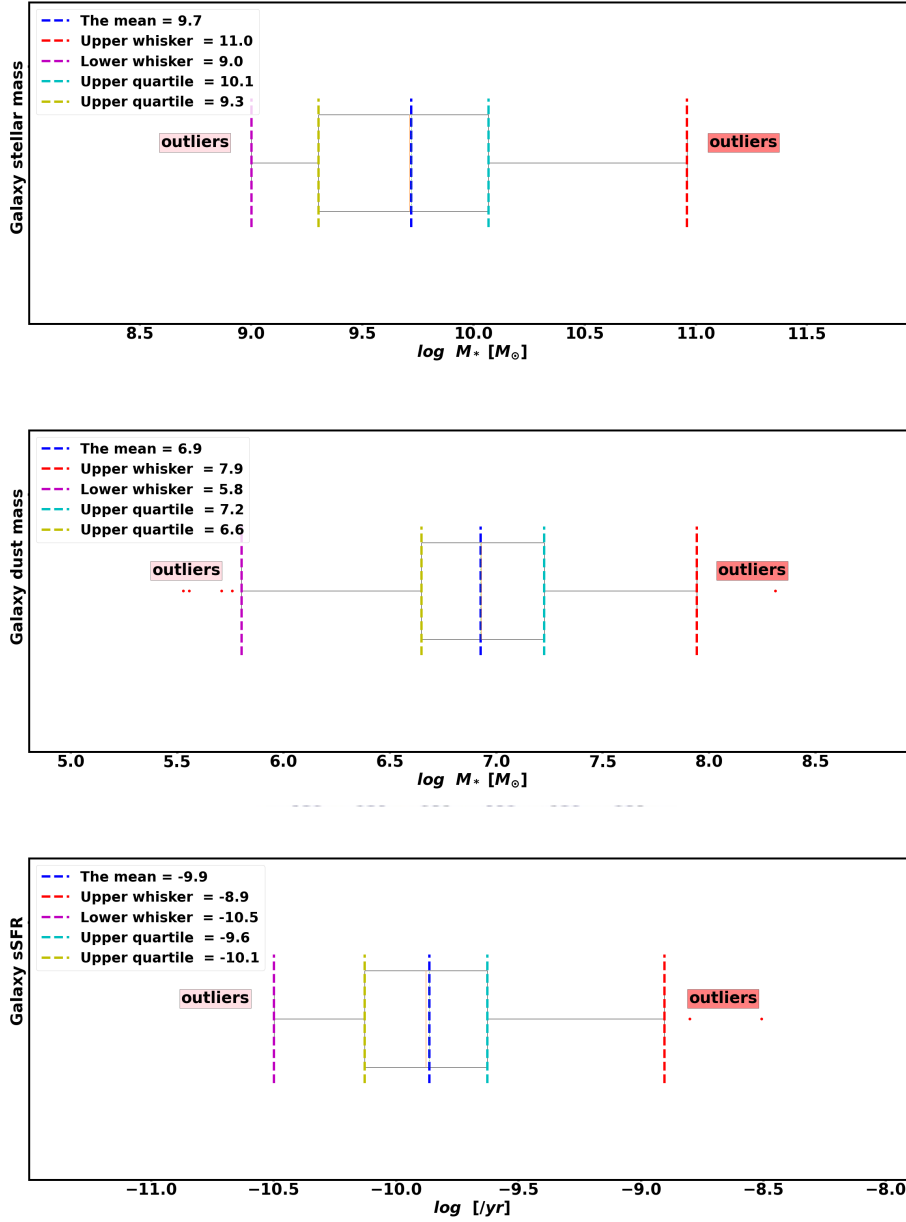


**Figure 19:** The stellar mass, dust mass, and specific star-formation box and whisker statistics diagram for all the selected from the DustPedia database

The galaxies' stellar masses box distribution in the top panel of Figure 19 starts from a minimum stellar mass of  $10^{9.0}M_\odot$  to a maximum of  $10^{11.0}M_\odot$ , with an average and median of  $10^{9.7}M_\odot$  and  $10^{9.7}M_\odot$  respectively. Majority, 50% (150) of the galaxies lie between  $10^{9.3}M_\odot \leq M_* \leq 10^{10.1}M_\odot$ , 25% (76) range between  $10^{9.0}M_\odot < M_* \leq 10^{9.3}M_\odot$ , and 25% (76) are higher stellar mass galaxies ranging between  $10^{10.1}M_\odot < M_* \leq 10^{11.0}M_\odot$ .

The dust mass distribution in the middle panel of Figure 19 starts from a minimum of  $10^{5.5}M_{\odot}$  to a maximum of  $10^{8.3}M_{\odot}$ , with an average and median of  $10^{6.9}M_{\odot}$  and  $10^{6.9}M_{\odot}$ , respectively. Most of the galaxies 50% (150) range between  $10^{6.6}M_{\odot} < M_{dust} \leq 10^{7.2}M_{\odot}$ , 25% (76) range between  $10^{5.8}M_{\odot} < M_{dust} \leq 10^{6.6}M_{\odot}$ , and 24% (75) range between  $10^{7.2}M_{\odot} < M_{dust} \leq 10^{7.9}M_{\odot}$ . The distribution has outliers both in the lower and higher ends. There are four galaxies with dust mass lower than  $10^{5.8}M_{\odot}$  and one galaxy above  $10^{7.9}M_{\odot}$ .

Lastly the sSFR distribution in the bottom panel of Figure 19 starts from a minimum of  $10^{-10.5}yr^{-1}$  to a maximum of  $10^{-8.5}yr^{-1}$  with an average and median of  $10^{-9.9}yr^{-1}$  and  $10^{-9.9}yr^{-1}$ , respectively. Most galaxies 50% (150) range between  $10^{-10.1} < sSFR[yr^{-1}] \leq 10^{-9.6}$  25% (76) are lower sSFR galaxies ranging between  $10^{-10.5} < sSFR[yr^{-1}] \leq 10^{-10.1}$ , and 24.3% (74) are higher sSFR galaxies in the range of  $10^{-9.6} < sSFR[yr^{-1}] \leq 10^{-8.9}$ , with a 0.7% (2) outlier with a sSFR above  $10^{-8.9}yr^{-1}$ .

### 2.3.2 Deriving DustPedia observation's physical properties using the observational fluxes

Observations detect the fluxes from the sources and not the physical properties of the sources, galaxies in our case. Different observations use different methods to get the physical properties of observations, i.e. the galaxy's stellar mass. For the DustPedia dataset presented in this project, the observation's physical properties were estimated using the Code Investigating GALaxy Emission (CIGALE) modelling method, which is a SED fitting method (Davies et al., 2017). In this project for SIMBA galaxies, we did not use SED fitting but simple recipes that depend on mock fluxes only. To test the difference between the recipes used in this work (flux only simple recipes) and those used in DustPedia (SED fitting), we estimated the DustPedia physical properties using the recipes used in this work (applying observational fluxes on the simple equations). We compared our results with the physical properties in the original dataset, as shown in Figure 20. Figure 20 shows an agreement in the recipes but with some offsets, mainly in the dust estimation.

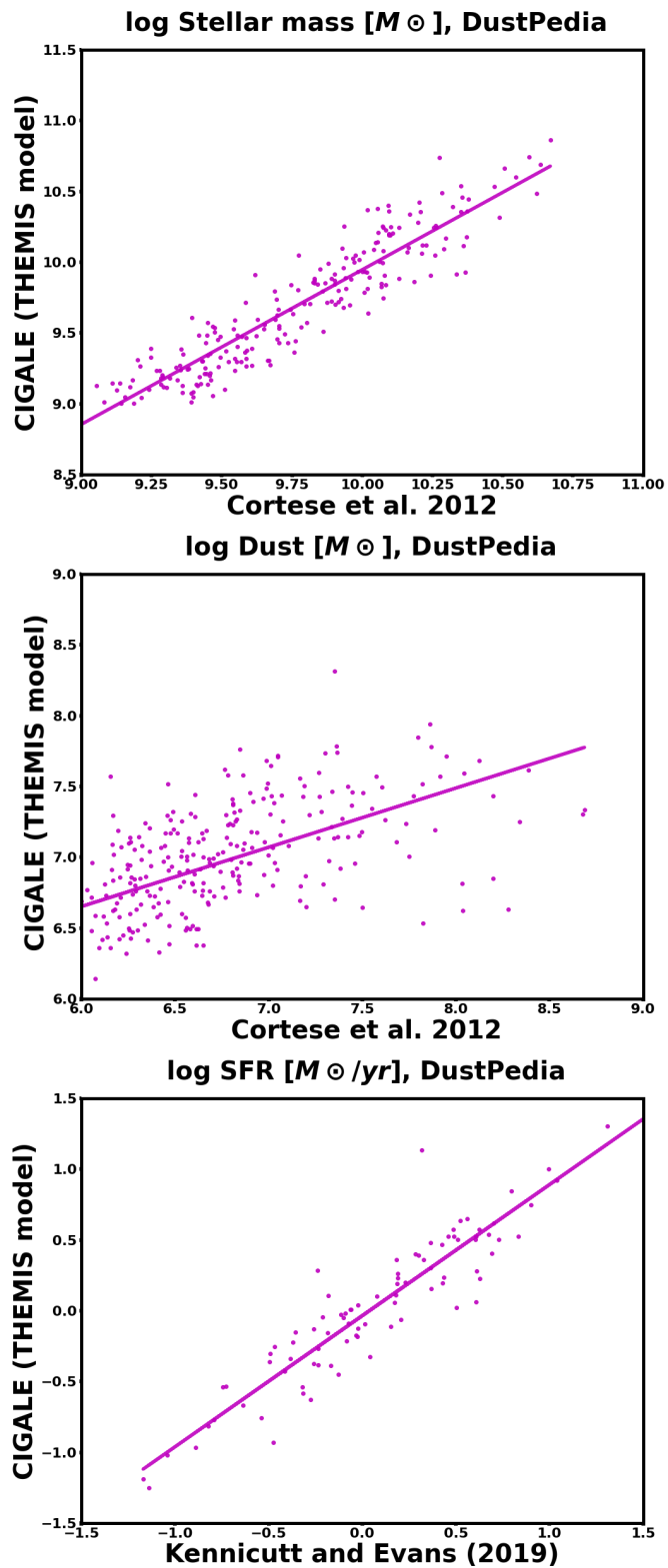


**Figure 20:** The relationship between this work’s DustPedia-derived physical properties and properties derived from [Clark et al. \(2018\)](#).

## 2.4 Statistics test on selected galaxies datasets

After selecting the galaxies from all three datasets, we conducted a few statistical tests to see if our datasets had significant differences. We tried the T-test ([Mishra et al., 2019](#)), Welch's test ([Keselman et al., 2004](#)), ANOVA test ([Kim, 2014](#)), and the Kruskal-Wallis H-test. Due to the different assumptions used in each test, we found Welch's and Kruskal-Wallis H-tests best for our datasets ([MacFarland & Yates, 2016](#)).

### The Kruskal-Wallis H-test

The Kruskal-Wallis H-test tests the population median for two or more groups, even if they are different in size, and returns the statistics and p-value. If the p-value is less than 0.05, then there is a significant difference between the datasets. If the p-value is more than 0.05, then there is no significant difference in the dataset. We tested the dust mass, stellar mass, and sSFR statistics distribution, and the test showed a significant difference in our datasets. For more information on this test, see [MacFarland & Yates \(2016\)](#).

### The Welch's test

The Kruskal-Wallis P-value test shows whether there is a significant difference in the three datasets, but it does not show which set is different. So we also did Welch's test; this test tests the difference in the population's mean, assuming they have different variances. The Kruskal-Wallis p-value test shows us whether there is a significant difference in the three datasets, but it does not show which set is different. Therefore, we also performed Welch's test. This test returns the value of the statistics and the p-value. Using similar p-value reasoning as in the Kruskal-Wallis test, we found no significant difference between EAGLE and DustPedia; however, all other paired distributions had significant differences. For more information on this test, see [Keselman et al. \(2004\)](#).

## 2.5 Method limitations and conclusions

Significant differences in sample quantity exist in our studied datasets. EAGLE has more galaxies compared to SIMBA and DustPedia. In the future, we can include all the different snapshot volumes, resulting in a larger sample and a broader insight into the study. Table 5 below summarises each parent dataset's primary information.

<b>SIMBA DATA</b>					
Box name	box length (cMpc)	Aperture ((kpc)	Distance (Mpc)	Nbands	No. of galaxies
m25n1024	25	30	20	20	2411
Extracted galaxies	25	30	20	20	264
<b>EAGLE DATA</b>					
Box name	box length (cMpc)	Aperture ((kpc)	Distance (Mpc)	Nbands	No. of galaxies
Ref-L1001504	100	30	20	29	16493
Extracted galaxies	100	30	20	29	1000
<b>DustPedia DATA</b>					
Aperture ((kpc)	Distance (Mpc)	No. of bands	No. of galaxies		
<17.6>	<21.5>	<20>	814		
<17.6>	<21.5>	<20>	302		

**Table 5:** The galaxy information for each dataset. For the simulations, the first column is the dataset name, as in simulations. The second column is the snapshot box size in comoving units. The third column is the aperture radius from the galaxy centre. The fourth column is the assumed distance (Mpc) from the observer/detector. The fifth column is the number of available band lists. The last column is the number of galaxies in each dataset. For DustPedia, the average galaxy aperture is in the first column, the distance from the galaxy in the second column, the number of available band lists in the fourth column, and the number of galaxies in the last column.

Above limitations, our methodology has met the objectives. We managed to get the galaxies of interest and create their mock observations with the SKIRT code, enabling scaling relations presented in the following chapter.

### 3 Results and Discussion

This chapter presents and discusses the main results of this project. Section 3.1 presents the inferred physical properties. Section 3.2 discusses the common luminosity proxies and compares them with previous literature. Section 3.3 presents the FIR and MIR luminosities scaling relations. Finally Section 3.4 presents the dust-to-stellar mass ratio's scaling relations.

#### 3.1 Inferred physical properties

The aims of this project are to evaluate the scaling relations of the cosmologically simulated galaxies and compare them with the scaling relations of real galaxies. This section compares the stellar mass, dust mass and specific star-formation rate (sSFR) of the galaxies from the SIMBA and EAGLE cosmological simulations and the DustPedia observational dataset.

The stellar mass distribution of the three data sets ranged from  $10^9 M_{\odot}$  to  $10^{11.2} M_{\odot}$ . EAGLE and DustPedia had a similar distribution, as found in Welch's test (Section 2.4) and demonstrated in the left panel of Figure 21. The SIMBA sample is dominated by lower mass galaxies in the range  $\leq 10^{9.5} M_{\odot}$ . All the samples contain a few higher mass galaxies that are greater than  $10^{10.5} M_{\odot}$ , but no sample contains a galaxy with a stellar mass higher than  $10^{11.2} M_{\odot}$ . The samples lack higher mass galaxies because the selection criteria promoted younger, more prominent stellar populations and excluded massive galaxies, which are usually red and old stellar populations with suppressed SFR. SIMBA galaxies have higher dust masses than EAGLE and DustPedia galaxies, as shown in Figure 21 (middle panel). The difference in the dust mass estimation mainly exists in the lower dust mass galaxies. The difference in the calculated relative change in the lower dust mass range was on average  $\approx 10\%$  between SIMBA and the other two samples, meaning SIMBA lower mass galaxies had an average of 10% more galaxy dust mass than EAGLE and DustPedia galaxies.

Between the three samples, EAGLE galaxies have the lowest sSFR. As seen in Figure 21 (right panel), the distributions are horizontally centered within a range of  $10^{-10.5} < \text{sSFR}$

$[\text{yr}] < 10^{-9.7}$  and the EAGLE distribution is shifted towards the lower sSFR range. DustPedia has significantly higher sSFR galaxies, i.e. the sample has high sSFR galaxies ( $sSFR > 10^{-9.5} \text{yr}^{-1}$ ) that are not contained in the SIMBA and EAGLE samples. The DustPedia distribution ranges between  $10^{-10.5} < \text{sSFR} [\text{yr}] < 10^{-9.5}$ .

These results gave us an insight into the dataset's physical properties that we should keep in mind as we continued with our analysis. For example, SIMBA galaxies have higher galaxy dust masses, and DustPedia galaxies have high sSFR. The following section examines whether these physical properties well represent their common known proxies.



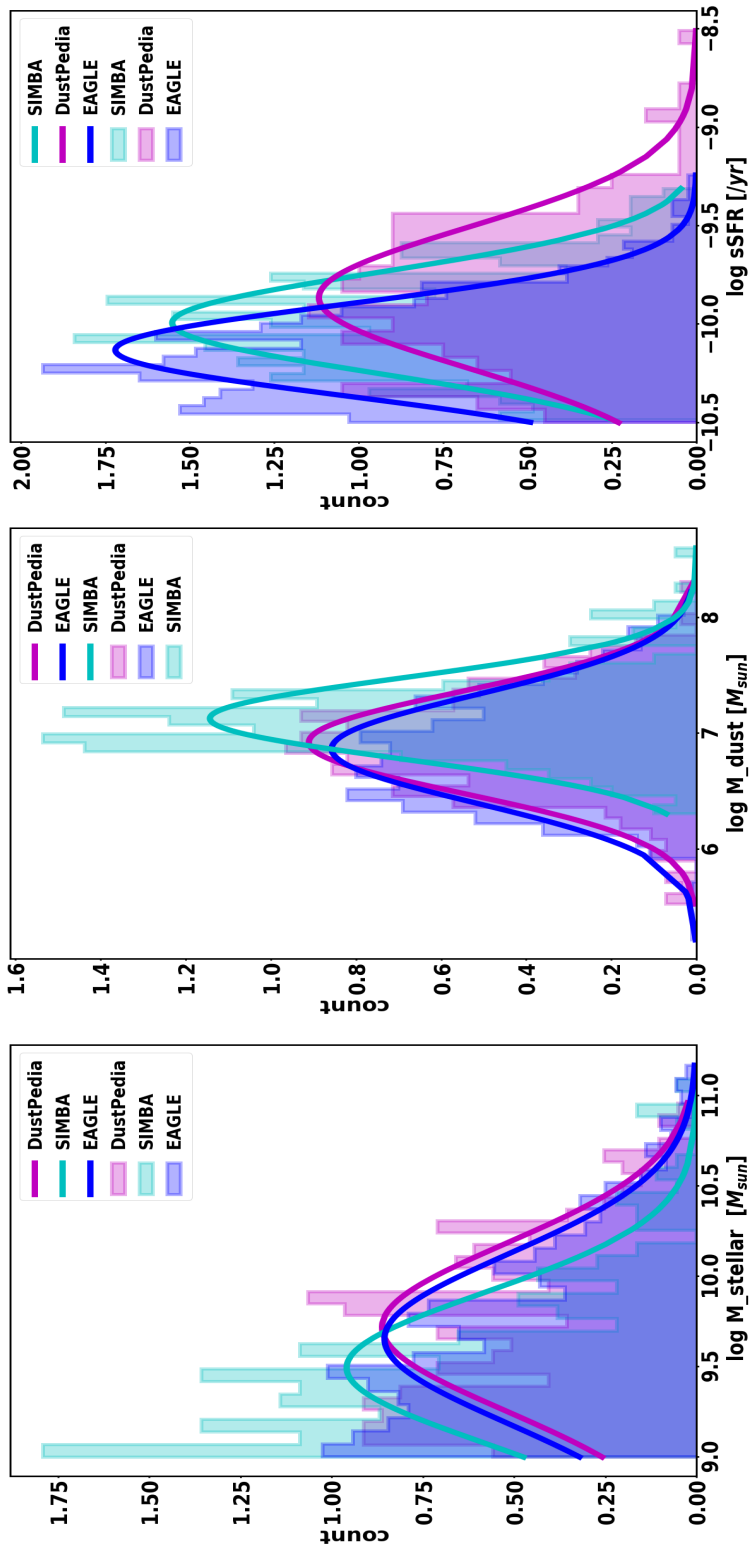


**Figure 21:** The normalised distribution of the galaxies' physical properties for SIMBA (cyan), EAGLE (blue), and DustPedia (magenta) data. The figure shows the stellar mass, dust mass, and sSFR distribution from left to right.

Sample galaxy stellar masses										
Dataset	Count	min.	max.	$\bar{x}$	Median	Mode	Var	std	skew	
<b>SIMBA</b>	264	9.001	11.094	9.495	9.407	9.339	0.173	0.415	1.322	
<b>DustPedia</b>	302	9.00	10.961	9.711	9.719	9.135	0.213	0.462	0.352	
<b>EAGLE</b>	1000	9.00	11.169	9.655	9.563	9.092	0.217	0.466	0.700	
Sample galaxy dust mass										
<b>SIMBA</b>	264	6.308	8.602	7.131	7.099	7.394	0.121	0.348	0.888	
<b>DustPedia</b>	302	5.529	8.312	6.925	6.927	5.708	0.191	0.437	-0.213	
<b>EAGLE</b>	1000	5.220	8.221	6.868	6.833	6.045	0.216	0.465	0.269	
Sample galaxy sSFR										
<b>SIMBA</b>	264	-	-9.311	-9.992	-	-9.498	0.066	0.257	0.258	
		10.484			10.002					
<b>DustPedia</b>	302	-	-8.508	-9.865	-9.878	-9.949	0.127	0.356	0.401	
		10.499								
<b>EAGLE</b>	1000	-	-9.242	-	-	-	0.054	0.231	0.636	
		10.497		10.130	10.162	10.203				

**Table 6:** The statistical summary of the physical properties for each sample's stellar masses in  $M_{\odot}$ , dust masses in  $M_{\odot}$ , and the sSFRs in ( $yr^{-1}$ ). The table shows each sample's minimum value (min), maximum value (max), average ( $\bar{x}$ ), median, mode, variance (Var), standard deviation (std), and the sample distribution's skewness (skew) from left to right.

## 3.2 Luminosities as a proxy of stellar mass, dust mass, and star formation rate

This section examines the simulation's SKIRT fluxes' ability to reproduce known common proxies by plotting their mock luminosities versus their inferred physical properties on the same axis with real observational galaxies (see Figure 22). The presented simulation's luminosities and physical properties were calculated using the SKIRT output fluxes. The physical properties studied here are the galaxies' stellar mass, dust mass, and SFR. The corresponding luminosity bands are the WISE  $3.4\mu m$ , WISE  $22\mu m$ , and SPIRE  $250\mu m$  bands. In previous literature, the WISE  $3.4\mu m$  band luminosities are described to be excellent galaxy stellar mass tracers Trčka et al. (2020), the WISE 12 and  $22\mu m$  monochromatic luminosities are good galaxies SFR tracers (Lee et al., 2013; Trčka et al., 2020), and the submillimetre SPIRE  $250\mu m$  band fluxes are good galaxy dust masses estimators (Dunne et al., 2011; Trčka et al., 2020). To check if our samples agree with the common known proxy relations (see Figure 22), we replicated these relations with our data samples, and we also included the lines of best fit traced from the previous literature. These proxies are important to confirm, as we used them in Section 3.3 to interpret the MIR/FIR luminosities scaling relations physically. To compare SIMBA's and EAGLE's SKIRT output fluxes in reproducing observational fluxes, we repeated the same band relation separately for simulation and observation. An overview of the results ends the section, which includes the derivation of general equations that can be used to estimate the galaxies' physical properties, provided that one has access to the fluxes ( see Section 3.2.4).

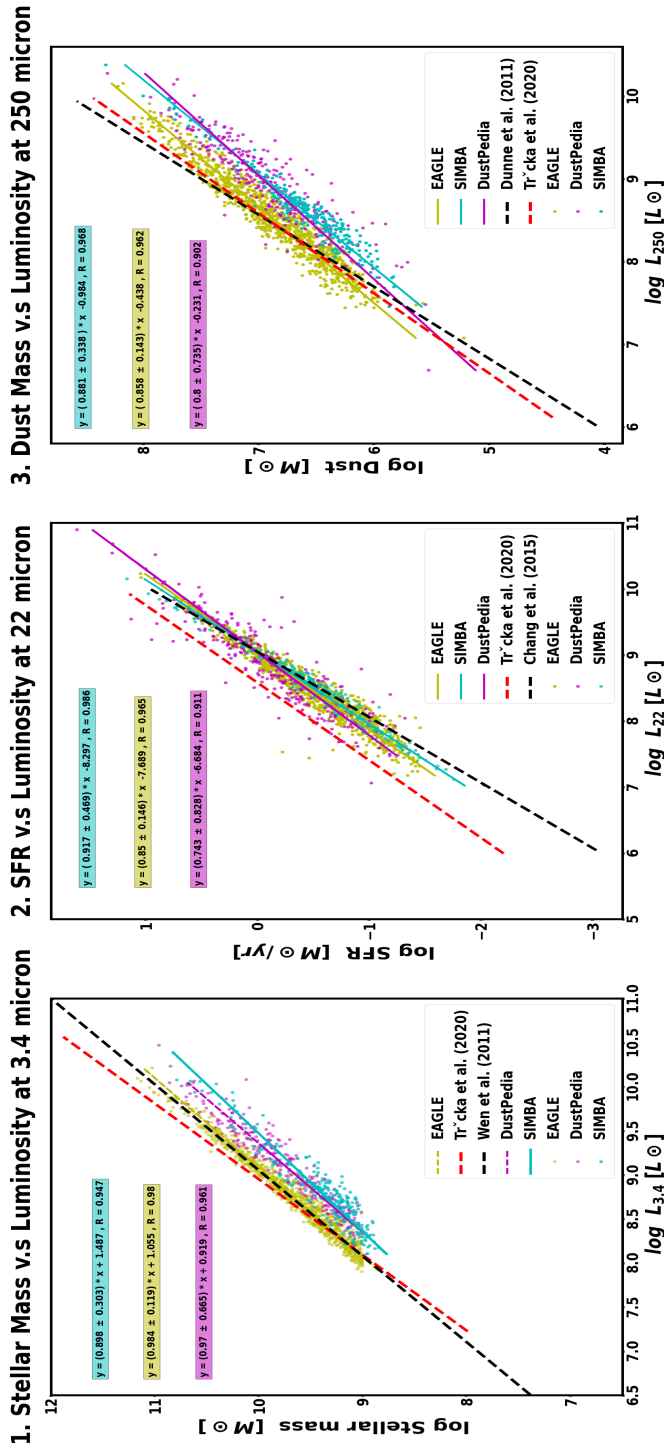


**Figure 22:** The relationship between the galaxies' luminosities and their stellar mass, dust mass, and SFR. The dots represent the SIMBA (cyan), EAGLE (green), and DustPedia (magenta) galaxies. The best fit line of each dataset is shown in the same colour code as the dots in each plot. The dashed red and black lines are the line of best fits traced from similar relations in previous literature for comparison. In the top row, the red dashed lines represent Trčka et al. (2020)'s relations, and the black dashed lines from left to right represent Wen et al. (2013), Chang et al. (2015), and Dunne et al. (2011) relations, respectively.

### 3.2.1 The WISE $3.4\mu\text{m}$ luminosity as the galaxy stellar mass proxy

Figure 23 shows the stellar mass tracer relation between the SIMBA and DustPedia galaxies in the left panel and between the EAGLE and DustPedia galaxies in the right panel. This relationship shows that SIMBA galaxies' SKIRT estimated fluxes agree better with observations than EAGLE galaxies' SKIRT estimated fluxes. So when coupling SIMBA and SKIRT, the SIMBA simulation reproduces the stellar masses of real galaxies. As for the differences observed between the EAGLE and DustPedia galaxies relations (right panel), there are two possible explanations. First, the SKIRT simulations of EAGLE galaxies at fixed galaxy stellar masses may have underestimated the galaxies'  $3.4\mu\text{m}$  fluxes (EAGLE galaxies' luminosities are 0.94 dex lower than DustPedia galaxies at fixed galaxy stellar masses). Second, the EAGLE galaxies may have higher galaxy stellar masses at fixed  $L_{3.4\mu\text{m}}$ , and we discuss these possibilities below.

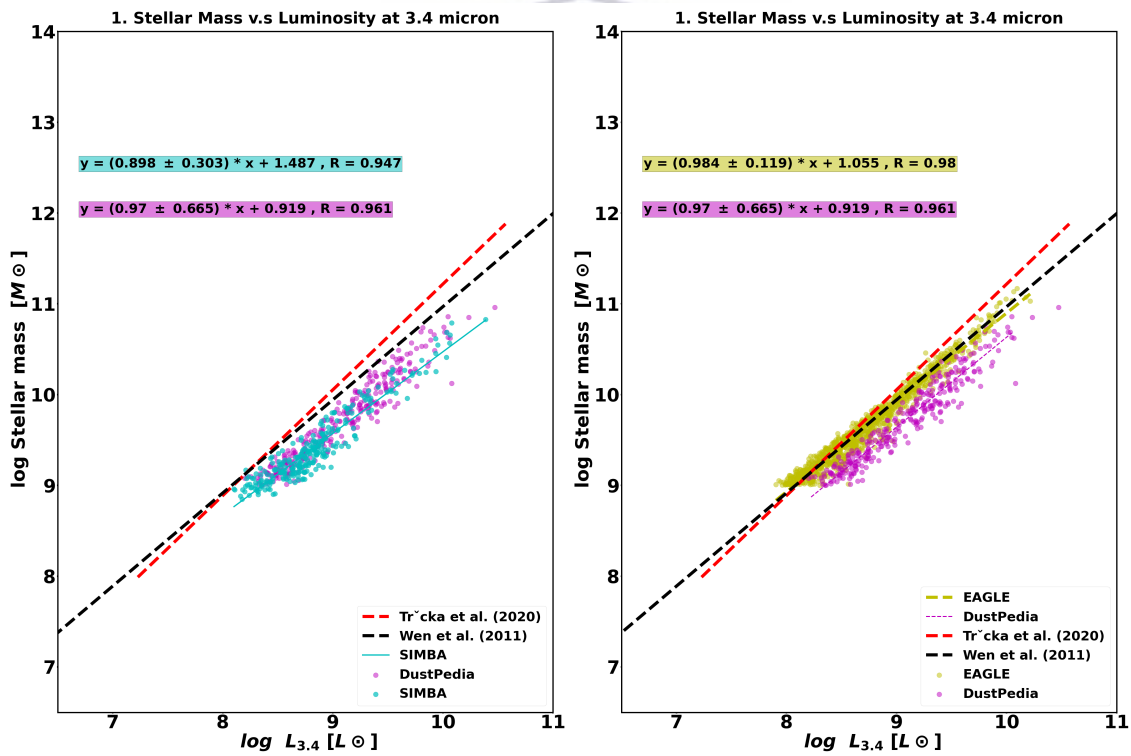


**Figure 23:** The  $3.4\mu\text{m}$  galaxies' luminosities and their stellar mass relation. For each presented sample, the galaxies' dots are coloured as follows; EAGLE (green), SIMBA (cyan) and DustPedia (magenta). The dashed lines are traced from previous literature (Trčka et al. (2020) - red dashed line; Wen et al. (2013) - black dashed line).

The stellar masses of EAGLE galaxies are similar to DustPedia galaxies, as shown in

Figure 15. Therefore, the offset observed between DustPedia and EAGLE stellar mass tracer relation is likely because SKIRT underestimated the WISE  $3.4\mu\text{m}$  band fluxes. Both simulations used the SED template established by Bruzual & Charlot (2003) to model the galaxies' stellar region particles when running galaxies through SKIRT. The Bruzual & Charlot (2003) SED template is a stellar mass-dependent template, so it gets affected by the simulation's sub-grid recipes. The flux estimation difference observed in EAGLE galaxies is likely due to the EAGLE simulation's initial mass functions, not SKIRT or the SED template. In support of our suggestion, Schaye et al. (2015) demonstrated that the EAGLE simulation does not produce the expected stellar and black-hole masses since the simulation does not include all the ISM structure modelling physics, such as cold interstellar gas phase. In addition, Davé et al. (2019)'s Figure 4 shows the galaxy stellar mass function evolution for EAGLE and SIMBA galaxies and compares their functions with observations from  $z = 6$  to  $z = 0$ . From their figure and overall findings, in comparison to EAGLE, SIMBA's simulation galaxy stellar mass functions appeared to be in good agreement with observations, especially at lower redshifts  $z < 3$ .

### 3.2.2 The WISE $22\mu\text{m}$ luminosity as the galaxy SFR proxy

Figure 24 shows the WISE  $22\mu\text{m}$  luminosity as a proxy for galaxy SFR. SIMBA and EAGLE simulations' SKIRT estimated fluxes are similar to fluxes from observations and previous literature, as shown in the figure. For both simulations, the galaxies were processed using the same MAPPING III SED template during the SKIRT processing. The template is parameterised based on the galaxies' metallicity, compactness, ISM pressure, and PDR covering factor (Groves et al., 2008). Table 3 shows that all of these parameters, except metallicity, were calculated during the post-processing procedure and are not directly extracted from the simulation snapshot. Based on this, both simulations' star-forming regions reproduce the fluxes of real galaxies when coupled with SKIRT.

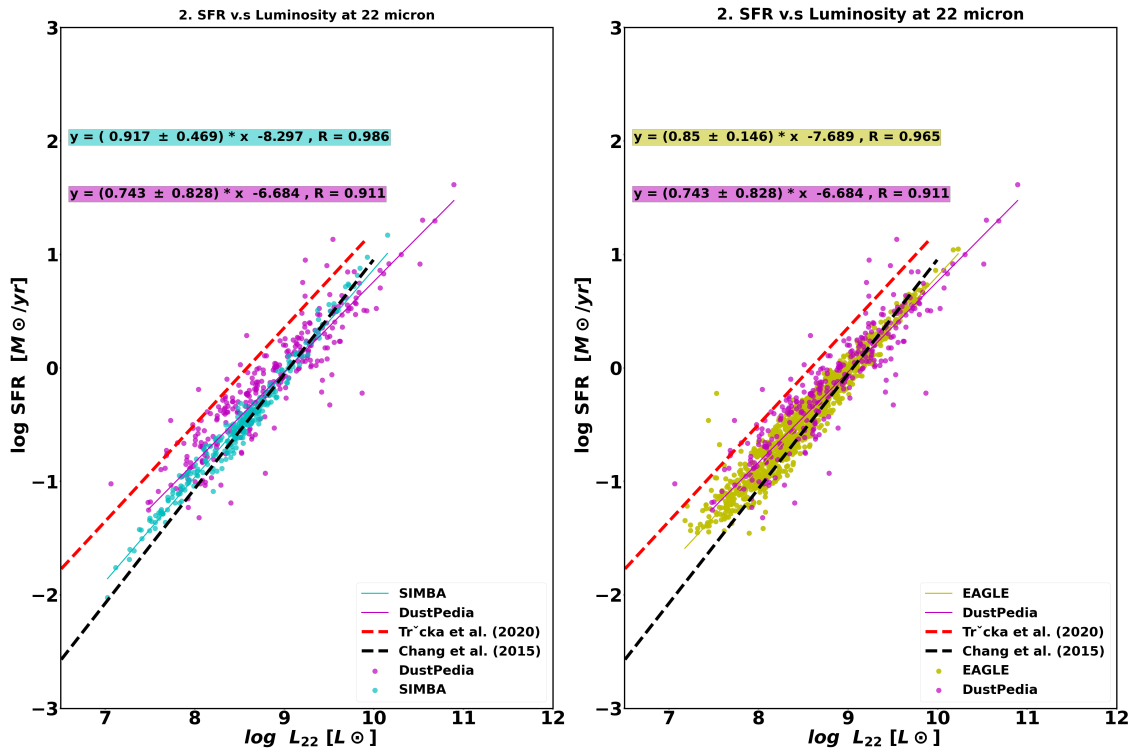


**Figure 24:** The  $22\mu\text{m}$  galaxies' luminosities and their SFR relation. For each presented sample, the galaxies' dots are coloured as follows; EAGLE (green), SIMBA (cyan) and DustPedia (magenta). The dashed lines are previous literature fits from Trčka et al. (2020) presented by the red dashed lines, and Chang et al. (2015) presented by the black dashed lines.

### 3.2.3 The SPIRE $250\mu\text{m}$ luminosity as the galaxy dust mass proxy

Figure 25 shows the SPIRE  $250\mu\text{m}$  luminosity as a proxy for the galaxy dust mass. The relation shows that the SIMBA galaxies' SKIRT estimated fluxes agree with observations better than the EAGLE galaxies' SKIRT estimated fluxes. Although the EAGLE galaxies' fluxes are under-estimated, there is not much difference between the EAGLE and DustPedia galaxies' SPIRE  $250\mu\text{m}$  fluxes ( $\leq 9\%$ ). The EAGLE simulation does not have dust implementations that trace the galaxy's dust formation, growth, and destruction. However, the EAGLE galaxies' dust masses were derived and calibrated to match the observed dust scaling relations during the EAGLE post-processing in Camps et al. (2016). However, when running the galaxies in SKIRT, each simulation used a different SED template to represent the simulations' diffuse dust. The differences in the templates used are likely to be the cause of the observed differences in the SKIRT estimated fluxes. We used the THEMIS dust model (Jones et al., 2017) on SIMBA galaxies, Camps et al.

(2016) used the Zubko et al. (2004) dust model on EAGLE galaxies when processing the galaxies through SKIRT. The Zubko et al. (2004) dust modelling is for non-composite to ensure the derived dust accurately reproduces real dust emission, extinction and abundance constraints of the Milky Way since the model mimics realistic dust mixtures. On the other hand, the THEMIS template models the dust in the diffuse interstellar medium. The main difference between the two models is that the Zubko et al. (2004) model FIR to submm emissivity was two factors higher than THEMIS. In particular, Zubko et al. (2004) finds more aromatic hydrocarbons around  $20 \mu m$  than the THEMIS model. Additionally, the THEMIS model aromatic features FIR emission strength that is twice that of the Zubko model (Galliano et al., 2018; Trčka et al., 2020).

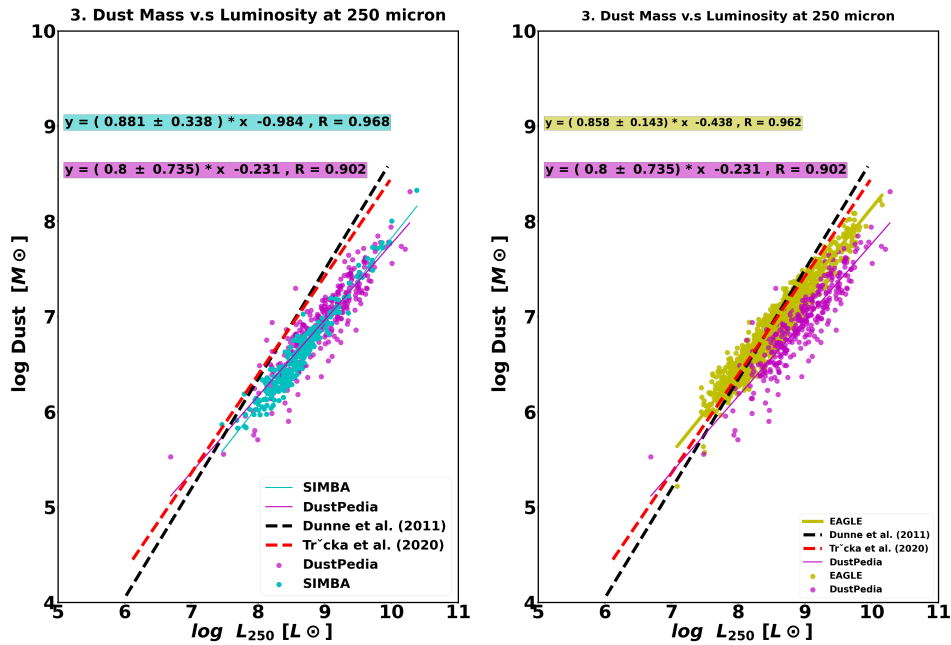


**Figure 25:** The  $250 \mu m$  galaxies' luminosities and their dust mass relation. For each presented sample, the galaxies' dots are coloured as follows; EAGLE (green), SIMBA (cyan) and DustPedia (magenta). The dashed lines are previous literature fits from Trčka et al. (2020) presented by the red dashed lines, and Dunne et al. (2011) presented by the black dashed lines.

### 3.2.4 Result summary

This section examined the ability of the EAGLE and SIMBA simulation's SKIRT estimated fluxes to agree with observational fluxes and common known proxies. Our results

show that our data samples reproduce the common proxies. Results agree with the WISE  $3.4\mu m$  band luminosities being the excellent galaxy stellar mass tracers, the WISE  $22\mu m$  luminosities being the good galaxies SFR tracers, and the submillimetre SPIRE  $250\mu m$  band fluxes being the good galaxy dust masses estimators as shown in previous literature (Trčka et al., 2020; Lee et al., 2013) and (Dunne et al., 2011). Our results also show that SIMBA galaxies imitate observations better than EAGLE galaxies. The EAGLE galaxies  $3.4\mu m$  and  $250\mu m$  fluxes are underestimated, except in the  $22\mu m$  fluxes and SFR relation, where both simulations perform reasonably equally. However, in Figure 26, we found that both the SIMBA and EAGLE galaxies' estimated SKIRT fluxes agree with fluxes from the DustPedia observations at  $1\sigma$  intrinsic scatter.

Additionally, we notice that the studied common proxies are tightly correlated, and we derive the mathematical forms of the luminosity proxies given in equation 20, 21, and 22. These equations benefit the community, e.g., if one has flux in  $3.4\mu m$ , from observations and simulations, then computation of the galaxy stellar mass is straightforward using equation 20.

$$\text{Stellar\_mass} = (0.952 \pm 0.427) L_{3.4\mu m} + 1.179 \quad (20)$$

$$\text{SFR} = (0.84 \pm 0.556) L_{22\mu m} + 7.586 \quad (21)$$

$$\text{Dust\_mass} = (0.847 \pm 0.474) L_{250\mu m} + 0.636 \quad (22)$$

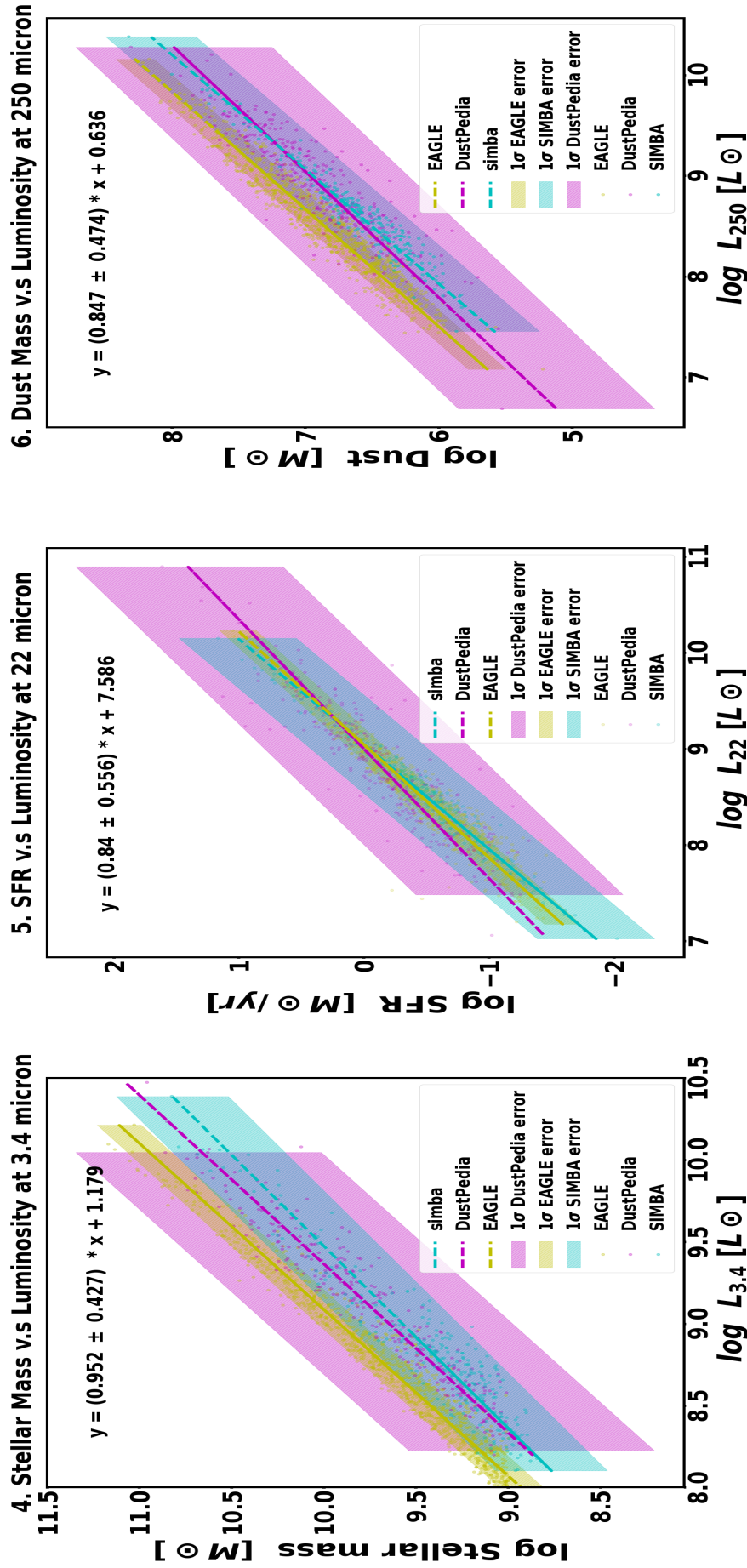


**Figure 26:** The relationship between the galaxies' luminosities and their stellar mass, dust mass, and SFR. The dots represent the SIMBA (cyan), EAGLE (green), and DustPedia (magenta) galaxies. The best fit line of each dataset is shown in the same colour code as the dots in each plot. The dashed red and black lines represent the same scaling relation taken from previous literature for comparison. In the top row, The red dashed lines represent Trčka et al. (2020) relations, and the black dashed lines from left to right represents Wen et al. (2013), Chang et al. (2015), and Dunne et al. (2011) relations respectively. The bottom row is the regression line, and the  $1\sigma$  intrinsic scatter of the dataset colour codes is similar to the first row.

### 3.3 The MIR/FIR luminosities scaling relations

This section presents the MIR and FIR luminosities scaling relations for the three datasets in Figure 27 and Figure 28. The presented results are similar and in agreement with those shown in Trčka et al. (2020) for EAGLE and DustPedia galaxies. Additional to Trčka et al. (2020)'s findings, we also found interesting results on SIMBA simulation, which are presented and discussed in this section.

#### 3.3.1 Scaling relation between luminosities in the $3.4\mu\text{m}$ and $22\mu\text{m}$ band

Figure 27 (a) shows the relationship between the WISE  $3.4\mu\text{m}$  and WISE  $22\mu\text{m}$  bands, a good proxy for the galaxy SFR per unit stellar mass. The relation displays a strong positive correlation between the presented bands. It shows that the galaxy's stellar mass increases with the star-formation rate, which is expected since we know that star-forming galaxies form new stars because they are rich in the gas needed for star-formation (Davé, 2008; Maragkoudakis et al., 2017) and (Schombert et al., 2022).

#### 3.3.2 Scaling relation between luminosities in the $3.4\mu\text{m}$ and $250\mu\text{m}$ band

Figure 27 (b) shows the relationship between the WISE  $3.4\mu\text{m}$  and SPIRE  $250\mu\text{m}$  luminosities, a good proxy for the galaxy dust mass per unit stellar mass. The relation shows a strong positive correlation between the galaxy dust mass and the stellar galaxy mass for the three data sets. In Figure 27 (a), we saw that massive galaxies form more stars. Now, this relation shows that massive galaxies also have more dust. We know that dust production, growth, and destruction in the ISM involve many processes that affect star formation and the stellar initial mass function (Asano et al., 2013; Calura et al., 2016). Asano et al. (2013) have shown that ISM dust mass growth is the main contributor of dust in galaxies with different SFR and ages. During stellar evolution, stellar mass loss and supernovae remnants release significant metals that condense to dust grains. Accretion of atoms and molecules promotes dust mass growth in the ISM (Asano et al., 2013; Draine, 2003). The correlation between the galaxy dust mass and stellar galaxy mass (shown in Figure 27b) is affected by the galaxy SFR (Santini et al., 2014). From Figure 27 (a) and (b), we learn that the more massive a galaxy is, the higher the SFR, with more dust content.

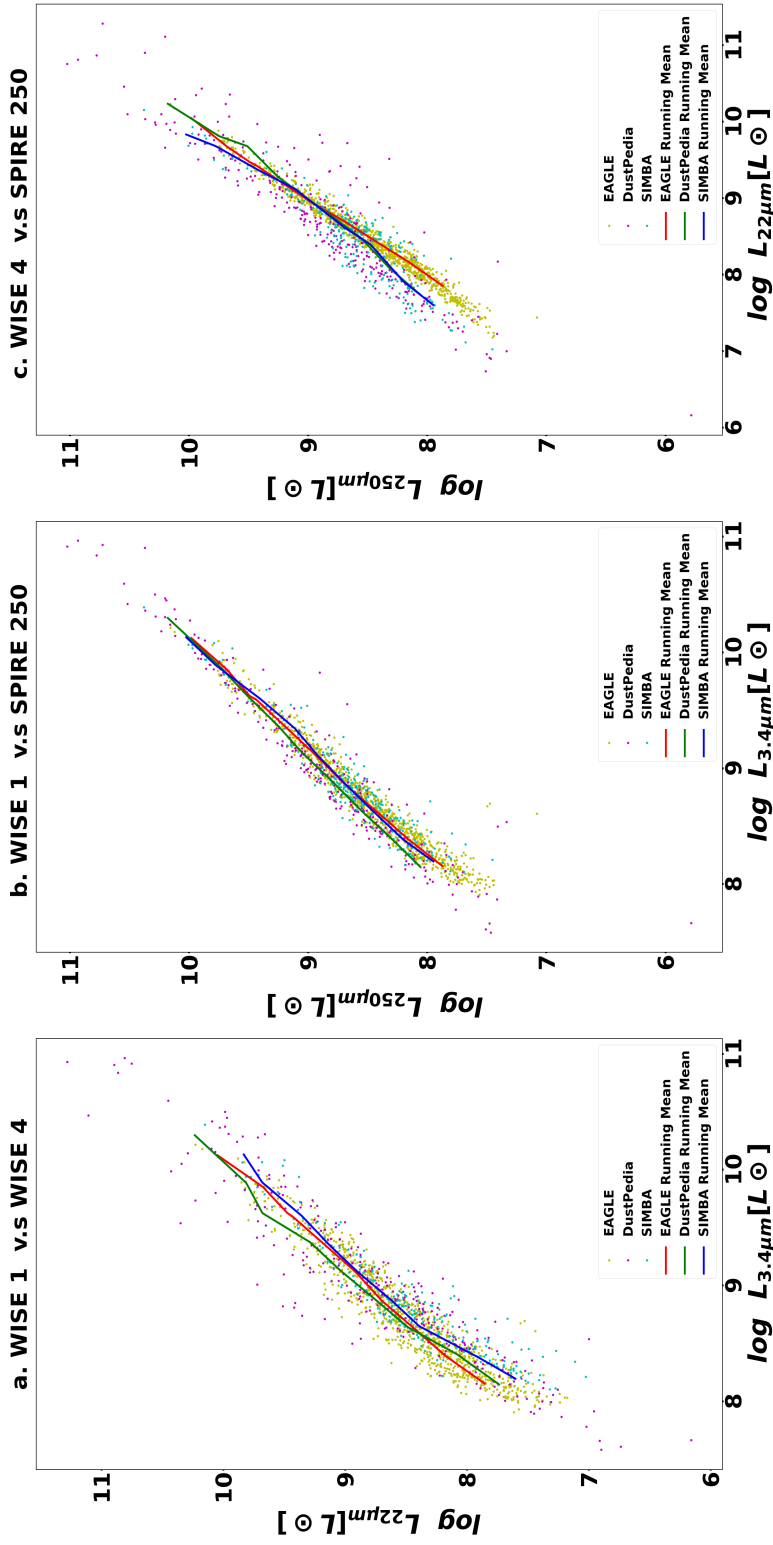


**Figure 27:** The scaling relations of the galaxies' MIR and FIR luminosities. The dots represent galaxies in each dataset, EAGLE (green), DustPedia (magenta), and SIMBA (cyan). The red, green, and blue lines are the galaxies' running mediums for datasets labelled in the plot legend.

### 3.3.3 Scaling relation between luminosities in the $22\mu m$ and $250\mu m$ band

Figure 27 (c) shows the relationship between WISE  $22\mu m$  and SPIRE  $250\mu m$ , a proxy relation for the galaxy SFR per unit dust mass. The relation displays a positive correlation between the galaxy dust mass and the galaxy star formation rate, which is expected as discussed in Figure 27 (b). Stars form within molecular dust clouds, and in the presence of dust and a cool ISM, the formation of molecular cloud increases by two orders of magnitude, resulting in more SFR activation (Hollenbach & McKee, 1979; Asano et al., 2013). In summary, a significant amount of dust makes the environment favourable for star formation. Figure 27 (c) shows the same relationship for the three data sets.

### 3.3.4 Interesting findings in the luminosities ratio relations

We have learned about the physical properties of the ISM in the first three luminosity scaling relations in Figure 27. We saw that the more massive a galaxy is, the more dust it contains and the higher the SFR. Nevertheless, from these relations, we could not identify the degree to which each simulation imitates observations of real galaxies. Figure 29 shows the sigma intrinsic scatter agreement for the relations studied in this section, and indeed in the first three relations; all samples are in agreement except for the luminosity ratio scaling relations shown in Figure 28. Figure 28 is a proxy for the galaxy specific dust versus galaxy sSFR ( $L_{250\mu m} / L_{3.4\mu m}$  versus  $L_{22\mu m} / L_{3.4\mu m}$ ).

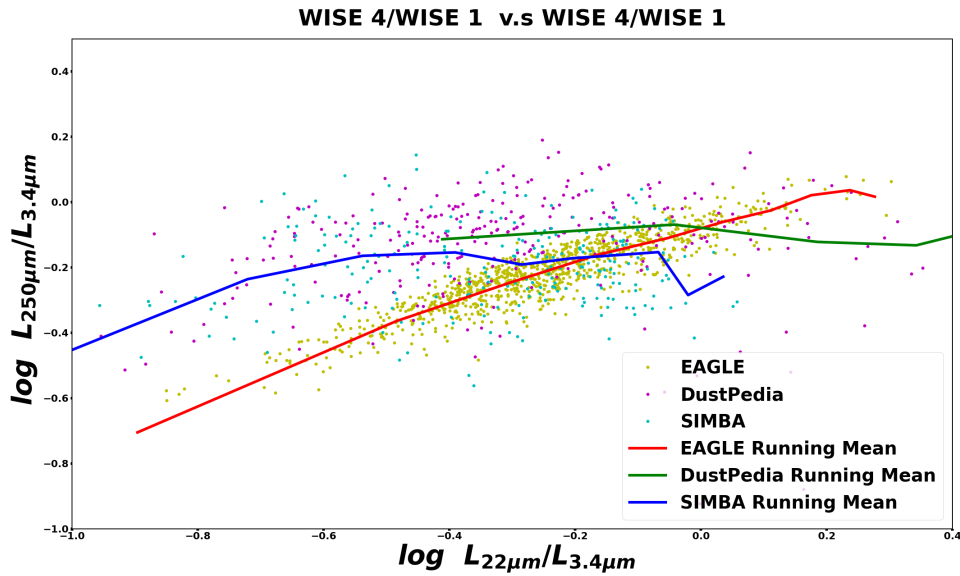


**Figure 28:** The scaling relations of the galaxies' MIR and FIR luminosities. EAGLE (green), DustPedia (magenta), and SIMBA (cyan) dots represent the galaxies in each dataset. As labelled in the plot legend, the red, green, and blue lines are the galaxies' running mediums for the datasets.

In Figure 28, the EAGLE galaxies' sSFR increases with increasing specific dust masses continually. On the other hand, SIMBA galaxies' sSFR increases with specific dust masses in the lower sSFR ranges ( $L_{22\mu m} / L_{3.4\mu m} < -0.4$ ); corresponding to lower mass galaxies. The curve then flattens in the higher sSFR range ( $L_{22\mu m} / L_{3.4\mu m} > -0.4$ ); thus, higher mass galaxies with higher sSFR. This curve flattening is also observed in real galaxies, suggesting that the SIMBA simulation has succeeded in simulating another observational scaling relation to be discussed shortly.

## Discussion

They are two possible causes of the curve flattening observed in SIMBA and DustPedia galaxies. The first cause may be the decrease in star formations, wherein galaxies' gas reservoirs run low, resulting in star formation shut down, causing a flattening at the higher mass end. The second reason may be due to massive galaxy quenching<sup>18</sup> as a result of AGN feedback. All galaxies are believed to be centred around BHs, which feed on the surrounding gas or material through accretion.

<sup>18</sup>Galaxy quenching occurs when a galaxy loses its cold gas and starts suppressing its star formation until it no longer produces stars

As with SIMBA, EAGLE simulations include baryonic processes like star formation, AGN feedback, and cooling (Baes et al., 2019). The main difference between the two simulations is SIMBA's main features. SIMBA's features include high-resolution subgrid models, unique dust production models, unique destruction models, and AGN jet quenching feedback models that rely on black-hole accretion rates (Davé et al., 2019; Lovell et al., 2021). These special features enable SIMBA to produce BH and galaxies that are in good agreement with observations because on-the-fly dust production and destruction models improve the extinction model of the simulation and dust extinction plays a vital role in observations. The BH jet feedback contributes immensely to the baryonic process, including the quenching of massive galaxies.

### 3.3.5 Result summary

This section studied the ISM infrared luminosities scaling relations for SIMBA simulations, EAGLE simulation, and DustPedia observations to understand the galaxies' ISM's physical properties and evaluate if the simulated galaxies behave like observational galaxies. Overall, the results shows that the three datasets were in agreement at  $1\sigma$  intrinsic scatter, shown in Figure 29 with an RMS intrinsic scatter  $\leq 0.5$ . The physical interpretation of these ISM relations showed that massive galaxies have more dust and high SFR. We also found that the SIMBA unique features enable the simulation to reproduce the observed quenching scenario seen in massive galaxies ( $> 10M_{\odot}$ ), as depicted in Figure 28 and also found in Li et al. (2019) and Davé et al. (2019).

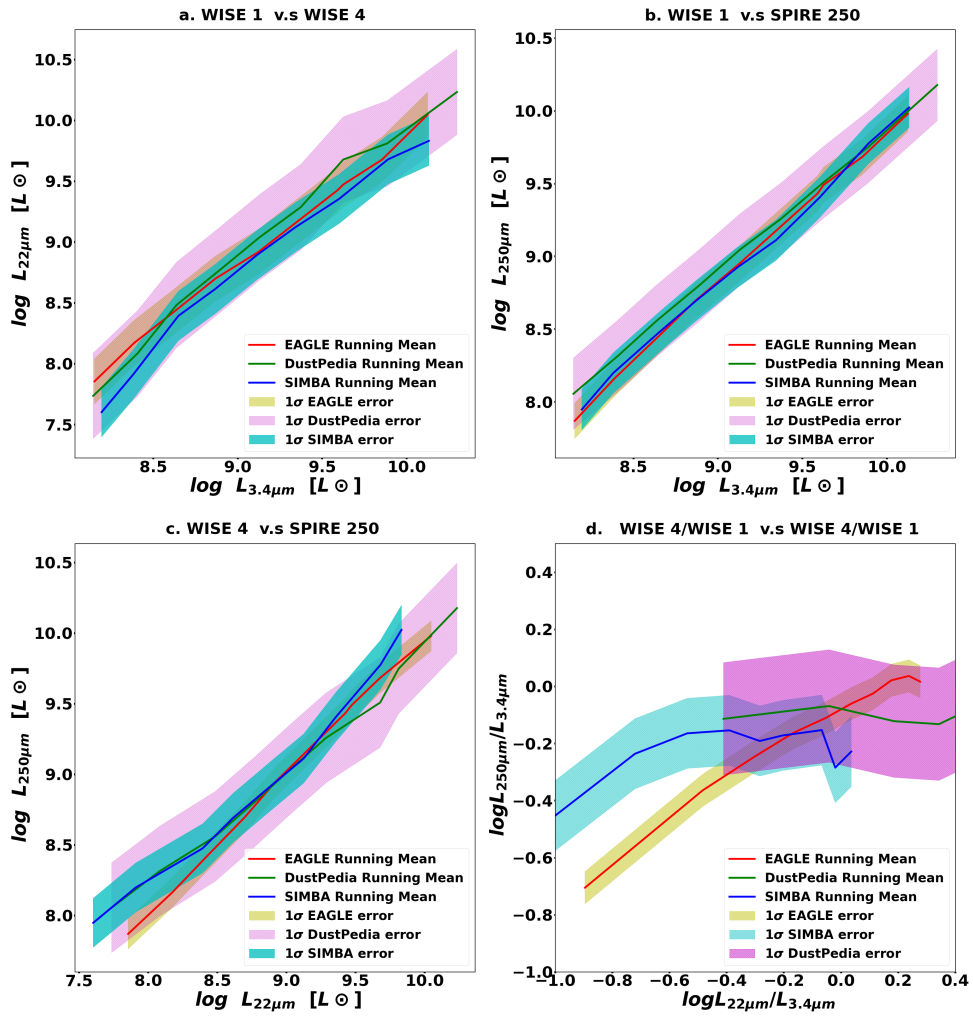


**Figure 29:** The scaling relations of Figure 27 and Figure 28 intensity scatter at  $1\sigma$ .

### 3.4 Dust to stellar mass ratios scaling relation

The dust-to-stellar mass ratio scaling relations are good to consider when interested in understanding galaxies' dust properties (Hou et al., 2019). So far, both simulations performed reasonably well in reproducing real galaxies MIR and FIR luminosities scaling relations; even better, the SIMBA galaxies have reproduced the phenomenon of quenching in massive galaxies, as seen in observations, within  $1\sigma$  intrinsic scatter. We also studied the scaling relations of the galaxies' inferred physical properties for deeper analysis and comparison with previous findings (Camps et al., 2016). We studied the scaling relation between dust-to-stellar mass ratios versus galaxy stellar mass, the submm colour-colour SPIRE fluxes, and the dust-to-stellar mass ratios versus NUV-r colour. We found some discrepancies between observations and simulations, which are discussed in this section.

We found good agreement between both simulations' and observations' dust-to-stellar mass ratios versus galaxies' stellar mass relation in Figure 30 (top panel). We observe a similar slope in all three samples' flux ratios relationships, with a good agreement between SIMBA and DustPedia ratios, but lower ratios for EAGLE galaxies in Figure 30 (middle panel). We also found a huge offset in the SIMBA galaxies' dust-to-stellar mass ratio versus the NUV-r colour plot in Figure 30 (bottom panel), the NUV-r colour-magnitude is a good proxy for sSFR (Schiminovich et al., 2007)). DustPedia and EAGLE galaxies agree, showing an anti-correlating trend between the galaxies' dust-to-stellar ratios and the NUV-r colour magnitudes. Our results were the same as those presented in Camps et al. (2016), the difference here is that we present only a subset of their sample due to the applied selection criteria. Moreover, Camps et al. (2016)'s selection criteria were not sSFR based; rather, they were based on galaxy stellar mass ( $M_* > 10^{8.5}$ ). The sampling included galaxies from different EAGLE snapshots (Re-cal25, Ref25, and Ref100) and the number of stellar particles per galaxy (2000/galaxy). Therefore Camps et al. (2016)'s EAGLE sample accommodated higher mass galaxies ( $> 10^{10} M_\odot$ ) with lower dust-to-stellar ratios ( $< -3.5$ ) and these galaxies clearly demonstrates the relation diverges at  $> 10^{10} M_\odot$ ). Our results displayed the deviation observed in Camps et al. (2016); however, because of this work's selection criteria the deviation observed in Camps et al. (2016) is not because we had fewer higher mass galaxies with lower dust-to-stellar ratios. However, we managed to reproduce Camps et al. (2016)'s dust scaling relations. In Camps

et al. (2016), they found that the EAGLE lower flux ratios seen in Figure 30 (bottom panel) indicated lower dust temperatures, and large cold dust contributions ( $T \leq 18K$ ) confirming sub-grid model limitations, implying that the EAGLE simulated dust was insufficiently heated.

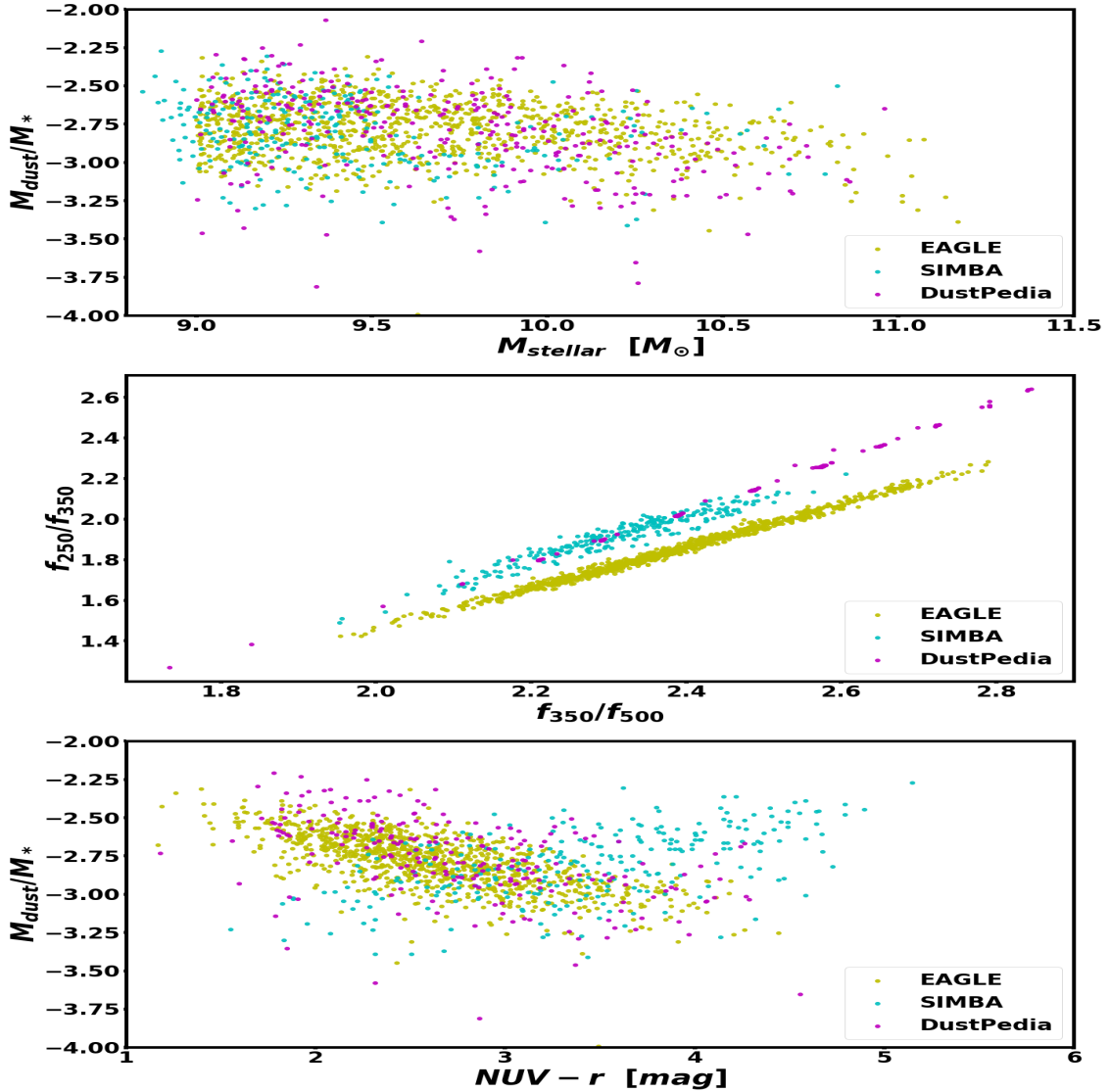


**Figure 30:** Dust scaling relations for SIMBA galaxies (cyan) and EAGLE galaxies (green), compared with the DustPedia (magenta) galaxies. The top panel shows the dust-to-stellar mass ratio versus the NUV-r colour. The middle panel shows the dust-to-stellar mass ratio versus the galaxy’s stellar mass. The bottom panel shows the SPIRE colour-colour relation  $f_{250}/f_{350}$  versus  $f_{350}/f_{500}$ .

After these findings, we attempted to discover possible reasons why some of the SIMBA galaxies’ have a huge offset observed in the dust-to-stellar masses versus the

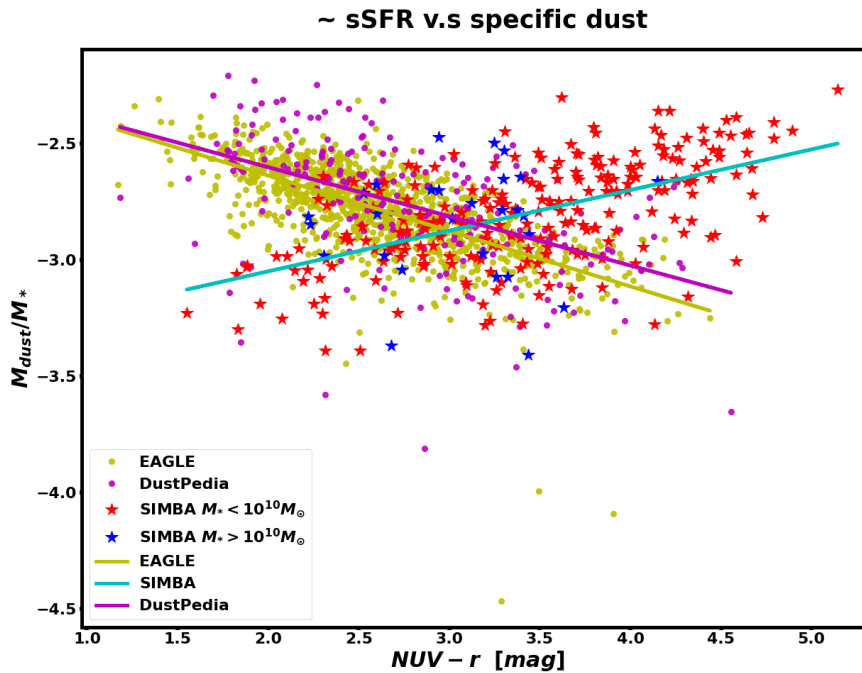


**Figure 31:** The scaling relation of the NUV-r colour magnitudes ( sSFR) versus specific dust. The dots represent EAGLE (green) and DustPedia (magenta) galaxies. The stars represent SIMBA galaxies that are less than  $10M_{\odot}$  (red) and SIMBA galaxies that are  $10M_{\odot}$  (blue). The best fit line of each dataset is shown in the same colour code as the dots and stars in each plot.

NUV-r colour plots. In the plot, the EAGLE and DustPedia galaxies show a relation of specific dust decreasing as the galaxies become redder or the NUV-r colour-magnitude increases. On the other hand, SIMBA galaxies display an overall opposite trend. SIMBA galaxies become redder as specific dust increases. Our first assumption was the known SIMBA simulation's bimodality. Figure 6 of [Davé et al. \(2019\)](#) show that the SIMBA simulations (1) overestimate the sSFR for lower mass galaxies and (2) estimate the correct sSFR for quenching and quenched systems (higher mass galaxies). To test our suggestion, we created Figure 31 to see if the SIMBA higher mass galaxies would agree with EAGLE and DustPedia. We found that most of the lower-mass galaxies, presented as red stars in the plot, were in the offset; however, some of the higher-mass galaxies were also in these offsets. Thus, we could not conclude it was the simulation's bimodality.

In Section 3.3, we saw that there was a relationship between the galaxy dust mass, stellar mass, and SFR; therefore, we re-created the NUV-r colour plot and colour-coded the

galaxies according to their SFR to see if this offset could be related to the SFR to the galaxies (see Figure 32). The figure shows that most SIMBA galaxies with higher dust-to-stellar mass ratios are bluer, implying higher SFR. Again there were other red-orange galaxies in the offset, meaning there might be another reason causing this offset in SIMBA galaxies. Therefore, the research can only conclude that SIMBA failed to reproduce the observed NUV-r colour versus specific dust trend. It would be interesting to explore the main causes of this discrepancy in future work.

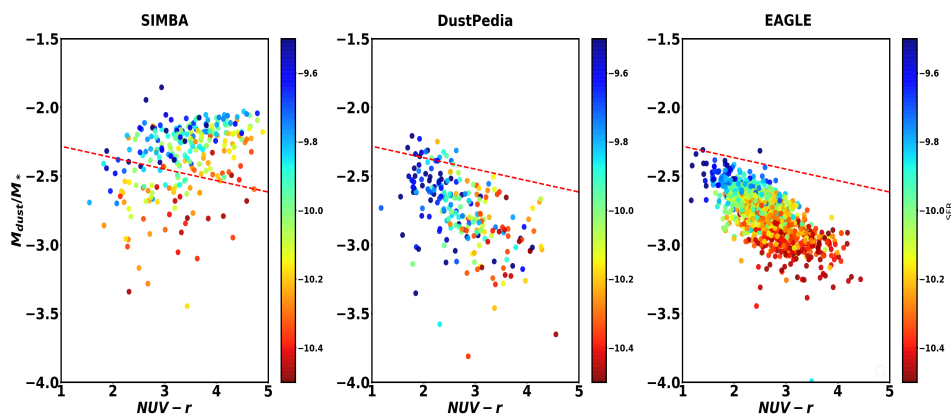
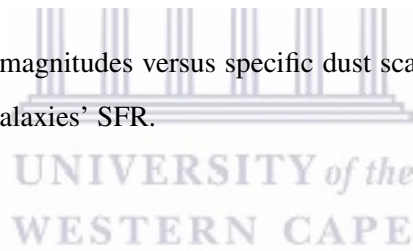


**Figure 32:** The NUV-r colour magnitudes versus specific dust scaling relations as in Figure 31, colour coded according to the galaxies' SFR.



### 3.4.1 Result summary

Although we did not get to the main reason why each simulation (mainly SIMBA) has the observed discrepancies, this section has proven that both simulation's sub-grid recipes still need to be improved. Based on the relation studied, we suggest improving the SFR sub-grid recipe for SIMBA simulations and the dust heating and population recipe for EAGLE simulations. Future work is also suggested for further analysis.

## 4 Conclusion

In this work, we test and validate the interstellar physics of the SIMBA hydrodynamic simulations with observations. To achieve the aims of this project, we studied and compared the ISM scaling relations of SIMBA simulations and DustPedia observations. We employed SKIRT to create the simulation's mock fluxes from UV to submm wavelength range. Due to similar work already being done on the EAGLE hydrodynamic simulation, we incorporated the EAGLE dataset already processed in SKIRT by [Camps et al. \(2016\)](#). This allowed us to compare the ISM conditions of two hydrodynamical simulations against observations. We note that this work is focused on local galaxies, both for simulations and observations. The project answered the following research questions: Do SIMBA-simulated galaxies' scaling relations reproduce observational galaxies' scaling relations? How is the performance of the SIMBA simulation compared to other simulations, particularly the EAGLE simulations? And below is the summary of our findings :

1. SIMBA galaxies' SKIRT estimated fluxes agree with observational fluxes better than EAGLE galaxies' SKIRT fluxes. The SKIRT fluxes for EAGLE galaxies at  $3.4\mu m$  wavelength are underestimated by a factor of 0.94 dex (see Section 23).
2. For both simulations, there was a good agreement between the simulated and observed galaxies' SFR and  $22\mu m$  SKIRT fluxes relation (see Section 24).
3. There's a better agreement between the SIMBA and observational galaxies' dust masses and the  $250\mu m$  fluxes relation. In this case, the percentage difference between the EAGLE and the observations is  $\leq 9\%$  (see Section 25). However, overall there was a fair agreement between the simulated and observed galaxies' dust masses and  $250\mu m$  fluxes.
4. We derived the mathematical forms for the common proxies presented in Section 3.2. To estimate the SFR of a galaxy, we present equation 21. For the galaxy stellar mass, we present equation 20, and for the galaxy dust mass, we present equation 22.
5. For the FIR and MIR luminosities' scaling relations in Section 3.3, we found that both SIMBA and EAGLE simulations reasonably reproduced the observed ISM

scaling relations. This was true especially for SIMBA galaxies since their main features enabled the quenching of massive galaxies, as shown in Figure 28.

6. In the physical properties and colour scaling relations in Section 3.4, we found that both SIMBA and EAGLE simulations reproduced the observed physical property dust scaling relations with some limitations. SIMBA reproduced the dust-to-stellar mass ratio versus galaxy stellar mass and the  $f_{250}/f_{350}$  versus  $f_{350}/f_{500}$  ratio relation, with huge offsets in the dust-to-stellar versus NUV-r colour relation that is not yet fully understood. The EAGLE dust-to-stellar mass ratio versus stellar mass and NUV-r colour relations agreed with observations, with discrepancies in the  $f_{250}/f_{350}$  versus  $f_{350}/f_{500}$  ratio relation, implying insufficiently heated simulated dust.

After trying different possible reasons, the main cause of the SIMBA galaxies' huge offset in the dust-to-stellar versus NUV-r colour is not yet fully understood and is considered for future work. One of the things that can be improved for future analysis can be the selection criteria. The selection used in this work excluded most of the higher mass quenched and quenching systems that would have enabled testing the SIMBA bimodality discussed in the results section. In that note we suggest a similar selection criteria used in [Camps et al. \(2016\)](#) and [Trčka et al. \(2020\)](#) for future work. Despite this, we conclude that this project was successful as we have proven that the SIMBA simulations can reproduce observational galaxies' scaling relations when coupled with SKIRT.

## References

- Abraham R. G., van den Bergh S., 2001, *Science*, 293, 1273
- Anghopo J., 2021, PhD thesis, UCL (University College London)
- Asano R. S., Takeuchi T. T., Hirashita H., Inoue A. K., 2013, *Earth, Planets and Space*, 65, 213
- Baes M., Trčka A., Camps P., Nersesian A., Trayford J., Theuns T., Dobbels W., 2019, *Monthly Notices of the Royal Astronomical Society*, 484, 4069
- Baes M., et al., 2020, *Monthly Notices of the Royal Astronomical Society*, 494, 2912
- Birnboim Y., Dekel A., 2003, *Monthly Notices of the Royal Astronomical Society*, 345, 349
- Boquien M., Burgarella D., Roehly Y., Buat V., Ciesla L., Corre D., Inoue A., Salas H., 2019, *Astronomy & Astrophysics*, 622, A103
- Brinchmann J., Charlot S., White S. D., Tremonti C., Kauffmann G., Heckman T., Brinkmann J., 2004, *Monthly notices of the royal astronomical society*, 351, 1151
- Brussaard P., Van de Hulst H., 1962, *Reviews of Modern Physics*, 34, 507
- Bruzual G., Charlot S., 2003, *Monthly Notices of the Royal Astronomical Society*, 344, 1000
- Calura F., et al., 2016, *Monthly Notices of the Royal Astronomical Society*, p. stw2749
- Camps P., Baes M., 2015, *Astronomy and Computing*, 9, 20
- Camps P., Trayford J. W., Baes M., Theuns T., Schaller M., Schaye J., 2016, *Monthly Notices of the Royal Astronomical Society*, 462, 1057
- Casasola V., et al., 2020, *Astronomy & Astrophysics*, 633, A100
- Chabrier G., 2003, *Publications of the Astronomical Society of the Pacific*, 115, 763
- Chang Y.-Y., van der Wel A., da Cunha E., Rix H.-W., 2015, *The Astrophysical Journal Supplement Series*, 219, 8

- Clark C. J., et al., 2018, *Astronomy & Astrophysics*, 609, A37
- Cole S., Aragon-Salamanca A., Frenk C. S., Navarro J. F., Zepf S. E., 1994, *Monthly Notices of the Royal Astronomical Society*, 271, 781
- Collaboration P., et al., 2020
- Commons W., 2020, File:OffsetTF.png — Wikimedia Commons, the free media repository, <https://commons.wikimedia.org/w/index.php?title=File:OffsetTF.png&oldid=449989615>
- Cortese L., et al., 2012, *Astronomy & Astrophysics*, 540, A52
- Dashyan G., Choi E., Somerville R. S., Naab T., Quirk A. C., Hirschmann M., Ostriker J. P., 2019, *Monthly Notices of the Royal Astronomical Society*, 487, 5889
- Davé R., 2008, *Monthly Notices of the Royal Astronomical Society*, 385, 147
- Davé R., Thompson R., Hopkins P. F., 2016, *Monthly Notices of the Royal Astronomical Society*, 462, 3265
- Davé R., Anglés-Alcázar D., Narayanan D., Li Q., Rafieferantsoa M. H., Appleby S., 2019, *Monthly Notices of the Royal Astronomical Society*, 486, 2827
- Davies J., et al., 2017, *Publications of the Astronomical Society of the Pacific*, 129, 044102
- Dekel A., Silk J., 1986, *The Astrophysical Journal*, 303, 39
- Deschamps R., Braun K., Jorissen A., Siess L., Baes M., Camps P., 2015, *Astronomy & Astrophysics*, 577, A55
- Draine B. T., 2003, *Annual Review of Astronomy and Astrophysics*, 41, 241
- Dunne L., et al., 2011, *Monthly Notices of the Royal Astronomical Society*, 417, 1510
- Dwek E., 1998, *The Astrophysical Journal*, 501, 643
- Galametz M., et al., 2013, *Monthly Notices of the Royal Astronomical Society*, 431, 1956
- Galliano F., Galametz M., Jones A. P., 2018, *Annual Review of Astronomy and Astrophysics*, 56, 673

- Glowacki M., Elson E., Davé R., 2020, *Monthly Notices of the Royal Astronomical Society*, 498, 3687
- Groves B., Dopita M. A., Sutherland R. S., Kewley L. J., Fischera J., Leitherer C., Brandl B., van Breugel W., 2008, *The Astrophysical Journal Supplement Series*, 176, 438
- Hahn C., et al., 2022, *The Astrophysical Journal*, 926, 122
- Hendrix T., Keppens R., Camps P., 2015, *Astronomy & Astrophysics*, 575, A110
- Hollenbach D., McKee C. F., 1979, *The Astrophysical Journal Supplement Series*, 41, 555
- Hopkins P. F., Quataert E., 2011, *Monthly Notices of the Royal Astronomical Society*, 415, 1027
- Hou K.-C., Aoyama S., Hirashita H., Nagamine K., Shimizu I., 2019, *Monthly Notices of the Royal Astronomical Society*, 485, 1727
- Jones A., Köhler M., Ysard N., Bocchio M., Verstraete L., 2017, *Astronomy & Astrophysics*, 602, A46
- Jonsson P., Groves B. A., Cox T., 2010, *Monthly Notices of the Royal Astronomical Society*, 403, 17
- Jørgensen I., Franx M., Kjaergaard P., 1996, *Monthly Notices of the Royal Astronomical Society*, 280, 167
- Kapoor A. U., et al., 2021, *Monthly Notices of the Royal Astronomical Society*, 506, 5703
- Kereš D., Katz N., Weinberg D. H., Davé R., 2005, *Monthly Notices of the Royal Astronomical Society*, 363, 2
- Keselman H., Othman A. R., Wilcox R. R., Fradette K., 2004, *Psychological Science*, 15, 47
- Kim H.-Y., 2014, *Restorative dentistry & endodontics*, 39, 74
- Koda J., Sofue Y., Wada K., 2000, *The Astrophysical Journal*, 532, 214

- Kroupa P., 2002, *Science*, 295, 82
- Larsen R. D., 1985, *Journal of Chemical Education*, 62, 302
- Lee J. C., Hwang H. S., Ko J., 2013, *The Astrophysical Journal*, 774, 62
- Li Q., Narayanan D., Davé R., 2019, *Monthly Notices of the Royal Astronomical Society*, 490, 1425
- Lovell C. C., Geach J. E., Davé R., Narayanan D., Li Q., 2021, *Monthly Notices of the Royal Astronomical Society*, 502, 772
- MacFarland T. W., Yates J. M., 2016, in , *Introduction to nonparametric statistics for the biological sciences using R*. Springer, pp 177–211
- Maragkoudakis A., Zezas A., Ashby M., Willner S., 2017, *Monthly Notices of the Royal Astronomical Society*, 466, 1192
- Mishra P., Singh U., Pandey C. M., Mishra P., Pandey G., 2019, *Annals of cardiac anaesthesia*, 22, 407
- Morrissey P., et al., 2007, *The Astrophysical Journal Supplement Series*, 173, 682
- Nelson D., et al., 2018, *Monthly Notices of the Royal Astronomical Society*, 475, 624
- Netzer H., 2013, *The physics and evolution of active galactic nuclei*. Cambridge university press
- Neugebauer G., et al., 1984, *The Astrophysical Journal*, 278, L1
- Pilbratt G., et al., 2010, *Astronomy & Astrophysics*, 518, L1
- Rémy-Ruyer A., et al., 2014, *Astronomy & Astrophysics*, 563, A31
- Rodriguez-Gomez V., et al., 2019, *Monthly Notices of the Royal Astronomical Society*, 483, 4140
- Sanders R., 2010, *Monthly Notices of the Royal Astronomical Society*, 407, 1128
- Santini P., et al., 2014, *Astronomy & Astrophysics*, 562, A30
- Schaye J., et al., 2015, *Monthly Notices of the Royal Astronomical Society*, 446, 521

- Schiminovich D., et al., 2007, *The Astrophysical Journal Supplement Series*, 173, 315
- Schombert J., McGaugh S., Lelli F., 2022, *The Astronomical Journal*, 163, 154
- Skrutskie M., et al., 2006, *The Astronomical Journal*, 131, 1163
- Somerville R. S., Davé R., 2015, *Annual Review of Astronomy and Astrophysics*, 53, 51
- Somerville R. S., Hopkins P. F., Cox T. J., Robertson B. E., Hernquist L., 2008, *Monthly Notices of the Royal Astronomical Society*, 391, 481
- Stalevski M., Fritz J., Baes M., Nakos T., Popović L. Č., 2012, *Monthly Notices of the Royal Astronomical Society*, 420, 2756
- Tomczak A. R., et al., 2016, *The Astrophysical Journal*, 817, 118
- Trčka A., et al., 2020, *Monthly Notices of the Royal Astronomical Society*, 494, 2823
- Treu T., Auger M. W., Koopmans L. V., Gavazzi R., Marshall P. J., Bolton A. S., 2010, *The Astrophysical Journal*, 709, 1195
- Tsai J. C., Mathews W. G., 1995, arXiv preprint astro-ph/9502053
- Tully R. B., Fisher J. R., 1977, *Astronomy and Astrophysics*, 54, 661
- Vogelsberger M., et al., 2014, *Monthly Notices of the Royal Astronomical Society*, 444, 1518
- Vogelsberger M., Marinacci F., Torrey P., Puchwein E., 2020a, *Nature Reviews Physics*, 2, 42
- Vogelsberger M., et al., 2020b, *Monthly Notices of the Royal Astronomical Society*, 492, 5167
- Volonteri M., 2010, *The Astronomy and Astrophysics Review*, 18, 279
- Wen X.-Q., Wu H., Zhu Y.-N., Lam M. I., Wu C.-J., Wicker J., Zhao Y.-H., 2013, *Monthly Notices of the Royal Astronomical Society*, 433, 2946
- Wikipedia contributors 2021a, Faber–Jackson relation — Wikipedia, The Free Encyclopedia, [https://en.wikipedia.org/w/index.php?title=Faber%E2%80%93Jackson\\_relation&oldid=1058960263](https://en.wikipedia.org/w/index.php?title=Faber%E2%80%93Jackson_relation&oldid=1058960263)

Wikipedia contributors 2021b, Galaxy color–magnitude diagram — Wikipedia, The Free Encyclopedia, [https://en.wikipedia.org/w/index.php?title=Galaxy\\_color%E2%80%93magnitude\\_diagram&oldid=1058147263](https://en.wikipedia.org/w/index.php?title=Galaxy_color%E2%80%93magnitude_diagram&oldid=1058147263)

Wright E. L., et al., 2010, The Astronomical Journal, 140, 1868

York D. G., et al., 2000, The Astronomical Journal, 120, 1579

Zubko V., Dwek E., Arendt R. G., 2004, The Astrophysical Journal Supplement Series, 152, 211

